Electron channelling in varying magnetic potentials

Lawton, David Neil

Award date:
2002

Awarding institution:
University of Bath

ELECTRON CHANNELLING IN VARYING MAGNETIC POTENTIALS

Submitted by David Neil Lawton
for the degree of
Doctor of Philosophy
of the University of Bath
2002

ProQuest LLC
789 East Eisenhower Parkway
P.O. Box 1346
Ann Arbor, MI 48106-1346

Abstract

Experiments have been performed examining different aspects of the magnetoresistance of a two dimensional electron gas (2DEG) subjected to an inhomogeneous magnetic field. Devices are studied in an external magnetic field; the inhomogeneity arising from a stripe of ferromagnetic material manufactured above the 2DEG. Experiments have focused on three main areas: confirming the magnetic channelling hypothesis; manipulating the magnetoresistance; and examining the response of the device to temperature.

Hybrid devices combining magnetic structures with semiconductors are of interest both for their potential applications in magnetoelectronics and as systems for studying fundamental physics in areas such as electron transport and integer and fractional quantum Hall effects. In addition, hybrid devices have the potential to model more complex systems of exotic particles such as composite fermions.

The results in this work present a clear picture of electron channelling by magnetic fields. Peaks in the magnetoresistance form due to two types of electron orbits: snake states (which dominate when the field from the ferromagnet produces neighbouring regions in the 2DEG having opposite directions of the magnetic field) and cycloid states (when the external field is sufficient to produce regions of varying strength but of the same sign). The position of the peaks varies depending on the strength of ferromagnet used and the carrier density. When placed in an angled applied field, the peak position is found to be invariant with respect to the z-component of the applied field, confirming the magnetic channelling picture. As the temperature is increased, the cycloid states are rapidly quenched (1.35-30K) while the snake states persist to higher temperature (>80K), showing their robustness to disorder. In addition, the Hall effect is strongly affected by the presence of snake and cycloid states and certain magnetic properties of the ferromagnetic stripe can be observed in the results.

As ever, there are more people to thank than can be listed here. I would like to start by thanking my supervisor, Dr. Alain Nogaret, for his support and enthusiasm over the course of the last three years. I would also like to acknowledge Dr. Maude and Prof. Portal for their help whilst working at Grenoble and Prof. Kibis for his theoretical input.

Then there are the many people who've helped me keep a healthy perspective throughout my time at Bath. I wouldn't have enjoyed myself half as much without the members of Backstage, the Arts Union and LINKS, all part of the Students Union. At the heart of the Students Union are, of course, Andrée and Charlie, Andrée in particular gets my thanks for her unflagging confidence in me.

Finally, some people who've been there when it was all getting a bit too much. Thank you Will for keeping me abreast of the latest developments in consumer technology, Jim for letting me join his club, Phish for some great weekends, Arturo for his vigilance and Hazel for being herself.

For my family

who always knew I could do this

Contents

Chapter 1

Quantum Semiconductor Structures

1.1 Overview

The basic theory required to describe particles confined to two, one or zero dimensions has been in place for nearly as long as quantum mechanics itself. However, it wasn't until the 1970's that it became possible to make practical devices based on the ideas. One of the major factors in this advance was the ability to make well defined semiconductor structures consisting of layers of different materials. In particular, groups within IBM, AT&T Bell labs and the Ioffe Institute were able to make heterostructures, devices in which the chemical composition varies with position, with layers as thin as 250Å. By 1973 the technology was reliable enough for device fabrication to be considered. Applications followed rapidly with heterostructure lasers [1], resonant tunnelling diodes [2] and superlattices [3]. Along with the new devices came experiments which challenged existing theories and required new physics to explain. Further improvements in fabrication techniques have created higher purity materials upon which to base even more ambitious sample designs. Today there is a huge, worldwide scientific community working on developing new quantum semiconductor devices and probing the underlying physics.

This thesis is based upon experimental and theoretical investigations of a specific

type of hybrid semiconductor/ferromagnetic device. The title of this chapter 'Quantum Semiconductor Structures' covers an incredibly broad and diverse field of modern physics into which this work falls. However, the field is too large to do justice to here, so only those areas which are of direct relevance are described below. Some ideas are then developed further in subsequent chapters.

1.2 The Two Dimensional Electron Gas

The groups at AT&T, IBM and the Ioffe institute were attempting to confine electrons to two dimensions by altering the semiconductor's chemical composition in the third dimension, creating a quantum well. The two dimensional electron gas (2DEG) formed in these heterostructures has rapidly become the system of choice, both for studying electron transport and for fabricating modern electronic devices. Its popularity has arisen from two principle strengths: theoretical treatments are simplified due to the reduced dimensionality and very high electron mobilities are possible, $\mu > 10^6$ cm^2/Vs.

1.2.1 Fabrication

The most widely used material system for fabricating 2DEGs is gallium arsenide (GaAs), a III-V semiconductor. A silicon-doped layer of aluminium gallium arsenide ($Al_xGa_{1-x}As$, where x is normally around 0.3 to keep the material's direct band gap) is produced on top of the GaAs to form a heterojunction. The interface is very smooth as there is near perfect lattice matching between the two materials. The electron affinity of AlGaAs is $\chi^1 = 3.74$eV, smaller than for GaAs, $\chi^2 = 4.07$eV, but the energy gap, E_G, between valence and conduction bands is greater (3eV for pure AlAs and 1.5eV for pure GaAs [4]) leading to the 'straddled' configuration as shown in figure 1.1. Conduction electrons transfer to the GaAs layer leaving a positively charged depletion region in the AlGaAs near the interface. This charged region bends the conduction band in GaAs downwards leading to an almost triangular potential well. The well confines electrons in the z-direction but leaves them free to travel in the x-y plane, so forming the 2DEG. Ideally, the transfer of charge from the AlGaAs to the GaAs layer leaves the AlGaAs completely depleted resulting in conduction solely in the 2DEG.

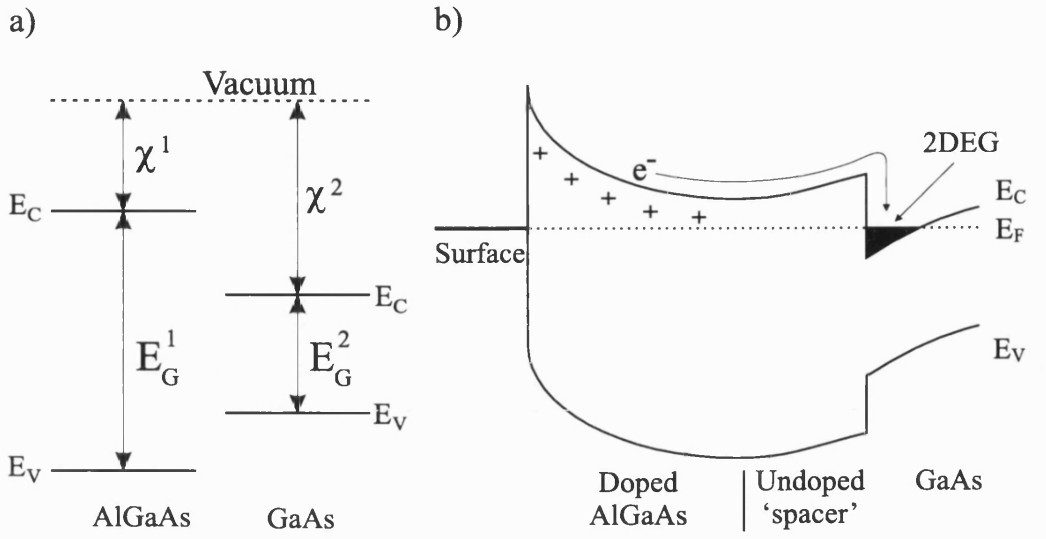

Figure 1.1: a) Electron affinity, χ, and energy gap, E_G, alignment leading to b) 'straddled' bandgap configuration in GaAs/AlGaAs system.

A typical device wafer will actually have several layers of different materials and doping built on either a silicon or GaAs substrate. These layers are typically produced by molecular beam epitaxy or metal organic chemical vapour deposition. Working from the substrate up, a thick, $\sim 1\mu$m, GaAs layer is grown. Then, in a process called modulation doping, the AlGaAs layer (doped with silicon donors) is deposited but the first 5-50nm is left undoped to form a spacer layer. This ensures that the electrons in the 2DEG are physically separated from the impurities in the doped AlGaAs region above the spacer, improving mobility. A thick spacer layer will improve mobility but decrease electron density, n_s, as the spacer acts as a barrier to the initial transfer of electrons from the doped AlGaAs to the GaAs. Finally, a layer of GaAs, called the cap, is grown to protect the more reactive AlGaAs layer from oxidation. The techniques used to grow the 2DEGs are good enough to allow for patterned substrates which has led to some interesting work (see section 1.4). It is also possible to construct a two dimensional hole gas by doping the AlGaAs layer with beryllium atoms which act as acceptors.

1.2.2 Delta Doping

An alternative method for producing 2DEGs is to delta-dope the GaAs layer. This entails growing a narrow GaAs region and depositing a thin, highly doped layer at its centre. This produces a very narrow quantum well in which electrons

can again form a 2DEG. The advantage of this method is that the 2DEG can be fabricated much closer to the surface ~30nm as opposed to ~100nm with the conventional technique. Unfortunately, mobility is reduced with respect to a conventional heterostructure as the electrons are physically close to the dopant impurities and so scattering is greater.

1.2.3 Applications and Research Areas

2DEGs have provided the ideal medium for studying the behaviour of ballistic electrons in electric and magnetic fields. In addition, their high mobility has led to completely new devices such as the quantum well laser and improvements on established devices leading to the high electron mobility transistor, the hetero-junction bipolar transistor and many others. Confinement to fewer dimensions to create one dimensional wires or zero dimensional dots is a newer field but has already seen applications such as quantum dot lasers. (Refs. [5, 6] offer good reviews of all these areas.)

The rest of this chapter looks at some of the fundamental physics they have been instrumental in investigating and the history leading up to this thesis.

1.3 Electrons in Magnetic and Electric Fields

1.3.1 Electron Transport

When describing electron transport in devices and categorising the effects that arise, two natural regimes are identifiable: ballistic and diffusive (see figure 1.2). If the mean free path, ℓ, is greater than the typical sample dimensions, d, then the electron's trajectory through the sample is likely to only be interrupted by the sample boundaries, giving ballistic transport. Quantum mechanical effects generally depend upon transport in this regime.

However, where ℓ is smaller than the sample dimensions, scattering from impurities and phonons leads to the electron taking a more random path through the

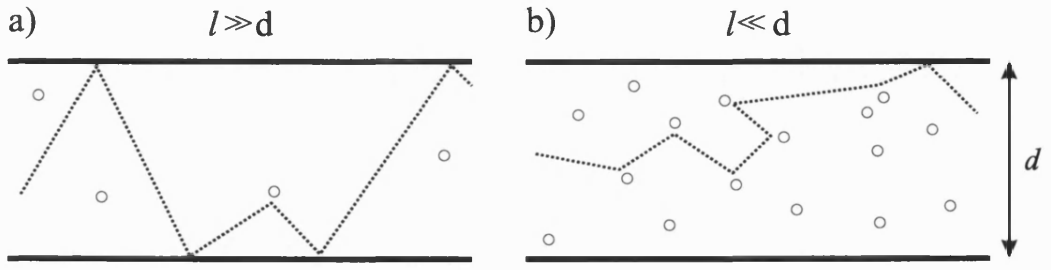

Figure 1.2: a) Ballistic and b) diffusive transport regimes. Open circles, 'o' represent potential scattering events.

sample and boundary scattering is fairly unimportant. This is called diffusive transport.

In addition, a range of effects are seen when ℓ is of the same order as the sample dimensions and these are classified as quasi-ballistic. By varying the sample temperature it is possible to see behaviour corresponding to first one, and then another regime. A comprehensive review of quantum transport is given in ref. [7].

1.3.2 Homogenous Magnetic Fields

Any charged particle moving in an homogeneous magnetic field experiences the Lorentz force, proportional to the particle's velocity and the strength of the magnetic field. Lorentz's law, eq. 1.1, also allows for the presence of an electric field but this will be ignored for this discussion.

$$\vec{F} = q(\vec{E} + \vec{v} \times \vec{B}), \tag{1.1}$$

where q is the electronic charge, $\vec{v}$ is the electron velocity, $\vec{E}$ is the electric field and $\vec{B}$ is the magnetic field.

The three vectors involved; force, velocity and magnetic field, form an orthogonal set due to the cross-product term. When the electrons are confined in a 2DEG, the consequence is that the electrons can only be influenced by the component of the magnetic field which is perpendicular to the plane. Components in other directions have little effect as they are attempting to move the electron out of the plane of the 2DEG which is prohibited.

As the force is always acting at right angles to the electron's velocity, the effect of the Lorentz force is to bend the electron path in to a circular orbit called a cyclotron orbit. The effect can be compared to the centripetal force as shown in eq. 1.2.

$$F = qv_F B = \frac{mv_F^2}{r}, \tag{1.2}$$

where v_F is the Fermi velocity.

This comparison leads to some useful parameters such as the cyclotron radius, r_c, re-arranged in eq. 1.3, and ω_c, the cyclotron frequency.

$$r_c = \frac{mv_F}{qB}, \tag{1.3}$$

$$\omega_c = \frac{v_F}{r_c} = \frac{qB}{m}. \tag{1.4}$$

Returning to eq. 1.1, it is possible to extract equations for the electron motion in a 2DEG under the influence of a perpendicular magnetic field. If the force is expressed as the product of mass and acceleration then the acceleration can be expressed as:

$$\vec{a} = \frac{q\vec{v}}{m}\mathbf{x}\vec{B}. \tag{1.5}$$

If the 2DEG is taken to be in the x-y plane then the perpendicular magnetic field is pointing in the z direction making it simple to separate the acceleration into x and y components:

$$a_x = \frac{dv_x}{dt} = \frac{qv_y B_z}{m} = \omega_c v_y, \tag{1.6}$$

and similarly $a_y = -\omega_c v_x$.

These coupled differential equations are simply solved to give:

$$v_x = v_F \cos(\omega_c t + \phi) \tag{1.7}$$
$$v_y = -v_F \sin(\omega_c t + \phi), \tag{1.8}$$

where ϕ is the initial angle between the x-axis and the electron's velocity.

The time evolution of the positions is also simply obtained as:

$$x = r_c \sin(\omega_c t + \phi) \tag{1.9}$$
$$y = r_c \cos(\omega_c t + \phi), \tag{1.10}$$

making the circular nature of the electron motion obvious.

1.3.3 Hall Effect

When the Lorentz force is considered for a sample of finite width in a uniform magnetic field, it is clear that the curved electron trajectories will interact with the sample boundaries. The electrons accumulate on one side of the sample and this leads to an electric field, E_H, being established which opposes the effect of the magnetic field, see figure 1.3. This is called the Hall effect and is normally measured by the Hall voltage, the potential difference between the sides of the sample.

1.3.4 Quantum Mechanical Description

The effect of a magnetic field can be considered quantum mechanically through the magnetic vector potential term, $\vec{A}$, in the momentum, $\vec{p}$:

$$\vec{p} = m\vec{v} + q\vec{A}. \tag{1.11}$$

Using the Landau gauge, the perpendicular magnetic field can be expressed as

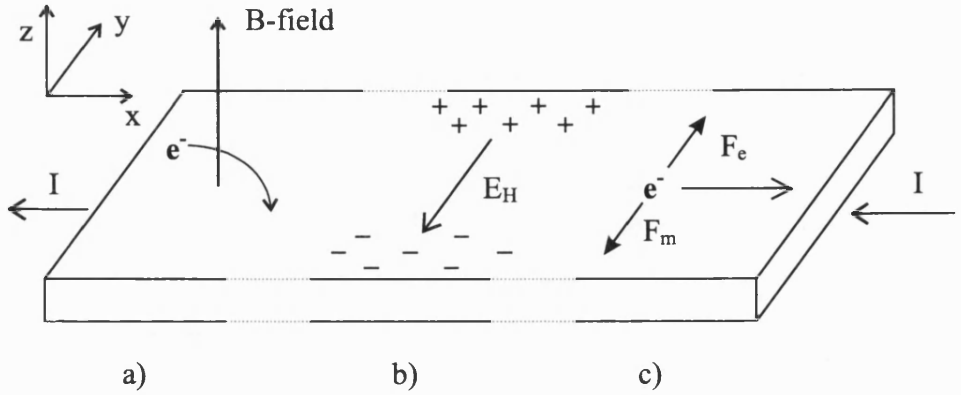

Figure 1.3: The Hall effect. a) Electrons are forced towards the near edge by the magnetic field, b) a charge imbalance develops with an associated electric force, F_e which c) cancels the effect of the magnetic field, F_m.

$A_y = B_0 x$ and the time independent Schrödinger equation becomes:

$$\frac{1}{2m}\left(\vec{p} - q\vec{A}\right)^2 \psi = \frac{1}{2m}\left(p_x^2 + (p_y + eB_0 x)^2\right)\psi = E\psi. \tag{1.12}$$

Substituting in the momentum operator $p_x = (\hbar/\imath)(\partial/\partial x)$ gives:

$$\frac{1}{2m}\left(-\hbar^2\frac{\partial^2}{\partial x^2} + \left(\frac{\hbar}{\imath}\frac{\partial}{\partial y} + \epsilon B_0 x\right)^2\right)\psi = E\psi. \tag{1.13}$$

Using the trial wavefunction,

$$\psi = \phi(x)e^{\imath k_y y}, \tag{1.14}$$

where ϕ is a function of x only, results in the final expression:

$$-\frac{\hbar^2}{2m}\frac{\partial^2\phi}{\partial x^2} + \frac{m}{2}\left(\frac{eB_0}{m}\right)^2\left(\frac{\hbar k_y}{eB_0} + x\right)^2\phi(x) = E\phi(x). \tag{1.15}$$

Comparing this to the solution for a simple harmonic oscillator:

$$-\frac{\hbar^2}{2m}\frac{\partial^2\phi}{\partial x^2} + \frac{1}{2}Cx^2\phi(x) = E\phi(x), \tag{1.16}$$

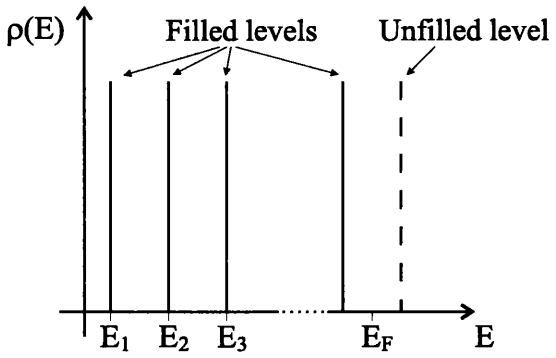

Figure 1.4: Landau Levels in a 2DEG.

several comparisons can be made. The frequency of a simple harmonic oscillator is $(\mathrm{C/m})^{1/2}$, the corresponding frequency from eq. 1.15 is eB_0/m or the cyclotron frequency, ω_c. Also, note the potential for the simple harmonic oscillator is centred at $x = 0$ whereas the magnetic solution is offset by $\hbar k_y/eB_0$.

Landau levels

The harmonic potential from the magnetic field leads to the formation of 'Landau' levels which can be seen as a quantisation of the cyclotron orbits. The energy levels, see eq. 1.17, are dependent on the magnetic field, through the cyclotron frequency, with any two adjacent levels being spaced by $\hbar\omega_c$.

$$E_n = \left(n + \frac{1}{2}\right)\hbar\omega_c. \tag{1.17}$$

Figure 1.4 shows the Landau levels as delta-functions but, in a real sample, impurity scattering and a non-zero temperature lead to the levels broadening and overlapping. It is only as the field, and so the spacing between levels, is increased that they can be distinguished.

1.3.5 Shubnikov de-Haas effect and Magnetoresistance

The quantising effect of the magnetic field can be observed through the Shubnikov de-Haas effect (or the de Haas-van Alphen effect in the magnetisation). As the

magnetic field is increased, the energy spacing of the Landau levels increases. As the levels pass through the Fermi energy, E_F, the density of states at the Fermi energy oscillates resulting in an oscillatory conductivity.

This effect can be measured by recording the sample's resistance as the magnetic field is increased. The general name for this sort of measurement is magnetoresistance, in this case, the magnetoresistance shows 'Shubnikov de-Haas oscillations'. At higher magnetic fields, Landau levels, and the spaces between them, are responsible for the integer quantum Hall effect.

The Shubnikov de-Haas effect has a practical use in determining the carrier density in the sample. The minima in the oscillations correspond to the Fermi energy being between Landau levels. This occurs with a regular spacing in B^{-1} so by indexing the minima in the magnetoresistance and plotting against 1/B, a graph, with gradient proportional to the Fermi energy, can be obtained. The Fermi energy can be related to the Fermi wave vector, k_F, and through eq. 1.19 to the carrier density, n_s.

$$E_F = \frac{\hbar^2 k_F^2}{2m} \tag{1.18}$$

$$k_F = \sqrt{2\pi n_s}. \tag{1.19}$$

The Integer and Fractional Quantum Hall Effects

The Hall effect and Shubnikov de-Haas oscillations are observable at relatively low fields, from 0 – ~1T. However, as the field strength is increased two new effects are observed. First the integer quantum Hall effect (IQHE) [8] and then at still higher fields the fractional quantum Hall effect (FQHE) [9]. Both produce similar effects in the magnetoresistance: zeros in the longitudinal resistance and plateaus in the transverse resistance at rational values of h/e^2. The features are labelled by filling factor, $\upsilon = hn_s/eB$, which can be interpreted as the number of electrons per magnetic flux quantum in the sample. As the magnetic field is increased, υ takes on smaller integer values until the crossover between IQHE and FQHE when υ becomes a fraction. Despite the similarities, the two effects have different physical origins; the IQHE arises from the quantisation of energy levels by the magnetic field whereas the FQHE is the result of electron-electron interactions.

Composite Fermions

Although the IQHE and FQHE have different origins, their similar effects led Jain [10] to introduce the concept of a composite fermion (CF) as a way of visualising the two effects. The CF is a quasi-particle consisting of an electron with a number of flux quanta bound to it. The flux quanta oppose the external field so there exists a value of the external field where the two cancel each other and the CF is effectively experiencing zero field. By various mathematical transformations it is possible to interpret the FQHE as CFs exhibiting the IQHE. Of particular interest has been the case when the electron has two attached flux quanta at $\upsilon = 1/2$ where Halperin *et al.* [11] predicted the existence of a well defined CF Fermi surface. A series of experimental and theoretical papers have show CFs exhibiting commensurability oscillations in magnetic antidot lattices [12, 13], universal conduction fluctuations [14] and extended states in random magnetic fields [15].

1.3.6 Electrostatic Modulation

The quantisation introduced into a sample by applying a magnetic field can have interesting effects when combined with a periodic electric potential. In 1989, Weiss *et al.* [16, 17] and Winkler *et al.* [18] observed oscillations in the magnetoresistance that were periodic in 1/B but at values of the magnetic field too small for them to be Shubnikov de-Haas oscillations. Their samples had potentials introduced by holographic illumination (leading to a variation in the background charge in the AlGaAs layer) and a metal grating respectively (which provided a periodic, weak electric modulation). The oscillations were explained by Beenakker [19] as a resonance in the drift of the cyclotron orbit guiding centre caused by the interaction of the periodic electric and homogenous magnetic fields; an effect well known from plasma physics. Weiss oscillations, as they became known, sparked the interest of several research groups to try and produce a similar effect using a periodic magnetic field.

1.4 Inhomogeneous Magnetic Fields

The theoretical basis for the magnetic analogue of Weiss oscillations was considered in 1990 by Vasilopoulos and Peeters [20]. However, it was not experimentally realised until 1995, when two research groups [21, 22] reported, in the same issue of Physical Review Letters, oscillations in the magnetoresistance caused by a periodic magnetic modulation. Both groups used longitudinal arrays of material fabricated on the surface of a 2DEG wafer. Carmona *et al.* used type II superconducting stripes to alter the field distribution as the external field was swept up or down. They were able to turn this effect off by heating the sample above the superconducting critical temperature. Ye *et al.* used ferromagnetic stripes of dysprosium, producing an additional field contribution. Both reported features in the magnetoresistance when the cyclotron radius was commensurate with the period of the stripes in the array.

A completely different approach to producing a varying magnetic field in the 2DEG was taken by Leadbeater *et al.* [23] who applied a uniform magnetic field to a non-planar 2DEG. In this technique, the 2DEG is grown over a patterned substrate. The 2DEG conforms to this pattern and so, locally, can be at varying angles to the applied field. See figure 1.5.

Research has continued with the inhomogeneous fields from magnetic dots and slabs becoming of interest for magnetometery (see section 1.5). Apart from the applications, there is a lot of interest in these types of samples as they have the potential to model more complicated systems such as superconductivity and composite fermions without the difficult experimental conditions.

1.4.1 Snake and Cycloid States

The combination of magnetic components with semiconductors has enabled various magnetic potentials to be investigated. Of particular interest for this report are those configurations where the electrons in the 2DEG experience magnetic fields of varying sign. As the Lorentz force depends upon the direction of the magnetic field, electrons experience opposite forces in regions having opposite magnetic field. This can result in the electrons travelling in and out of neigh-

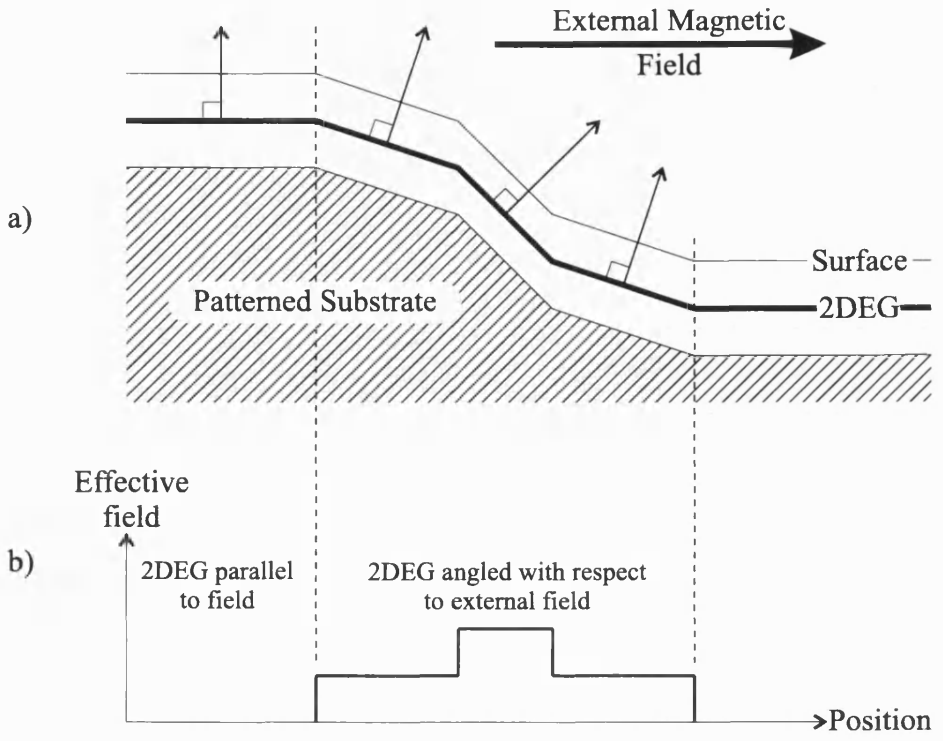

Figure 1.5: a) Non-planar 2DEG in a parallel field and b) the field experienced by electrons in the 2DEG.

bouring regions following a line of zero field. These 'snake states' are illustrated in figure 1.6 for the case of the magnetic profile from a single stripe. Alongside is a second type of trajectory called a 'cycloid orbit'. This occurs when the magnetic field in two adjacent regions is of the same sign but different strength. The electron follows a tighter circular orbit in the stronger field region and so gains an overall drift.

The quantum mechanical solution in section 1.3.4 can be expanded to include the effect of changing the sign of the magnetic field. A magnetic step from -B_0 to +B_0 at x=0 is included simply by modifying the vector potential to $A_y = B_0|x|$. The Schrödinger equation then becomes:

$$-\frac{\hbar^2}{2m}\frac{\partial^2\phi}{\partial x^2} + \frac{m}{2}\left(\frac{eB_0}{m}\right)^2\left(\frac{\hbar k_y}{eB_0} + |x|\right)^2\phi(x) = E\phi(x), \tag{1.20}$$

effectively introducing two potential wells centred at $x = \pm\hbar k_y/eB_0$. Figure 1.7a-c shows the effect of the potentials as k_y is varied. For large positive values of k_y,

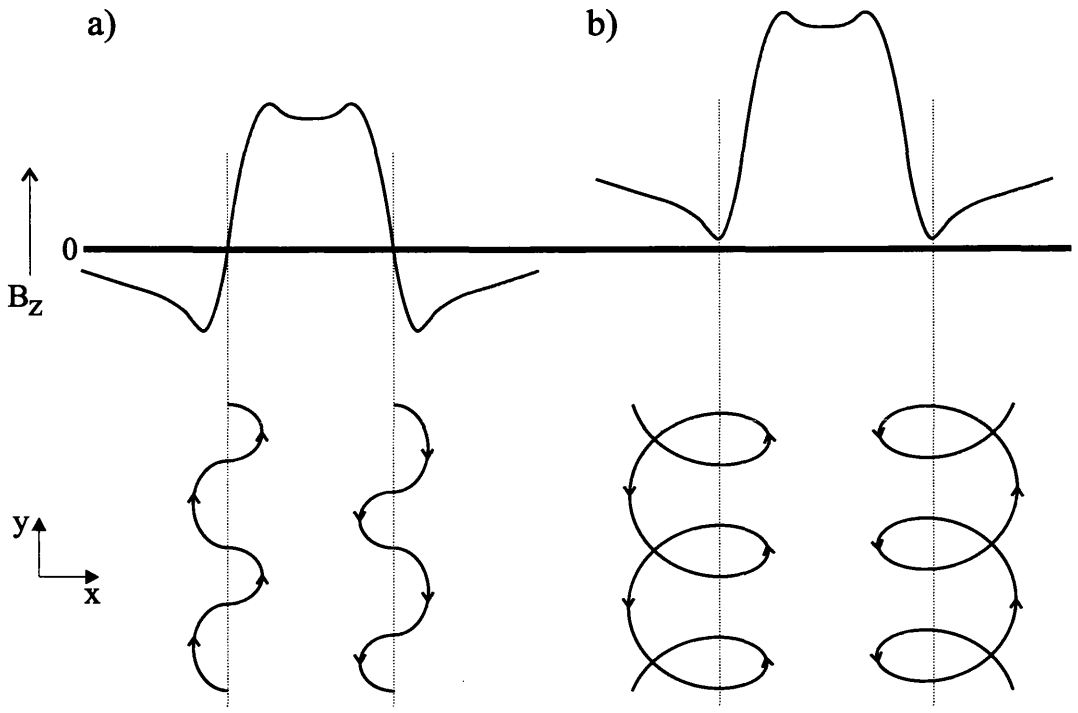

Figure 1.6: Magnetic profiles and electron trajectories for a) snake and b) cycloid states.

the two potentials are completely independent corresponding to Landau levels forming in either half of the device. As k_y is reduced, the two potentials intersect and snake states can propagate by performing parts of cyclotron orbits in either half of the device. The overlap between the potentials increases as k_y decreases until, at k_y=0, the potentials overlap. As k_y becomes negative, the resulting potential remains central but narrows and increases in energy. The consequence of this is the energy levels rise and the spacing increases. This results in an asymmetric energy dispersion curve as shown in figure 1.7d.

The situation has been considered more fully by Reijniers and Peeters *et al.* [24, 25].

1.5 Applications and Future

One of the great attractions of these devices is that they can be easily incorporated into standard semiconductor processing techniques. Applications in magnetometry [26, 27] and magnetic memory [28, 29, 30] have already been suggested. For

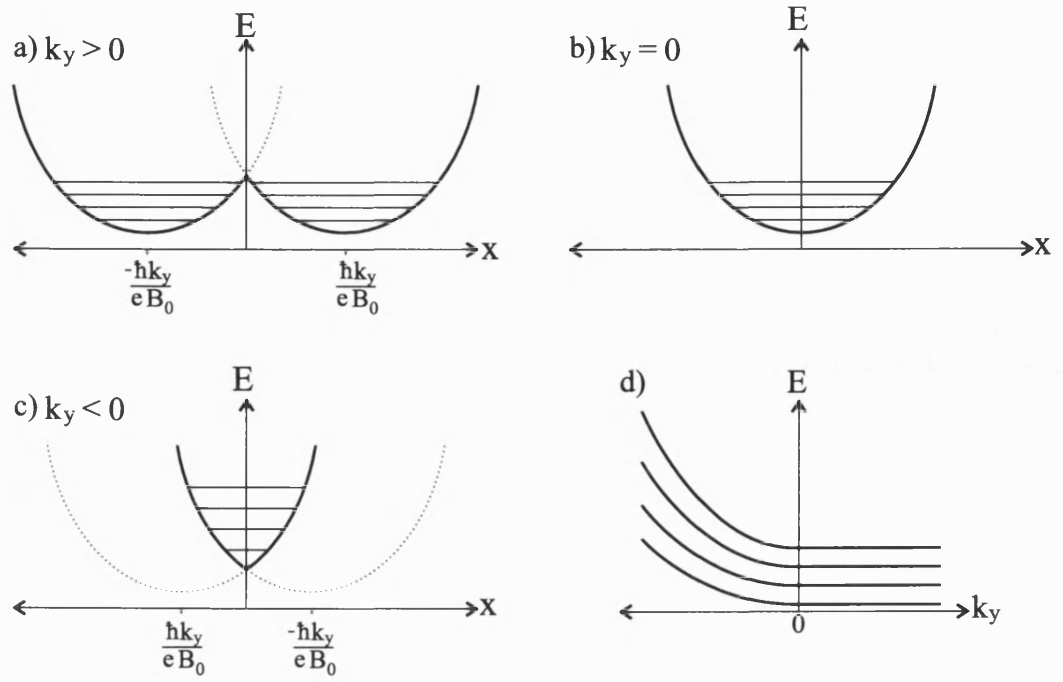

Figure 1.7: Energy levels resulting from the two potentials caused by a stepped magnetic field. a) to c) show the effect of varying k_y and d) shows the resulting energy dispersion curves.

the magnetometry, the material to be studied is deposited onto a 2DEG. The field from the material can then be studied through its effect on the electron conduction beneath.

Any device with potential memory applications is always keenly investigated as the magnetic media market constantly requires denser, cheaper and faster storage solutions. The magnetic memory applications proposed use a ferromagnetic layer partially covering a Hall cross. As the layer's magnetisation is changed, via an external field, so is the Hall resistance. The design can be modified to produce either a +/- or a low/high Hall resistance and interest has been sufficient for optimal device parameters to have been calculated [31].

1.6 The Place of This Work

In 2000, Nogaret, Bending and Henini published a paper [32] studying the effects of a single stripe of ferromagnetic material on the magnetoresistance of a 2DEG. This thesis represents the continuation of that work.

Chapter two covers the semiconductor fabrication techniques and details the experimental setup. The next three chapters report experimental results. Chapter three is concerned with possible causes of features in the magnetoresistance with a tilted external magnetic field being used to distinguish between magnetisation and channelling effects. In chapter four, the sample properties are varied by using different ferromagnetic materials, varying the stripe's dimensions and altering the 2DEG carrier density. Models based on diffusion are introduced to examine some of the parameters. Chapter five examines the response of the sample over the temperature range 1.2 to 100K to study the robustness of magnetic channelling to disorder. The penultimate chapter includes work on some features which have only reached the initial investigation stage and looks at the future directions for this work. Finally, chapter seven summarises the preceding chapters before concluding on the current state of understanding of magnetic channelling.

Chapter 2

Experimental Techniques

2.1 Introduction

This chapter details the necessary techniques for fabricating samples, as shown in figure 2.1, from GaAs/AlGaAs wafers grown by molecular beam epitaxy (MBE) and explains the measurements performed upon them. This can be a long process consisting of many small steps from the initial device design to analysing the device's response to magnetic fields.

2.2 Fabrication

When preparing a device design for a new experiment, the properties required from the wafer must be considered. As the growing techniques have been refined, it has become possible to tailor properties such as carrier density and mobility more precisely. As explained in section 1.2, by growing layers of different materials, it is possible to create two dimensional electron gases which are ideal for transport experiments. In the case of this thesis, both conventional and δ-doped 2DEG structures (see figure 2.2) have been used (wafers grown by M. Henini at Nottingham University [33]).

Equally important as the wafer is the lithographic design for the device. The

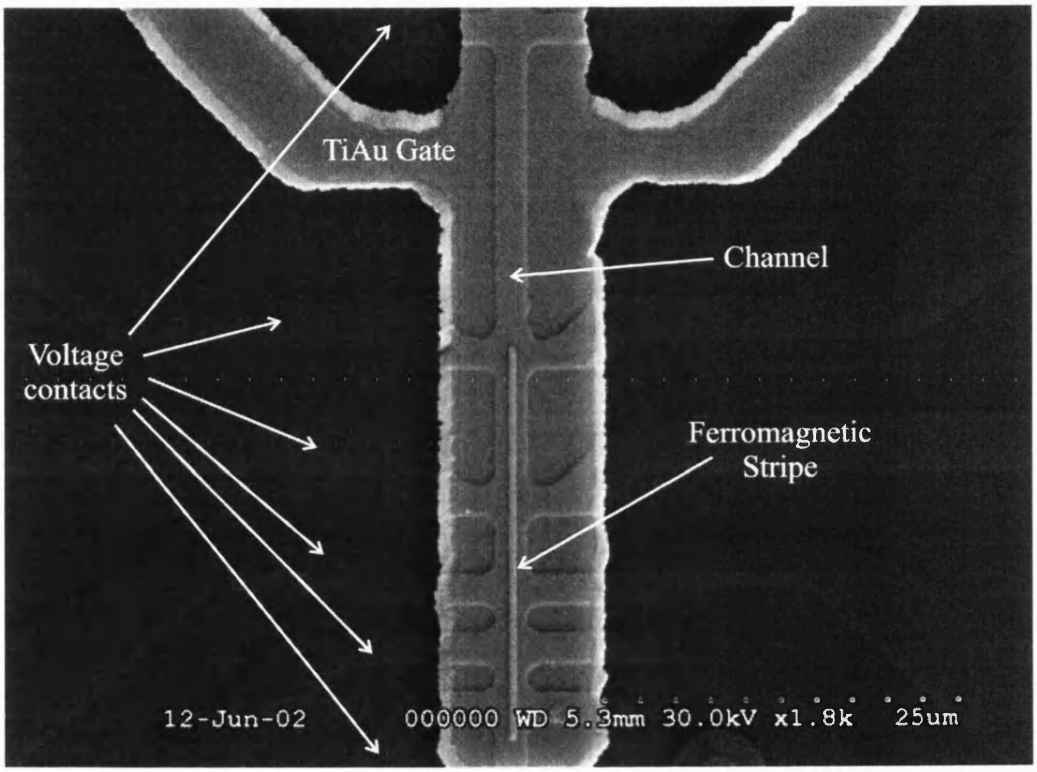

Figure 2.1: The hybrid device design incorporating a ferromagnetic stripe over a 2μm Hall bar.

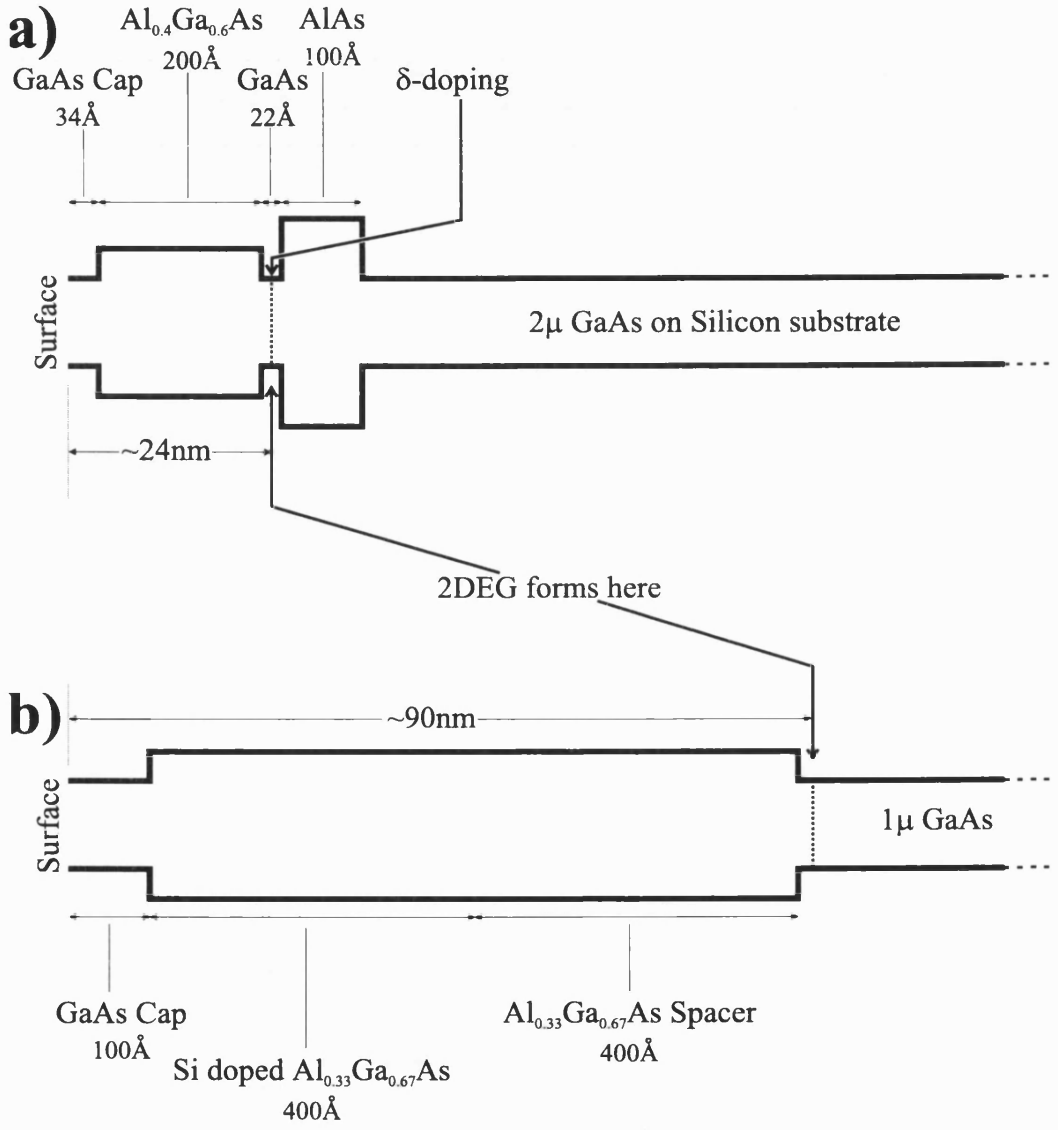

Figure 2.2: Wafer structure showing a) a shallow δ-doped 2DEG and b) a conventional 2DEG lying 90nm below the surface.

intrinsic carrier density and mobility may have been determined during growth but it is the building up of a complex set of layers via lithography which results in a functioning device. A number of design packages are available to generate patterns that can be transferred to chromium on glass 'masks' which are then used to transfer features on to the wafer. The latter process is called lithography and can involve either removing areas of the wafer or building up new layers of material. Work of this nature is carried out in a cleanroom to avoid contaminating the wafer with any impurities.

Figure 2.1 shows the area of interest for the devices in this report. The underlying structure is a long, narrow channel with contacts branching off on both sides. These branches gradually widen out to 50μm contact pads which are alloyed with a gold-germanium-nickel eutectic to contact the 2DEG and allow wires to be attached (shown in later figures). A stripe of ferromagnetic material is then deposited on top of the channel. It is this stripe that provides the inhomogeneity in the magnetic field. The device is topped with a metallic gate which covers the entire channel but is not electrically connected to the 2DEG. The following pages outline the techniques used with the details summarised in section 2.2.6.

2.2.1 Wafer Preparation

Wafers are normally received as 2.5" discs with two flattened sides to identify the <110> crystallographic axes along which GaAs cleaves naturally. However, it is impractical to work with a wafer this size so the first task is always to 'scribe' the wafer. This is simply done by moving a diamond tip into contact with the wafer surface, increasing the pressure slightly and then moving the wafer relative to the tip. As long as the scribed mark is along a <110> axis, the wafer will cleave cleanly.

To secure wafers during MBE growth, they are commonly secured with a layer of indium. This layer tends to be rough and can cause problems during fabrication so the back of the sample is 'lapped' to remove the indium. 'Lapping' is essentially polishing the reverse side against very high grade (1200) abrasive paper with the aid of polishing fluid. Care must be taken as the wafer contains arsenic and any ground off pieces are potentially dangerous.

Once the wafer has been scribed and lapped, it needs cleaning. Microposit 'soap' is a good general cleaner and is normally followed by immersion in acetone (good for removing organic contaminants), iso-propanol (to clean off the acetone) and a final washing with de-ionised water (DI). If the wafer is still dirty after this, the solvents can be heated and the sample can be agitated in the solvents using an ultrasonic bath. Again, care must be taken when setting the intensity of the agitations as collisions between the sample and its container can damage the 2DEG.

Once the wafer is satisfactorily cleaned, it is normally helpful to mount on a glass coverslip for ease of handling. A small drop of photoresist (see next section) between the sample and coverslip will, once baked, secure the wafer for the lithographic steps.

2.2.2 Lithography

It is useful to draw a parallel between lithography and photography. In the photographic process, a light sensitive layer of chemicals (typically Ag salts) is exposed to an image and records the pattern of light. The film can then be developed to reproduce the original image.

Lithography goes one step further by using the developed images as outlines for selective addition or removal of material from the wafer. The process is summarised in figure 2.3 and the individual steps are explained below.

The first element of optical lithography is the photoresist (or just resist); an organic polymer, in solution, which is sensitive to ultra violet (UV) light. There are two types of resist; positive resist where the UV weakens bonds between the polymers and negative resist where the bonds are normally weak but are then strengthened by exposure to UV. In the development stage, the weaker bonds are broken so positive resist produces a duplicate of the mask design whereas negative resist produces a negative of the mask. All the optical lithography was performed using Shipley SU1813 positive photoresist.

In the same way that photographic film must be thin and uniform, so must the resist if the mask is to be successfully transferred. To this end, the resist is

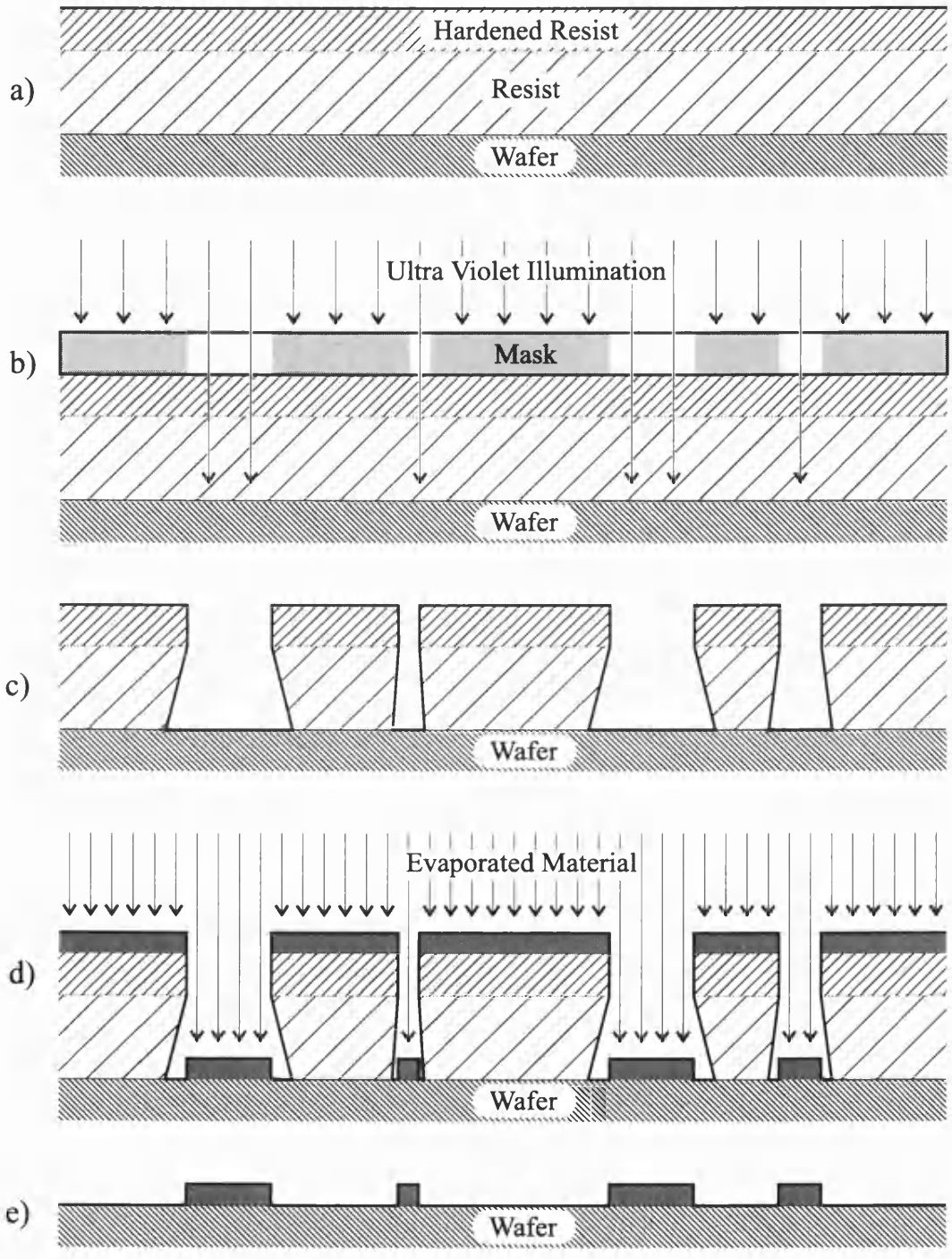

Figure 2.3: Key steps in processing: a) The wafer is prepared with resist ready for exposure, b) UV exposure of resist through mask, c) wafer and resist after development, d) deposition of new material through evaporation and e) wafer with new layer of features after liftoff.

dropped onto the wafer which is then spun at high speeds to spread the resist into a thin film. Spinning at 4000 r.p.m. for 30s leads to a layer $\sim 1.3\mu$m thick.

At this stage the resist is 'baked' for thirty minutes at 90°C to remove the solution and leave just the polymer layer. If the design requires material to be added to the wafer via 'evaporation' then the wafer is baked for fifteen minutes, soaked in chlorobenzene for fifteen minutes and then baked for a further fifteen minutes. This hardens the surface resist, as shown in part a) of figure 2.3, which facilitates liftoff as explained later.

The aim of lithography is to get an accurate transfer of the pattern from the mask on to the resist layer. This is achieved by bringing the mask into contact with the resist, shining UV light through the mask and then developing the resist (figure 2.3b). The exact exposure time varies with the age of the UV bulb but is typically around 10 seconds. Under or over exposure will make it difficult to get a sharp development but can be compensated for by altering the development time if the precision is not crucial.

Figure 2.4 shows the four layers that are used to create the devices of this report. In each case, the dark areas show where the mask is transparent. The features of the mask can be as small as one micron and so it is important that successive layers can be aligned to the previous ones to a very high degree of accuracy. To accomplish this, a 'mask aligner' is used; essentially a powerful microscope combined with x, y, z, and rotation movement stages and an ultra violet light source. The small alignment marks shown in the corners of the designs in figure 2.4 are designed purely to provide help aligning the layers.

Each resist has its associated developer; a chemical solution which attacks weak bonds and removes the polymer. Typical development times are from 20-60s, depending on the exposure time, after which the reaction is quenched by washing with DI. It is easy to see if the resist is underdeveloped by looking at it under a microscope (suitably UV filtered). The final result should show clean boundaries between the resist layer and the exposed wafer surface.

Optical lithography on conventional equipment is limited to feature sizes of around 1μm. Below this limit, diffraction effects, polymer size and microscope alignment make it practically impossible to achieve a good transfer of design to

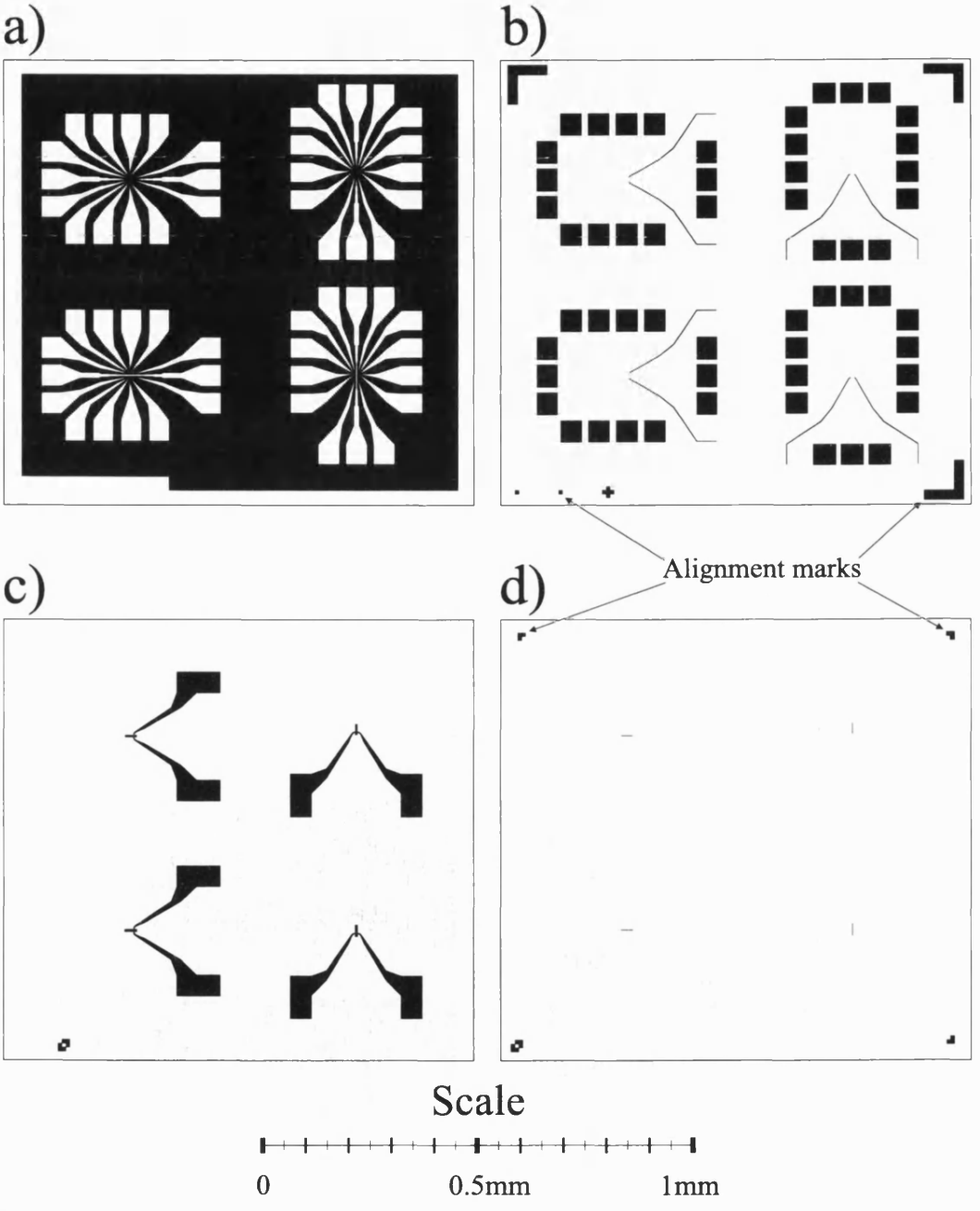

Figure 2.4: Design of the four layers for lithography. a) The layout of the device, b) ohmic contacts and e-beam guides, c) the gate layer and d) the ferromagnetic stripes (used in e-beam rather than optical lithography).

the wafer. However, smaller feature sizes of the order of 10nm are possible with electron beam lithography, as explained in section 2.2.5.

2.2.3 Etching

As the 2DEG is built into the wafer during growth, it extends over the entire area of the wafer. The first lithographic step in making a device is to isolate the layout of the device from its surroundings. Figure 2.4a shows the design of the Hall bar, dominated by the square contacts and the leads to the active area in the centre of each design. Note that this mask is different from the others in that most of the area is exposed (black). After exposure and development the Hall bar is reproduced on the wafer surface in the form of a layer of resist. The wafer must then be etched to a depth sufficient to insulate the Hall bar, typically 50-100 nm. It is not necessary to actually etch the 2DEG layer as the removal of the AlGaAs layer above destroys the confinement and depletes the 2DEG [34]. Although convenient for etching, this property also makes the devices sensitive to minor scratches so great care must be taken when manipulating the samples.

There are several different methods for etching including reactive ion etching and plasma etching but simple wet chemical etching is sufficient for these devices. A mixture of water, hydrogen peroxide and ammonia is used in the ratio 50:1:1. The hydrogen peroxide oxidises the surface which is then attacked by the ammonia. Etch rates of approximately 9 nm/s are achieved, measured by a talystepping machine, a high accuracy ($\sim \pm$5nm for the feature sizes in this thesis) mechanical machine which moves a stylus over the surface and measures the pressure on the stylus.

After etching, the sample is cleaned in acetone and isopropanol (removing the old resist) before a new layer of resist is spun on ready for the next stage of lithography.

2.2.4 Evaporation

After the sample has been etched, the basic shape of the device has been defined but there is no way to make electrical contacts to it. Parts b) and c) of figure 2.4 are both designed to allow metal layers to be added to the device. Specifically, the square holes (black) in b) allow material to be added over the contacts to the Hall bar whilst the shapes in layer c) allow for a gate to be added.

Figure 2.3c shows a wafer prepared for evaporation. The resist has been treated with chlorobenzene resulting in the near surface hardening. During development, the chemicals are more effective at removing the resist under the surface leading to an 'undercut'. Undercutting is very useful as, shown in figure 2.3d, it breaks the continuity of the metal film over the device. The material over the resist is removed when the sample is cleaned ('liftoff') but as the material on the wafer surface is not connected, it remains in place.

The principles of evaporation are not complex. Firstly, to ensure good adhesion of the evaporated materials to the sample, the wafer surface is cleaned with dilute hydrochloric acid (1:3). This does not affect the resist but simply removes any surface oxide. The samples are next loaded into the evaporator machine which is then pumped down to a pressure of $\sim 10^{-6}$ mbar. The evaporator is pre-loaded with the metals to be used. These are placed into small tungsten 'boats' (or ceramic boats if higher purity is required or if the metals react with tungsten) which are connected across the terminals of a high voltage power supply.

When the sample chamber has reached the desired vacuum, evaporation can commence. With the sample protected behind a shutter, the voltage passed through the boat is gradually increased until the metal melts and starts to evaporate. The sample is shielded to stop any contamination on the surface of the metals being deposited but after a few seconds, the shutter is opened and the evaporating metal can build up on the surface (see figure 2.3d). The rate and thickness are calculated based on an oscillating crystal whose resonant frequency shifts as the the evaporated material builds up. With knowledge of the density and acoustic impedance of the material being evaporated, it is possible to get very accurate results on the order of nanometres. This process is repeated for each required metal and the system is then left to cool before being vented to atmospheric pressure.

The final stage in the evaporation process is to remove the resist, leaving the newly deposited material on the surface. This is done by soaking the samples in hot acetone, often overnight, followed by agitation to remove any remaining resist. The result is shown in the last diagram of figure 2.3. The talystep can again be used to confirm the thickness of the deposited material.

Ohmic Contacts

The above section outlined the procedure for evaporation but the details of the metals used and their thicknesses depends on the desired function of the layer being deposited. The devices in this report require three different layers to be evaporated. The first layer to be laid down, b) in figure 2.4, is the ohmic contact layer. This is the most complex evaporation consisting of 60nm of germanium, 90nm of gold, 33nm of nickel and a further 200+nm of gold. This 'recipe' is designed to make good electrical contacts (linear I-V characteristic with low resistance) once the layers are alloyed and diffused down into the sample to the depth of the 2DEG.

The diffusion process is controlled in an annealer, a chamber with a regulated inert gas flow and a powerful illumination source which rapidly heats samples placed into the chamber. The two key factors in determining the depth to which the contacts are diffused are the temperature and time spent at that point; 15 seconds at 400°C has been found to be a good setting. On a chemical level, the process is fairly complex and still not entirely understood. Gold and germanium in the ratio 88:12 (by weight) form an eutectic alloy which melts at 360°. As the temperature increases, the germanium gold layers alloy and gallium can diffuse out of the wafer and into the alloy. Germanium can then diffuse into the wafer, replacing the gallium and forming a highly doped region. The nickel stops the surface becoming rough or 'balling' and may also aid germanium diffusion; the final gold layer helps reduce contact resistance and improves the surface morphology [35]. Examples of annealing can be seen in figure 2.5.

Following annealing, the samples are removed from the cleanroom and the I-V characteristics of the contacts are examined. If the resistances are too high or the I-Vs non-linear then there is no point continuing with the fabrication. Resistances are measured in dark conditions to reduce the effect of photo-generated carriers.

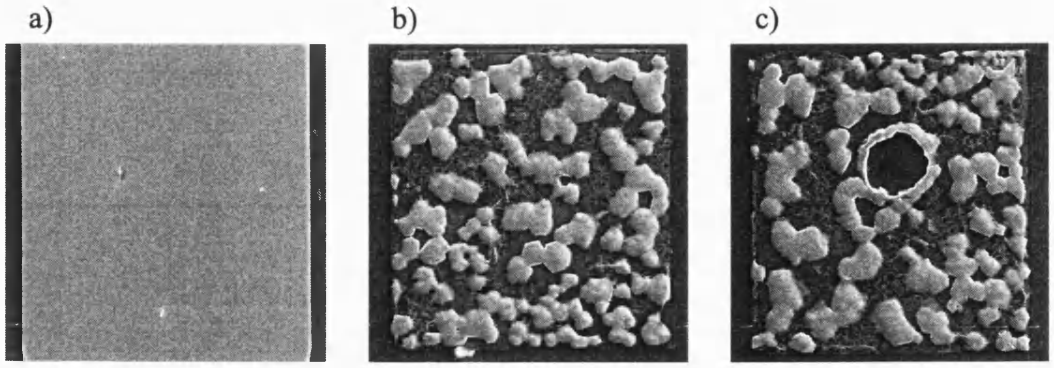

Figure 2.5: Examples of annealing on 100μm squares. a) unannealed gold, b) Ge, Au, Ni, Au annealed at 400° for 15s and c) an over-annealed contact, note the large defect.

Gate Layer

Layer c) of figure 2.4 shows the gate layer. The layer performs several useful purposes: it protects the active area from contamination and accidental damage, prevents oxidation of the ferromagnetic stripe and helps distribute stresses during thermal expansion/contraction reducing the buildup of a piezoelectric modulation. It is also used to control the electron density in the 2DEG by the application of a voltage. Placing metal layers on a semiconductor surface forces the conduction and valence bands to bend to equalise the Fermi level throughout the device, resulting in a Schottky barrier. Applying a voltage to the gate can then influence the Fermi level in the semiconductor resulting in the carrier density changing.

The gate is actually the final layer to be deposited and consists of two metals, 33nm of titanium and 200+nm of gold. They are not annealed which can make them difficult to connect wires to later as they are not securely attached to the surface.

2.2.5 Electron Beam Lithography

As stated above, optical lithography is limited to feature sizes of around 1μm. Current microprocessors, manufactured in state-of-the-art facilities have feature sizes of 0.13μm with Intel recently announcing successful 90nm processes [36] but these rely on specialised resists and exposure wavelengths bordering on the

X-ray. Electron beam (or e-beam) lithography operates on the same principles as optical lithography but with several major differences which allow features on the order of 10nm to be produced.

Firstly, different resists are used which are sensitive to electron energies but resistant to visible light. Polymethylmethacrylate (PMMA) is a common choice as it is relatively easy to work with. Spinning at 4,000 r.p.m. for 30 seconds produces a 250nm thick layer. This is baked at 150°C for 30 minutes and is then ready for use.

Another difference is the method of pattern transfer. Instead of a physical mask, the details of the feature are written by a computer controlled movement of the electron beam over the resist. This avoids the problems that can occur with mask defects, dust etc, in optical lithography and allows the device design to be altered without the need for a new set of physical masks.

The final difference is the beam itself. Using electrons reduces the effective wavelength although this is secondary to the ability to focus the beam. In practice, the final resolution is limited by the spot size and the amount of scattering from the resist and wafer surface.

E-beam lithography is ideal for small, intricate structures but is impractical for larger areas due to the time taken to raster the beam over the area. For the devices in this report, it is only used to expose the pattern of ferromagnetic stripes. The stripes are either 500 or 400nm wide and approximately 50μm long. Very good alignment is required to place them in the centre of the 2μm wide channel and parallel to it. Additional complications come from the low-contrast images of the sample and the need to avoid undue exposure of the e-beam resist. Narrow lines of gold (see figure 2.4b) are laid down with the ohmic contacts to provide a highly visible guide to the channel location.

2.2.6 Process Flow

The next couple of pages summarise all the cleanroom processing steps that are used in device fabrication.

A. Wafer preparation:

- Scribe wafer
- Lap back side
- Clean wafer

B. Isolate devices (etch):

- Spin on resist, SU1813, 30s @ 5000 r.p.m., bake 30m @ 90°C
- Align, expose and develop etch pattern
- Etch with 1:1:50 ammonia solution : H_2O_2 : H_2O for 9s (figure 2.6a)
- Strip resist

C. Define ohmic contacts:

- Spin on resist, SU1813, 30s @ 5000 r.p.m., bake 15m @ 90°C
- Soak in chlorobenzene for 15m
- Bake for 15m at 90°C
- Align, expose and develop ohmic pattern
- Prepare evaporator with Ge, Au and Ni
- Remove surface oxide with 1:3 HCl : H_2O
- Evaporate 60nm Ge, 90nm Au, 33nm Ni and 200+nm Au
- Allow to cool
- Lift off resist in hot acetone (figure 2.6b)

D. Anneal contacts

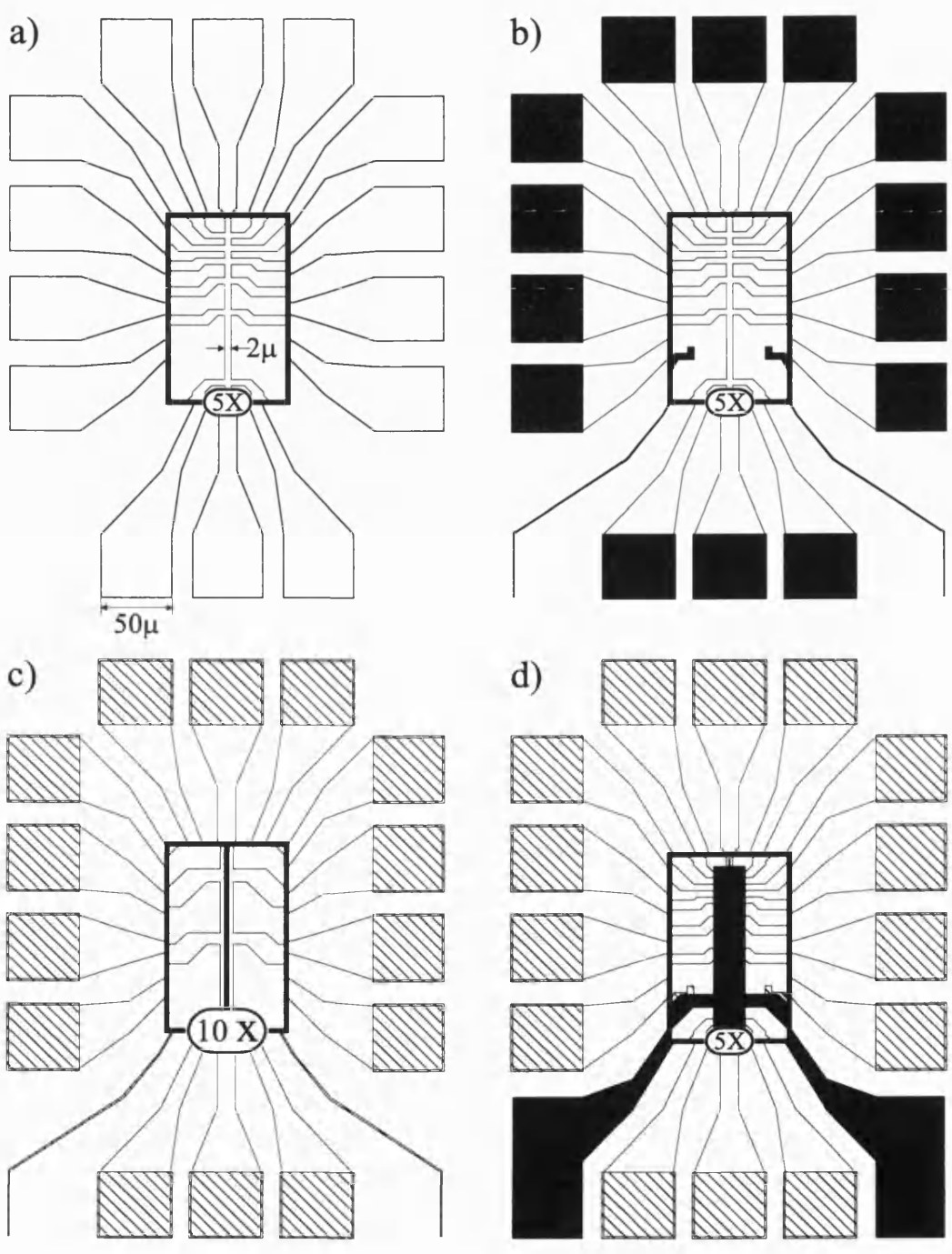

Figure 2.6: Changes in sample structure during fabrication with enlargement (5 or 10 times) of the critical central area). a) after etching, b) with ohmic contacts evaporated (black), c) with ohmics annealed (hatched) and ferromagnetic strip along the channel and d) after evaporation of the gate.

- Load sample into annealer
- Start forming gas flow
- Anneal at 400°C for 15s
- Allow to cool and switch off gas flow
- Test contact resistances and I-Vs

E. Fabricate ferromagnetic stripe:

- Clean wafer
- Spin on resist, PMMA, 30s @ 4000 r.p.m., bake 30m @ 150°C
- Load sample into e-beam machine
- Align, e-beam expose and develop stripe pattern
- Evaporate one from Ni, Fe or Dy
- Lift off resist (figure 2.6c)

F. Fabricate gate:

- Clean wafer
- Spin on resist, SU1813, 30s @ 5000 r.p.m., bake 15m @ 90°C
- Soak in chlorobenzene for 15m
- Bake for 15m at 90°C
- Align, expose and develop gate pattern
- Evaporate 33nm Ti and 200+nm Au
- Lift off resist (figure 2.6d)

2.2.7 Sample Mounting

Fabricating the gates is the last step undertaken in the cleanroom. Nothing more will be done to the structure of the device but there are still steps to be performed before the sample can be used in an experiment. These steps are all concerned with scaling up the device contacts so that instruments can be attached to the device.

In the first step, the sample is stuck to a 'chip carrier', a 10 by 10mm ceramic tile with 1mm square 'contact pads' around the edge, with GE varnish. The chip carrier can be seen in figure 2.7. The varnish is soft once heated (allowing removal if needed) but hardens as it cools, holding the sample in place.

The contact pads on the chip carrier are large enough to be accessible by a soldering iron and wire. However, it is still necessary to make contacts between the 50μm square contacts on the wafer and the pads on the chip carrier. This involves the use of a wedge bonding machine, essentially a complex needle or tip threaded with 12.5μm gold wire. The tip is threaded such that the wire passes over the tip as shown in figure 2.7. Steps a) to c) show the bonding process; in a), the tip is brought into contact with the pad in a brushing movement. At the point of contact, an ultrasonic pulse is sent through the tip which melts the wire onto the surface via thermocompression. The pulse power and duration are adjusted so that the wire is not broken but merely attached to the surface. In step b), the tip is raised, pulling wire through, and moved over the contacts on the sample. Step c) is similar to a) except that a higher power pulse is used to break the wire as it is bonded to the wafer. This step often reveals how good the fabrication has been as badly annealed contacts can flake and entire gate layers can be pulled off.

Once all the contacts have been bonded to a pad, silver epoxy is used to strengthen the bonds on the chip carrier. This is necessary as the final preparation is to solder wires onto the same pads which can easily knock off the bonds. The epoxy is baked at 120°C for 30 minutes to remove the solvent and harden.

As mentioned above, the final step is soldering wires to the contact pads. These 'sample wires' are 0.14mm in diameter and coated with enamel for insulation. The enamel can be removed from the ends by coating in solder flux and then

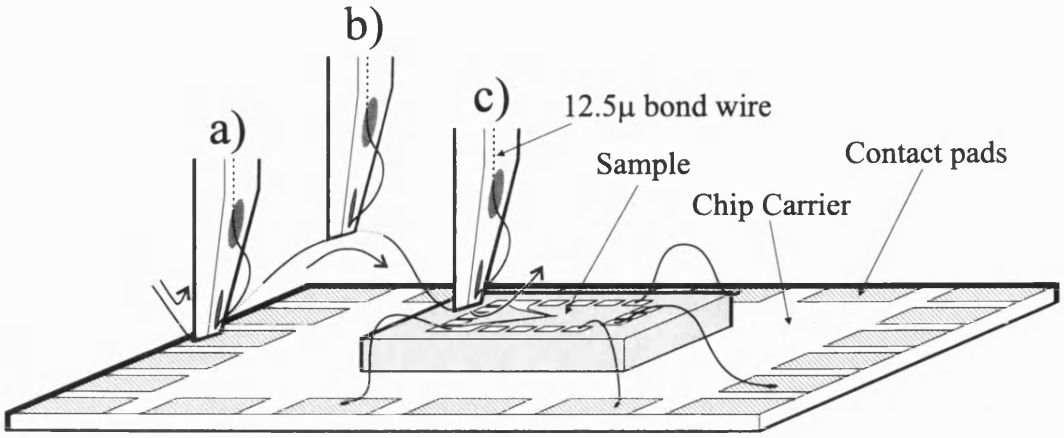

Figure 2.7: Bonding of a sample mounted on a ceramic chip carrier. Steps a) to c) show the bonding process as described in the text.

inserting into a large ball of molten solder or by scraping off with a scalpel. The wires are then soldered onto the contact pads and the other ends of the wires can be soldered into a contact box allowing connection to instruments. The only complexity with this process is the need to use indium solder as it is more reliable than lead/tin solder at low temperature.

2.3 Systems

The experimental results in this thesis were obtained on three different systems; one in Bath and two at the High Magnetic Field Laboratory in Grenoble. The Bath system is based on liquid helium cooling with a superconducting magnet capable of sweeping the magnetic field smoothly from -1T to +1T. The more heavily used of the Grenoble systems, used for most of the experimental work, was based around an Oxford Instruments superconducting magnet producing fields of up to 15T and capable of cooling to ~1.2K. Different sample holders, or 'inserts', allowed for variation in temperature and angle. The second Grenoble system was capable of producing fields of 23T and, through the use of a dilution refrigerator, temperatures as low as 20mK.

2.3.1 Achieving Low Temperatures

To perform low temperature experiments, a container is needed which can house the sample, its connectors and any other equipment which needs to be near the sample like superconducting magnets. These containers come in two types, glass dewars which are basically enlargements of the standard liquid nitrogen dewar and the more modern metal versions made by companies such as Oxford Instruments. The low temperatures are normally achieved by using liquefied gases (cryogens) to cool the components inside the cryostat. It is also possible to achieve low temperatures using closed cycle compressors but these were not used for the experiments in this report. The two common cryogenic liquids are nitrogen and helium having boiling points of 77K and 4.2K respectively. As liquid helium is considerably more expensive than liquid nitrogen, the cryostat is normally cooled first by liquid nitrogen in a process called pre-cooling. Most cryostats are designed in a concentric fashion, having different compartments for each cryogen (if liquid nitrogen comes into contact with liquid helium it will freeze potentially blocking the system). Once the system is cooled to liquid nitrogen temperatures, the liquid helium can be transferred and the system cooled to 4.2K. Another advantage of having different compartments is that liquid nitrogen can be used to provide insulating between the helium and room temperature reducing the helium evaporation.

Liquid helium is a particularly interesting cryogen, not least because of the emergence of a highly mobile helium film when it is cooled below 2.17K, the λ-point. The thin film can flow up the cryostat wall to such a height that it warms and starts to evaporate, raising the pressure and so making it harder to cool [37].

When working at low temperature it is vital to have a good vacuum in the sample space. This is because the gases present at room temperature will liquefy and then solidify as the system is cooled down. This can cause problems cooling the system but more damagingly, the gases can solidify in the pipes blocking them completely. Once this happens, there is no option but to heat the system until the blockage melts. Exchange gases, e.g. helium, are commonly used as by flushing the system with the exchange gas virtually all the atmospheric gases can be removed before the system is pumped down. It is also important to have a good vacuum between the He and N compartments.

Vacuum pumps are also important for cooling cryogens. Pumping on a cryogen removes the vapour above the liquid and reduces the pressure, lowering the boiling point. The two most commonly used pumps are the oil-sealed rotary pump (used from atmospheric pressure) and the diffusion pump (used to achieve vacuums in the range 10^{-3} to 10^{-6} mbar).

The last technique used to reduce temperature is the helium-3 dilution refrigerator. When a mixture of He^3 and He^4 is cooled below 0.9K, the mixture separates into two phases, one rich in He^3 and the other rich in He^4. The He^4-rich phase is equivalent to a superfluid with a 'gas' of He^3 atoms moving freely through it. The two phases can then be considered as He^3 liquid and He^3 vapour and by pumping on the He^3 vapour, the liquid can be further cooled. By placing the sample in thermal contact with the chamber containing the mixture, temperatures down to 20mK can be routinely achieved and sustained for prolonged periods.

2.3.2 Magnets

The construction of a superconducting magnet is very similar to a normal solenoid with turns of superconducting wire (normally a titanium niobium alloy) wound around a cylindrical core. The core diameter must be large enough to allow the sample in its holder to be inserted into the centre of the coil. Positioning is very important as the field becomes inhomogeneous towards the ends of the coil. Their advantage comes from the ability to take very high current densities with minimal resistance negating the need for a large power supply. In addition, they can be operated in a persistent field mode where the superconducting coils are shorted by a superconducting link allowing a very stable field to be sustained for as long as the wire remains superconducting.

Bitter magnets are used to obtain fields greater than ~15T. The basic principle is still one of circulating currents, normally in two or more concentric coils, but running at very high power; ~10MW for a 23T field with cooling water flows of up to $1000m^3$/hour. The magnet can cope with this much power through the use of copper Bitter plates (designed by Francis Bitter), which contain the coils, separated by insulating layers.

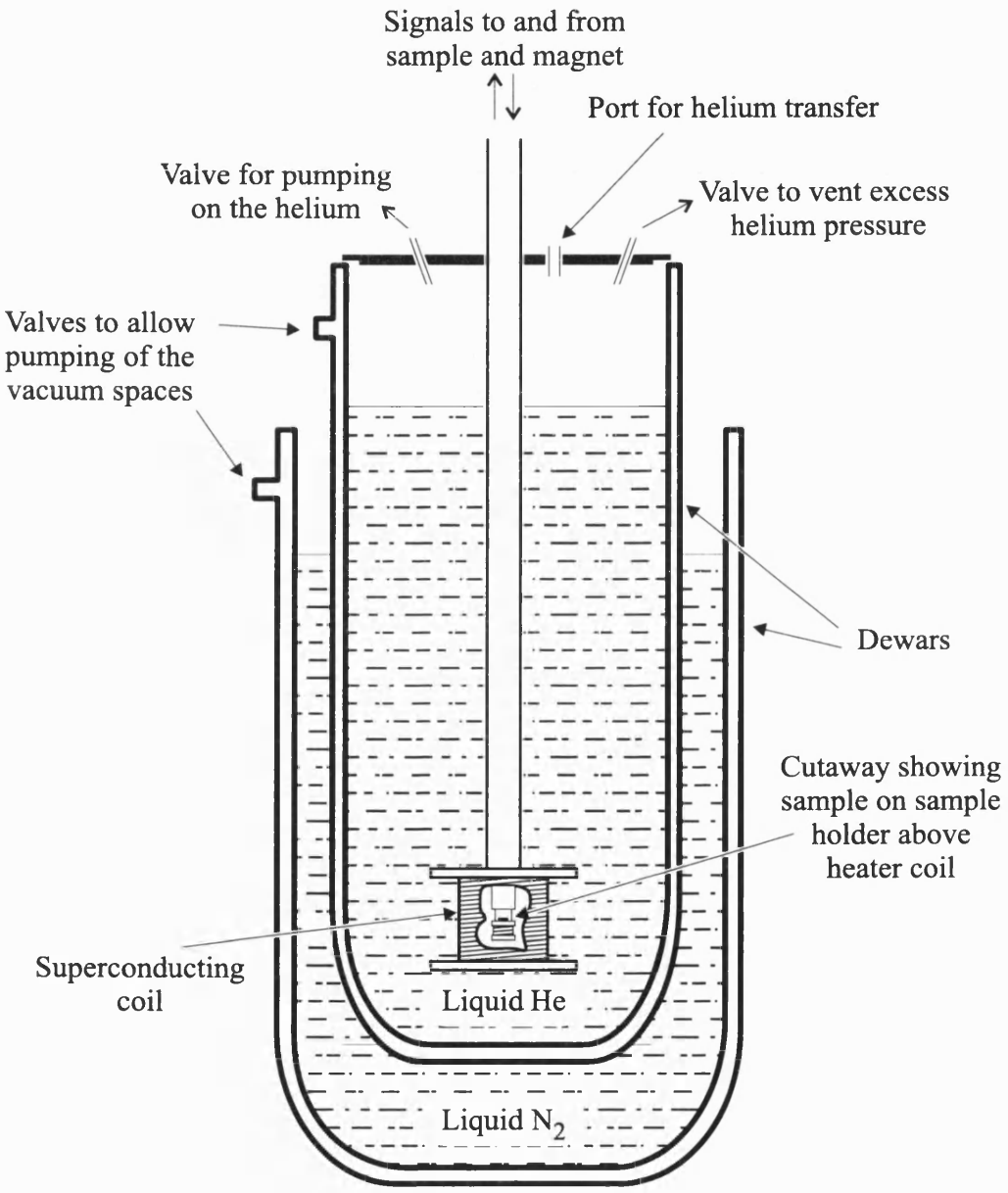

Figure 2.8: Cryostat schematic.

2.4 Measurement Techniques

Once the sample has been fabricated, cooled and subject to magnetic fields there is still the issue of how to measure its properties. Magnetotransport measurements are based on recording the resistance of the device whilst currents are passed through it in the presence of a magnetic field. The simplest method is to pass a known current through two probes and record the voltage drop across the same two probes (a standard multimeter style measurement). This is called a two terminal measurement and is normally avoided as combining the current and voltage contacts results in measuring the large contact resistance as well as the actual device resistance. A superior technique is to use four contacts.

The whole design of a Hall bar is based around the idea of four probe measurements. Two probes, often at either end of the active region, are used to send a current through the device, a further two probes, situated between the current contacts, are monitored to measure the voltage drop between them. This avoids measuring the contact resistance and so the reading can be very accurate. If the voltage probes are situated after the current probes, a 'non-local' measurement is being performed where the effects of the current are being studied indirectly.

In the following experimental chapters, two different types of basic result will be presented. These will be either R_{xx} or R_{xy} measurements. The subscripts refer to the direction the current is applied in and the direction the voltage drop is measured in; x is conventionally taken to be along the channel and y across the channel. As can be seen, the current is always applied along the channel but the voltage drop can be recorded either along the channel, giving the conventional resistance, or across the channel which is a classical Hall effect measurement.

2.4.1 Typical Experimental Setup

Figure 2.9 shows, schematically, the relationship between the sample, instruments and controlling computer for a DC measurement. a) and b) are programable voltage supplies to provide the sample voltage and gate bias. c) and d) are voltmeters; c) measures the voltage drop between the contacts being studied (either R_{xx} with the dotted line or R_{xy} with the dot-dash line) whereas d) measures the voltage

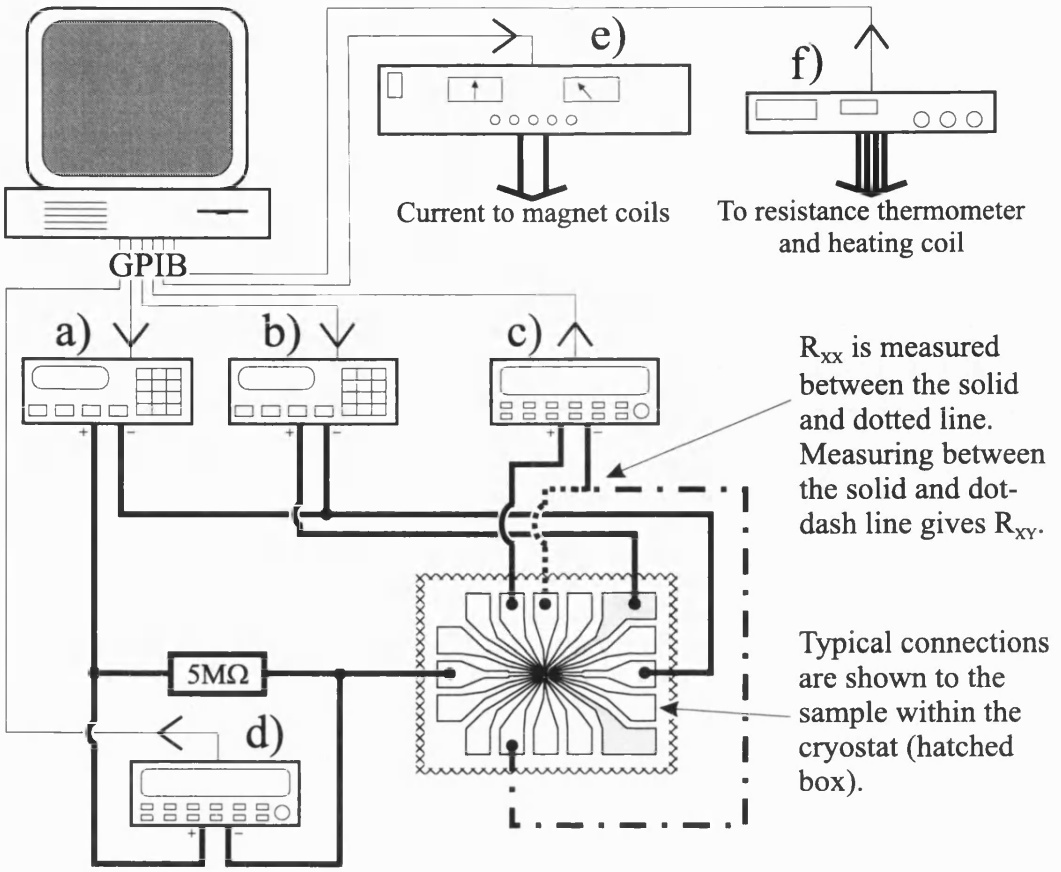

Figure 2.9: Experimental setup for DC measurement. See text for explanation.

drop across the resistor to determine the sample current. A large resistance is used so that the variations in the device resistance have a negligible effect on the current. e) is the magnet power supply and f) measures the temperature and can also be used to heat the sample by passing a current through a small coil around the base of the sample holder. All the instruments are connected to the computer using the G.P.I.B protocol. The computer runs a custom written data acquisition program which is capable of setting or sweeping the magnetic field, sample voltage and gate bias whilst recording the temperature and voltage drops across the sample and resistor.

AC magnetotransport measurements can be performed by replacing a), c) and d) with lock-in amplifiers. 7Hz was found to be a good operating frequency. However, most of the experiments were performed with a DC setup as it was anticipated that the I-V characteristics would be asymmetrical due to the asymmetric energy dispersion curves of snake states.

Chapter 3

Magnetic Channelling

3.1 Introduction

The last two chapters have explained the key pieces of research and the experimental techniques that have made this thesis possible. The next four chapters are concerned with the investigation of magnetic channelling in hybrid ferromagnet/semiconductor structures. This chapter examines the results from initial magnetoresistance experiments, outlines the alternative explanations for the observed results and explains why magnetic channelling via snake and cycloid states is the most viable current explanation.

3.1.1 Commensurability Oscillations

As explained in chapter 1, the impetus for studying magnetic structures on semiconductors came from Müller's paper [38] in which he studied electron transport in a non-uniform magnetic field and work by Vasilopoulos and Peeters [20] who predicted the magnetic equivalent of the commensurability oscillations observed in electrostatically modulated devices. Subsequent work with arrays of magnetic stripes [22, 21, 39] eventually led to the observation of resistance resonance peaks [32] with single stripes of nickel and iron. This chapter commences by examining initial results for a dysprosium stripe (the comparison with earlier results

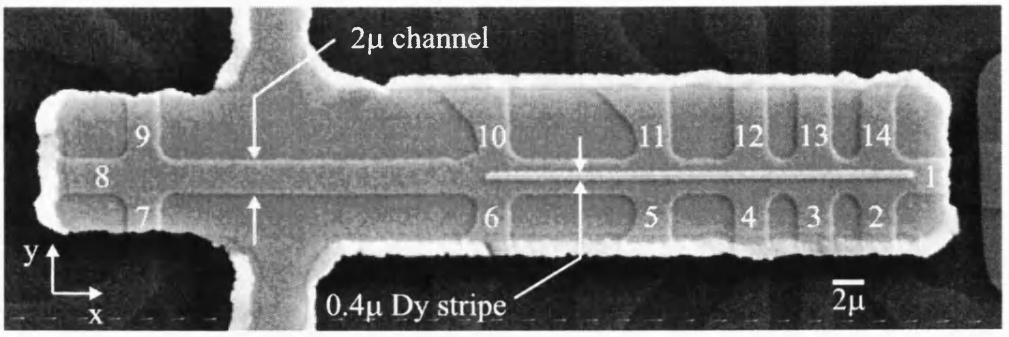

Figure 3.1: A typical 2μm channel device with a 400nm dysprosium stripe.

will be covered in chapter 4). Ref [32] contains an explanation of the effects seen but alternative theories have also been put forward. The main purpose of this chapter is to study the possible causes and provide the basis for understanding the following chapters.

3.2 Initial Experiments

Figure 3.1 shows a typical device as used for the measurements in this chapter. It consists of an AlGaAs/GaAs/AlGaAs δ-doped 2DEG (silicon doping level, $N_D = 3 \times 10^{12}$ cm^{-2}) formed 24nm below the surface. The 2μm channel has voltage contacts with separations varying from 4μm to 24μm on both sides of the channel to allow Hall and magnetoresistance measurements to be made. The dysprosium stripe at the centre of the channel is w = 400nm wide and h = 140nm high. The channel was defined by optical lithography and etching, the stripe by e-beam lithography and evaporation. Over the active area is a TiAu gate layer which serves to distribute stress evenly, protect the dysprosium from oxidation and allows manipulation of the carrier density in the 2DEG.

It is the presence of the dysprosium stripe which makes this device differ from a standard Hall bar. Dysprosium is a ferromagnetic element and, when magnetised, the field it creates will have an influence on the electrons in the 2DEG beneath. As explained in section 1.3.2, the confined electrons will only be affected by fields perpendicular to the plane of the 2DEG, i.e. the z-component of the field from the stripe.

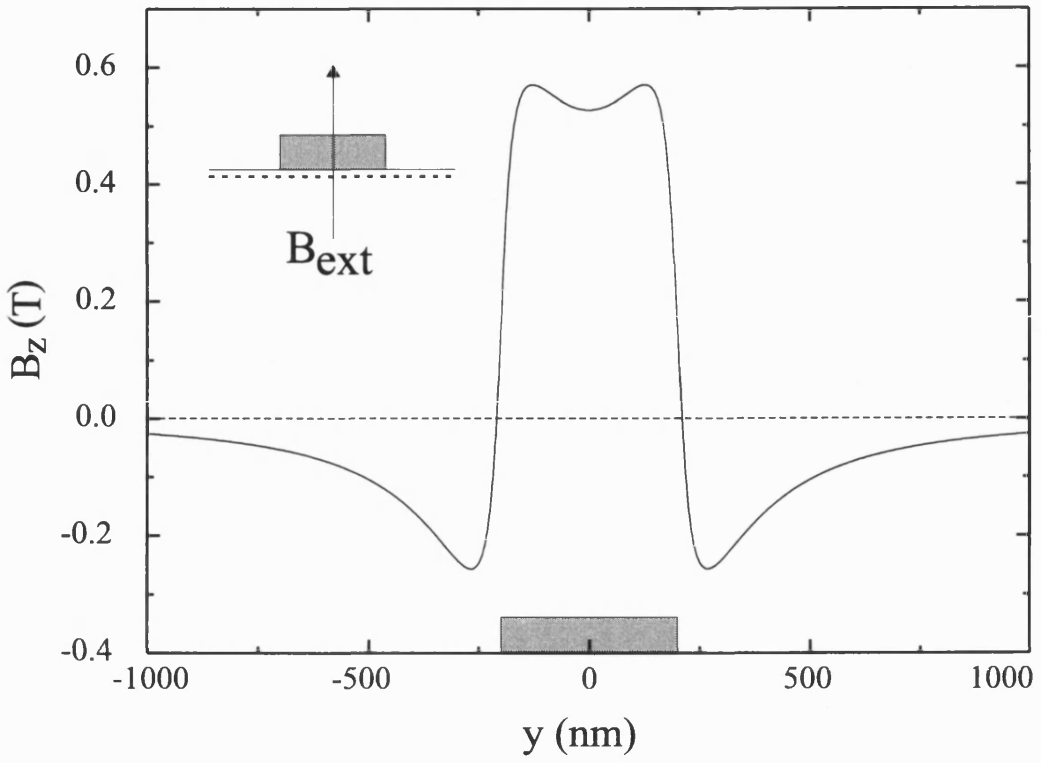

Figure 3.2: The field profile formed under a perpendicularly magnetised stripe with uniform magnetisation.

The commonest sample geometry in this report has the stripe magnetised perpendicular to the device to give the field profile shown in figure 3.2. The profile is given by (ref. [40]):

$$B_z(y) = \frac{M_s}{2\pi}\left(\arctan\left[\frac{y}{z}\right] - \arctan\left[\frac{y-w}{z}\right] - \arctan\left[\frac{y}{z+h}\right] + \arctan\left[\frac{y-w}{z+h}\right]\right) \tag{3.1}$$

where M_s is the saturation magnetisation of the ferromagnet (2.92T for dysprosium [41]), z is the distance of the 2DEG below the surface, w is the width of the stripe, h the height and y is the distance from the edge of the stripe.

As the direction of the magnetisation of the stripe changes, so does the B_z profile. Eq. 3.2 describes the magnet profile when the stripe is magnetised in the plane of the 2DEG but at ninety degrees to the direction of the channel [40]. Figure 3.3

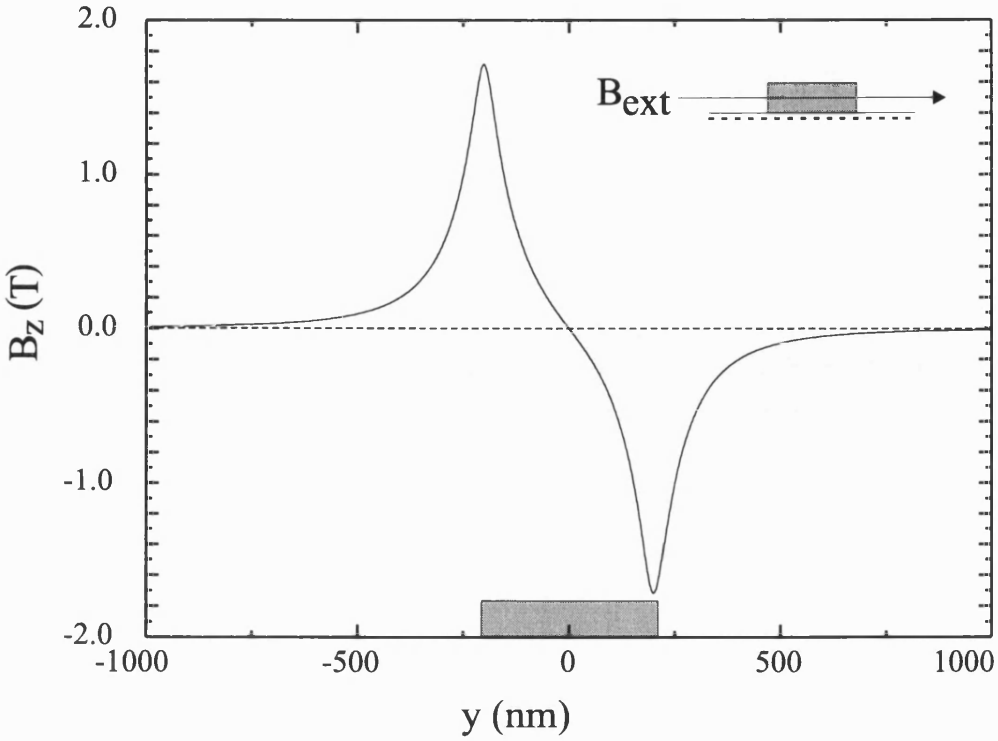

Figure 3.3: The field profile formed under a stripe magnetised parallel to the plane of the 2DEG but perpendicular to the channel direction.

shows this geometry and the profile that would arise from the device parameters given above.

$$B_z(y) = \frac{M_s}{2\pi}\left(\ln\sqrt{\frac{(z+h)^2+y^2}{z^2+y^2}} - \ln\sqrt{\frac{(z+h)^2+(y-w)^2}{z^2+(y-w)^2}}\right) \tag{3.2}$$

Precisely how the stripe magnetises forms a key part of any explanation of magnetic channelling and is considered in detail later in this chapter. Initially, it is assumed that the stripe is always fully magnetised, i.e. the stripes are perfect ferromagnets.

In addition to the magnetic field from the stripe, the sample is also in the presence of a uniform, applied magnetic field referred to as the external or applied field. In the first results of this section, the external field and the stripe magnetisation are aligned, both being perpendicular to the device. As the external field is perpendicular to the 2DEG, the electrons will experience the sum of the external field, B, and the contribution from the stripe.

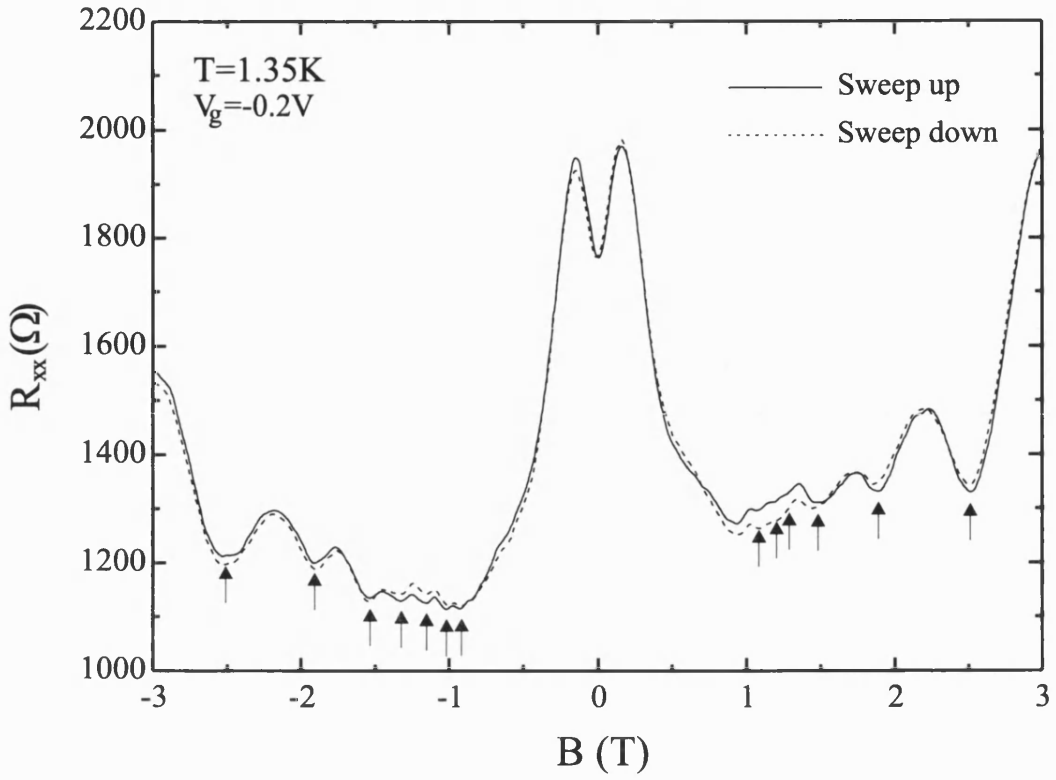

Figure 3.4: The magnetoresistance resonance peak in a sample with a dysprosium stripe. The arrows highlight the minima of the Shubnikov-de Haas oscillations.

3.2.1 Initial Measurement

For the results shown in figure 3.4, a 1mA current was passed along the length of the channel between the contacts labelled 8 and 1 in figure 3.1. The voltage between the third and first contacts, 4 and 2 (spacing 8μm), was recorded as the external field was increased from -3T to +3T. The recorded voltages allow the resistance to be calculated as plotted in figure 3.4 (dashed line shows the trace when the field was swept in the opposite direction). Standard features such as the Shubnikov-de Haas (SdH) oscillations (the minima are indicated by arrows) and the approximate symmetry around B=0 are obvious. However, there is also an unusual structure with peaks at $\pm$0.15T and a dip at zero field which shows very little hysteresis.

The influence of the stripe can also be seen on the Hall resistance. For figure 3.5 the voltage was recorded between contacts 4 and 12 across the channel as the field was again swept from -3T to +3T. The Hall resistance is normally considered to be proportional to the average magnetic field in the area of measurement; as such

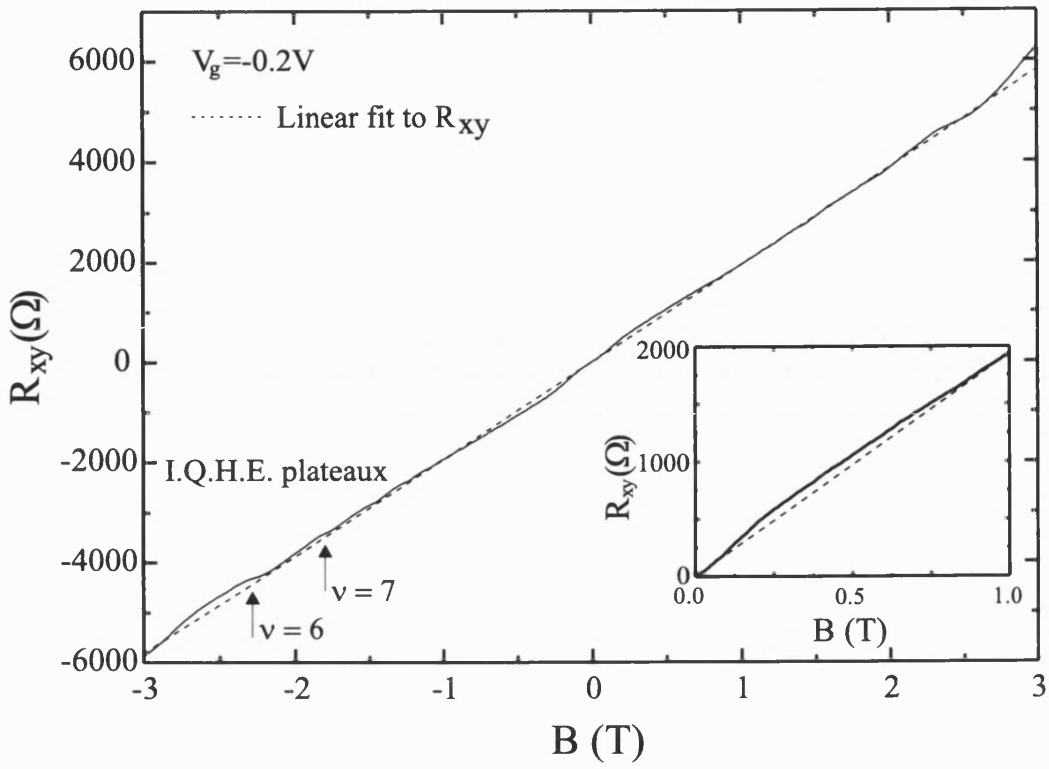

Figure 3.5: The Hall resistance for the same sample as figure 3.4. Inset shows enlargement from 0-1T illustrating the non-linear behaviour.

it is generally linear but the curve clearly departs from this behaviour as the field varies between ±1T. The deviations at higher field show the emerging integer quantum Hall effect (IQHE) and are not connected to the stripe's presence.

Figures like 3.4 and 3.5 also allow the carrier density, n_s, and mobility, μ, to be calculated. At low field, the gradient of the Hall resistance, $R_{xy} = B/n_s e$, can be used to accurately determine the carrier density. For a zero-bias sample the gradient was found to be 1642 m^2C^{-1} giving $n_s = 3.8 \times 10^{11} cm^{-2}$.

The Drude model [4] gives a good description of electron transport in low fields. Two useful quantities arise from it, the first being mobility, μ:

$$\mu = \frac{e\tau}{m^*} \tag{3.3}$$

where τ is the scattering time and m^* is the effective mass of the electron in the semiconductor.

The second useful quantity is the Drude resistivity:

$$\rho = \frac{1}{(n_s e \mu)} \tag{3.4}$$

As n_s has already been found for this sample, eq. 3.4 can now be used to calculate the mobility. For a zero-bias sample, the longitudinal resistance at B=0 is 240Ω, the contacts were separated by 8μm and the channel was 2μm wide so the resistivity is $\rho = R_{B=0} \times \frac{2}{8} = 60\Omega$ and the mobility $\mu = 1/\rho n_s e = 2.7 \times 10^5$ cm^2/Vs.

3.3 Magnetic Channelling

An explanation for the observed peaks around B=0, based on the stripe's magnetic field creating guided trajectories through the device, was put forward in ref. [32]. The effect of these guided trajectories will now be explained. Figure 3.6 shows the peak from figure 3.4 split into three regions where the different trajectories are active.

3.3.1 Snake States

The first region of figure 3.6 shows a monotonically increasing resistance with increasing magnetic field. At B=0, the only field influencing the sample is that from the stripe. As shown in figure 3.2, the field is negative away from the stripe and positive under the stripe. This modulation ranges from -0.26T to +0.57T and it is the change in sign which allows the first type of guided trajectory, snake states, to form. If the field changes sign then so will the Lorentz force meaning that electrons with parallel trajectories will experience opposite forces under and away from the stripe. As shown beneath the curve in figure 3.6, the electrons can be continually guided towards the B_z=0 line resulting in a 'snaking' motion through the device. Not all electrons will be guided in these states as the negative modulation is not large enough to sufficiently bend all the electrons in before they collide with the finite channel boundaries. However, those that are guided will

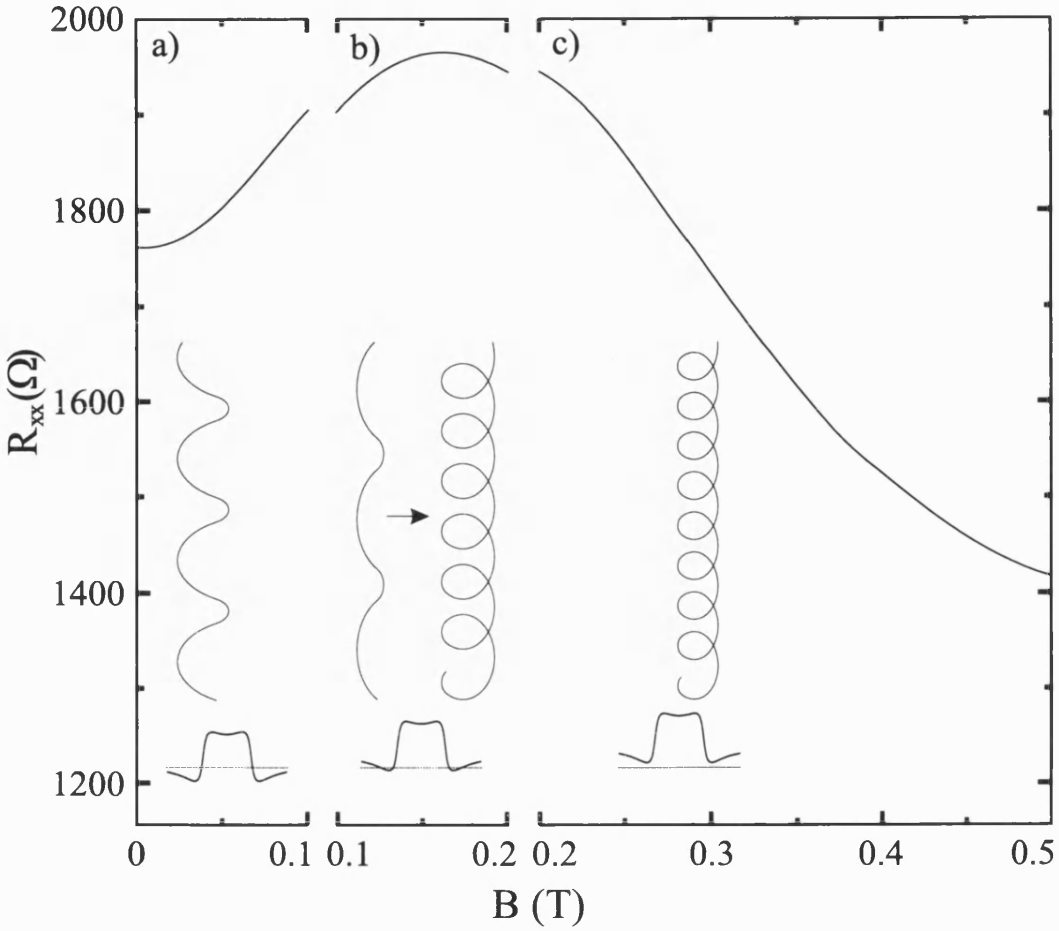

Figure 3.6: The effect of snake and cycloid states on the magnetoresistance. a) Snake states dominate at low field, b) snake states die away and cycloid states emerge and c) cycloid states dominate the resistance.

enhance conduction through the device and hence lower resistance.

As the external field is increased, the electrons experience the sum of the modulation from the stripe (unchanged by the external field) and the positive external field. The result is to reduce the negative modulation both in magnitude and the area of the sample it covers which reduces the number of electrons guided in snake states. As long as there is still an area of negative modulation in the sample, snake states can propagate but the number of guided electrons diminishes as the external field is increased resulting in the increasing resistance shown in figure 3.6.

3.3.2 Cycloid States

The second type of guided trajectory occurs when the negative modulation has been cancelled out by a sufficiently large external field. In this case, the Lorentz force will always be rotating the electron trajectories in the same way but the radius of curvature will be smaller under the stripe than in the regions not covered by the stripe. This difference in curvature leads to a cycloid state as illustrated on the right of figure 3.6. The resistance in this region is monotonically decreasing as the external field increases. With snake states, the external field was decreasing the number of guided electrons whereas for cycloid states, the external field increasing can trap more electrons into the guided trajectories. However, this effect is eventually cancelled out as the size of the original modulation from the stripe becomes smaller relative to the external field.

There is not a sharp transition between the two regions, as shown in the central region of figure 3.6. Although the snake states are quenched as soon as the negative field regions disappear, cycloid states can pass through small regions of negative field and develop gradually over the end of the snake states region.

3.4 Alternative Explanations

The snake state picture, presented above, is only one possible explanation for the resistance peaks. It is based on the assumption that the stripe is magnetised perpendicularly before any external field is applied and treats the electrons in a classical sense.

The assumption about magnetisation requires further examination. Work by Ye and Weiss *et al.* [22, 42] on arrays of dysprosium stripes and dots, showed that the dysprosium was gradually magnetised as the external field was increased. However, this does not rule out channelling. If the magnetisation process occurs rapidly enough for the negative modulation to be greater than the applied field, channelling can still occur. Some support for a hard magnetisation comes from work by Legvold [43] which shows a sharp transition at low fields but is based on crystalline dysprosium rather than the polycrystalline situation found when dysprosium is evaporated.

Dysprosium's polycrystalline nature adds the possibility of the field being more randomised than the profiles in figures 3.2 and 3.3 would suggest. Work on samples with CoPd multi-layers by Rushforth *et al.* [44] has shown that as the layers pass through a random domain orientation phase, the resistance increases as a result of decreased diffusivity. Further work, measuring the actual magnetisation of dysprosium for these devices is clearly required to determine the true situation.

Two other effects have been suggested to explain the peak structure and the rest of this chapter looks at these explanations, one based on the behaviour of narrow channelled devices and the other on a quantum mechanical model of the device.

3.4.1 Magnetosize Effect

At first glance the peaks look similar to those seen in narrow quantum wires with no ferromagnetic stripe [45]. Thornton *et al.* [46] studied the effect in detail, observing peaks in channels ranging from 0.13μm to 1.15μm wide which can be explained by considering boundary scattering. Figure 3.7 shows what can happen in a narrow channel when a small magnetic field is applied. The slight curvature of the trajectories directs the electrons towards the boundary walls. Scattering is thought to be largely specular (angle of reflection = angle of incidence) in these devices but a small diffusive (angle of reflection $\neq$ angle of incidence) component can result in the electrons being backscattered and the resistance increasing. In a large field, the backscattering is suppressed and the resistance falls again (figure 3.7 illustrates these points). Theory and experiment agree that the peak should occur when the channel width, d, is approximately half the cyclotron radius, r_c.

It is fairly simple to discount the size effect as the devices in this thesis have wider channels and, as has already been shown, the peaks can occur at fields of up to 0.1T whereas $r_c/2$ would be $\sim$ 0.05T for the dysprosium sample above. Figure 3.8a shows a 2μm sample with an iron stripe and lower carrier density where the peak position of 0.022T is close to the $r_c/2$ value of 0.02 (lower n_s leads to a smaller Fermi velocity and smaller cyclotron orbits). However, conclusive evidence is provided in figure 3.8b where the magnetoresistance of a 2μm sample fabricated without a stripe is shown. This displays only a gradual decrease in resistance until $\sim$0.3T where the cyclotron orbits become comparable in size to

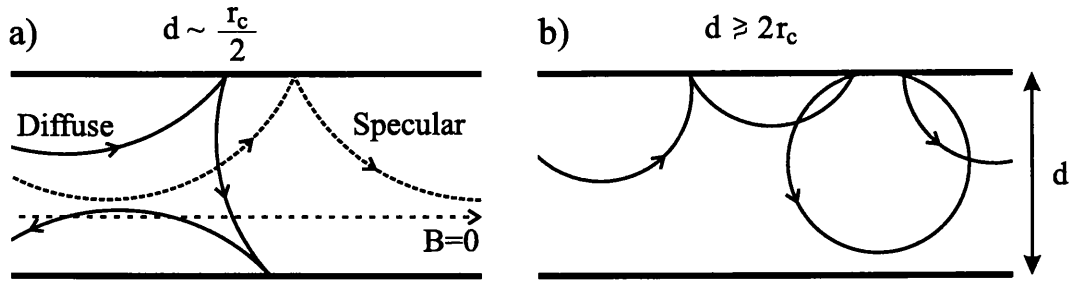

Figure 3.7: The size effect in a narrow channelled device. a) diffuse boundary scattering leads to backscattering of electrons and b) a sufficiently large field removes the possibility of backscattering.

the channel width and the resistance starts to rise again. Note that this is a graph of normalised resistance where the sample resistance is divided by the zero-field value. This makes it easier to compare the magnitude of the effect in samples with different resistances. The clear absence of a peak in the no stripe sample shows the size effect does not explain the resistance peaks.

3.4.2 Magnetisation

An alternative explanation was put forward by Reijniers and Peeters in 2001 [47] when they considered different cases of ferromagnetic behaviour for the stripe; whether it was a *hard* ferromagnet (magnetised with a negligible external field) or *soft* (magnetisation proportional to the external field until it saturates). Reijniers and Peeters' theory (based on the Landauer-Büttiker formula) suggested the soft case would give better agreement to the experimental data. They argued that as the stripe magnetised it tended to localise electrons into cyclotron orbits. As the external field increased, their energy spacing also increased resulting in fewer channels intersecting the Fermi level and hence reduced conduction. The decrease in resistance then arose through the rise of cycloid states and other orbits skipping along the sample edges.

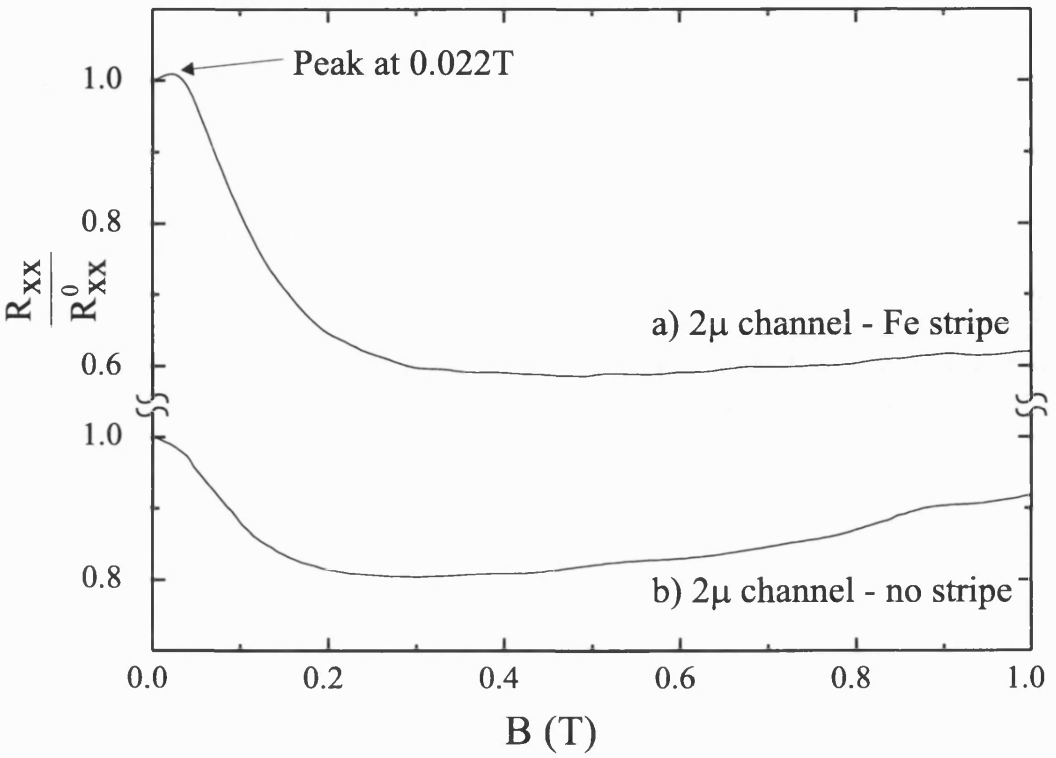

Figure 3.8: Magnetoresistance for samples with a) 2μm channel and an iron stripe and b) a 2μ device with no stripe.

3.5 Rotation Experiments

One way to distinguish between the modulation explanation, based on snake and cycloid states, and the magnetisation approach is to study the behaviour as the angle of the applied field is changed. The magnetisation of the stripe should depend simply on the magnitude of the external field whereas, if the modulation approach is correct, the peak should occur at a constant value of the field perpendicular to the 2DEG. All the experiments in this section were performed at Grenoble using a rotation stage (orientation shown in figure 3.9) at a temperature of 1.3K. The angle θ is defined relative to the external field being perpendicular to the device, i.e. the angle between the applied field and the normal to the 2DEG, hence $\theta = 90°$ refers to the magnetic field being in the plane of the 2DEG.

The rotation probe was calibrated by studying standard properties of the magneto- and Hall resistances (plotted in figure 3.10) and comparing the derived value of n_s to those obtained from the same sample on a normal mounting stage. The

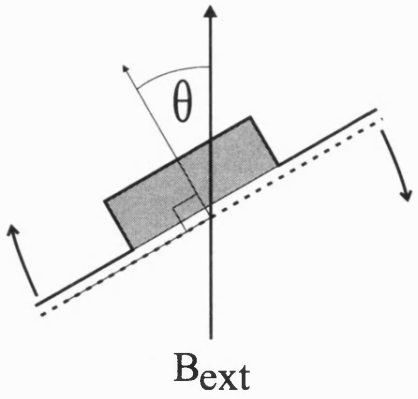

Figure 3.9: Orientation of the sample and rotation insert.

shifting spacing of the SdH minima oscillations, B_f, can be converted into an angle using $n_s = (2e/h)B_f \cos(\theta)$ (♦), the Hall co-efficient, $R_H = (-1/n_s e)\cos(\theta)$ can also be used (■). The rotation probe also had an indicator of the number of turns applied to the gears that rotated the sample, shown as the x-axis on figure 3.10, where 4.16 turns gave $\theta = 90°$ and 14 turns corresponded to $\theta = 0°$ (•). Overall, the agreement between the three measurements was excellent with a discrepancy of $\sim \pm 0.8$ degrees.

3.5.1 R_{xx} and R_{xy} vs B

Figure 3.11a shows a series of magnetoresistance traces, offset for clarity, recorded at different sample rotations. The solid line shows the $\theta = 0°$ result with the peak position occurring at 0.15T. As the angle is increased, the peak position increases until it reaches 1.08T at $\theta = 81.9°$. Apart from the $\theta = 89.1°$ trace and allowing for the offset, the curves all follow the same shape with a rise to the peak, a large reduction in the resistance and the gradual introduction of the SdH oscillations. This figure clearly demonstrates that the peak position is not directly related to the magnitude of the external field.

Figure 3.11b shows the quantity R_{xy}/R^0_{xy} against B. R^0_{xy} is a linear fit to the R_{xy} data and, therefore, the graph shows the deviation from the linear Hall resistance or the normalised Hall resistance which is more useful to study. Again the curves are offset for clarity but it is obvious that the peak position follows a similar trend to the R_{xx} traces but with the peaks occurring at higher field values for each angle respectively. It is also noticeable that the curves all tend to a value of

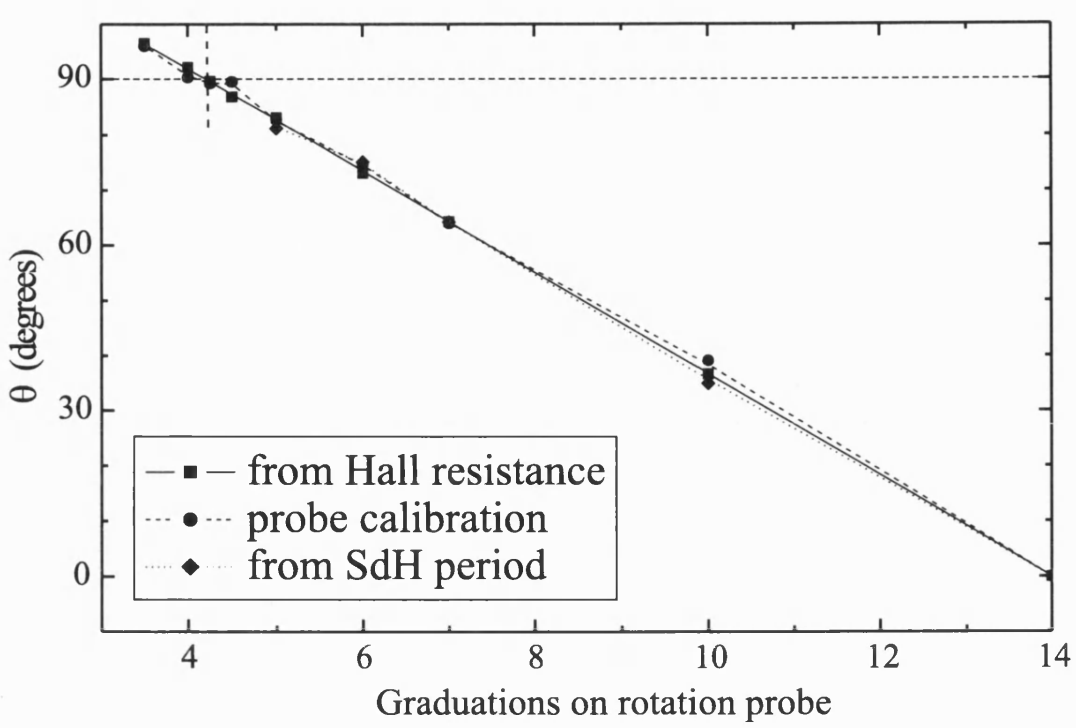

Figure 3.10: Calibration of the rotation probe.

1 (allowing for the offset) at high fields.

3.5.2 R_{xx} and R_{xy} vs B_z

Already, the results in figure 3.11 are disputing any claim that the peak position depends on the total external field, as would be expected if the peak occurred due to the magnetisation saturating. The results shown in figure 3.12 proceed to show that the peak position is actually dependent on the z-component of the applied field.

Panel a) of figure 3.12 again shows the R_{xx} traces at varying angles. However, they are now plotted against $B_z = B\cos(\theta)$. The degree to which the peaks are now aligned (peak positions vary between 0.145T and 0.153T) is remarkable considering the applied field varies over two orders of magnitude and the angle by over eighty degrees. This behaviour cannot be explained by a magnetisation model but instead corresponds to the behaviour expected from the snake and cycloid states being affected by the z-component of the external field.

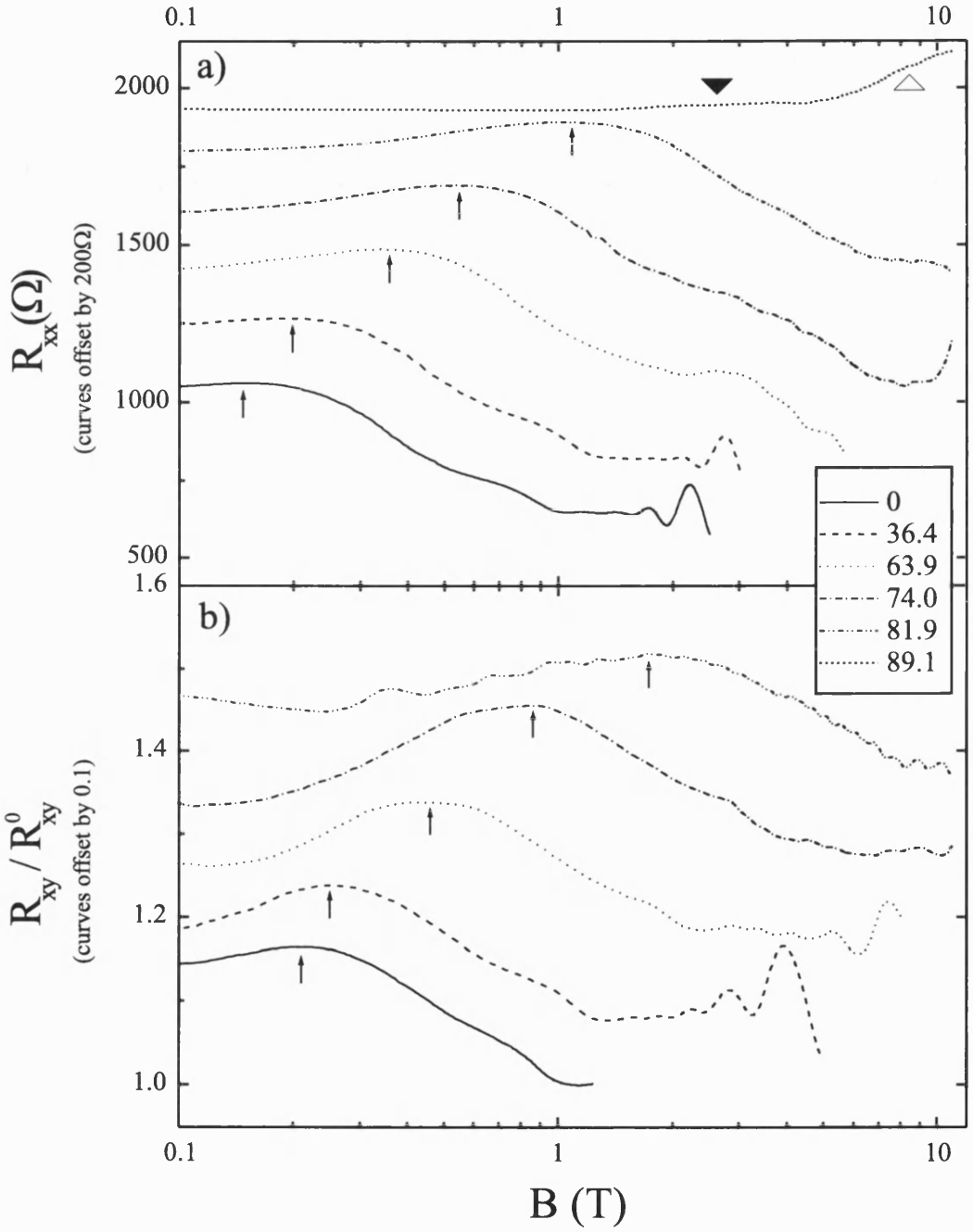

Figure 3.11: R_{xx} and $\frac{R_{xy}}{R^0_{xy}}$ plotted against B. (Log scale)

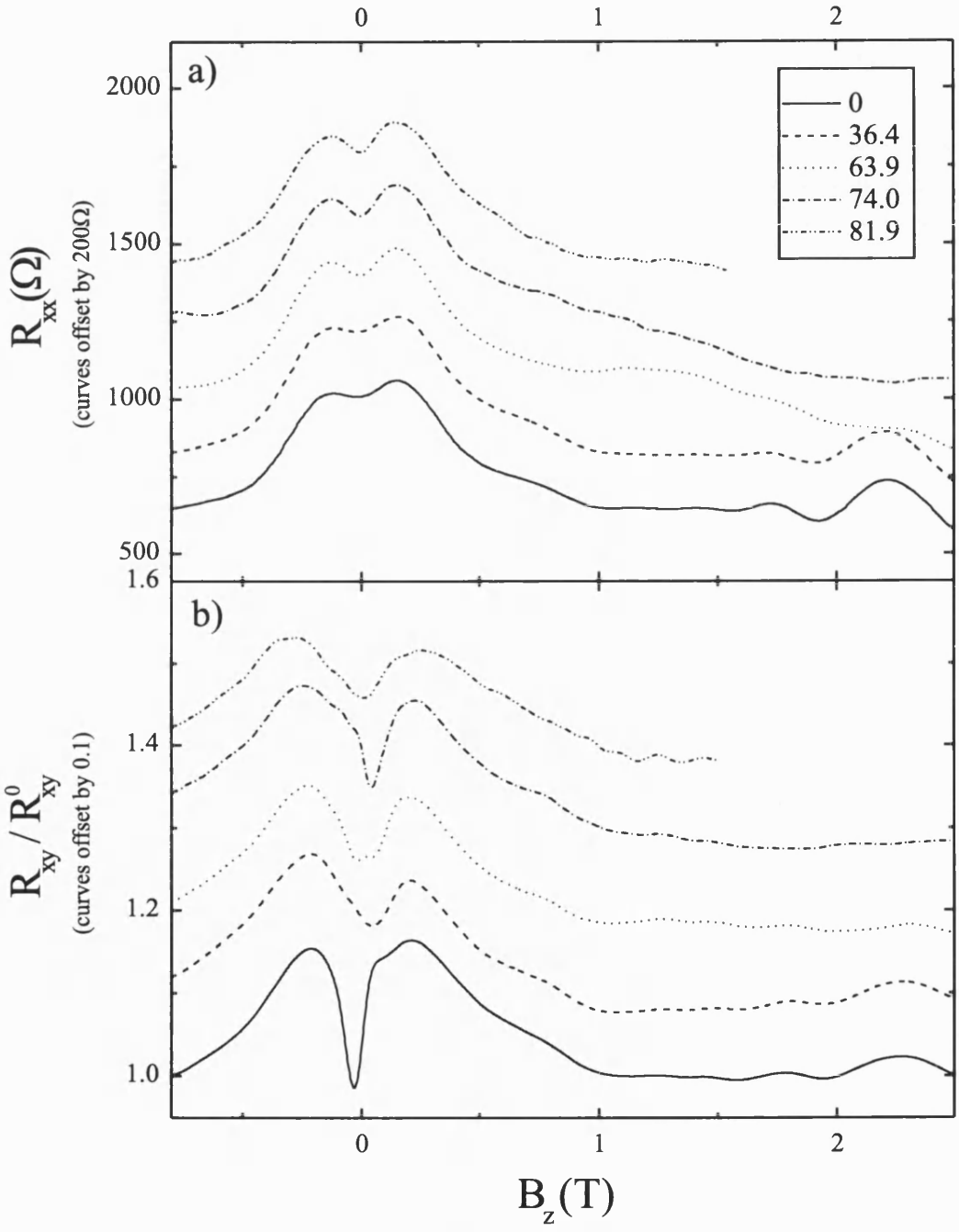

Figure 3.12: R_{xx} and $\frac{R_{xy}}{R^0_{xy}}$ plotted against B_z.

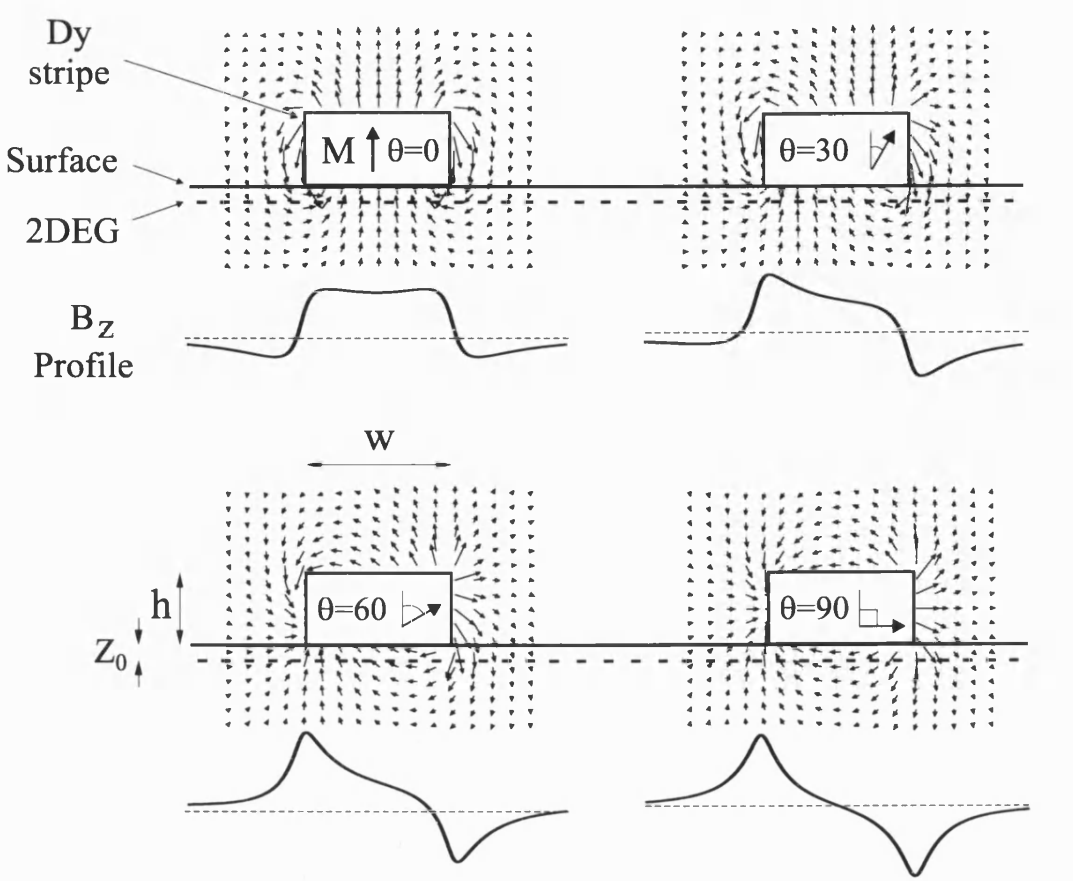

Figure 3.13: Effect of rotation on the magnetic profile. The stripe geometry is shown in relation to the sample surface (solid line) and 2DEG (dashed line) with the field lines for four angles of magnetisation. The profile seen by the electrons in the 2DEG is also shown for each angle.

In fact, the only noticeable effect of the rotation is in the behaviour of the SdH oscillations which are gradually quenched as the angle is increased. This is connected to the the changing magnetic profile from the stripe as it is magnetised in the direction of the external field (figure 3.13 shows the profile for various angles of magnetisation). At higher angles the profile becomes more triangular providing a greater disruption to the Landau levels. This in turn reduces the magnitude of the SdH oscillations.

Panel b) of figure 3.12 shows the normalised Hall resistance against B_z and presents a similar case to R_{xx}. The peaks line up at a field value of around 0.21T although there is more variation than in the R_{xx} results. The presence of peaks in R_{xy} was also observed in ref. [32] and presents a striking difference from the conventional Hall effect. The value of the transverse resistance is normally related to the average magnetic field in the junction being measured. Knowing

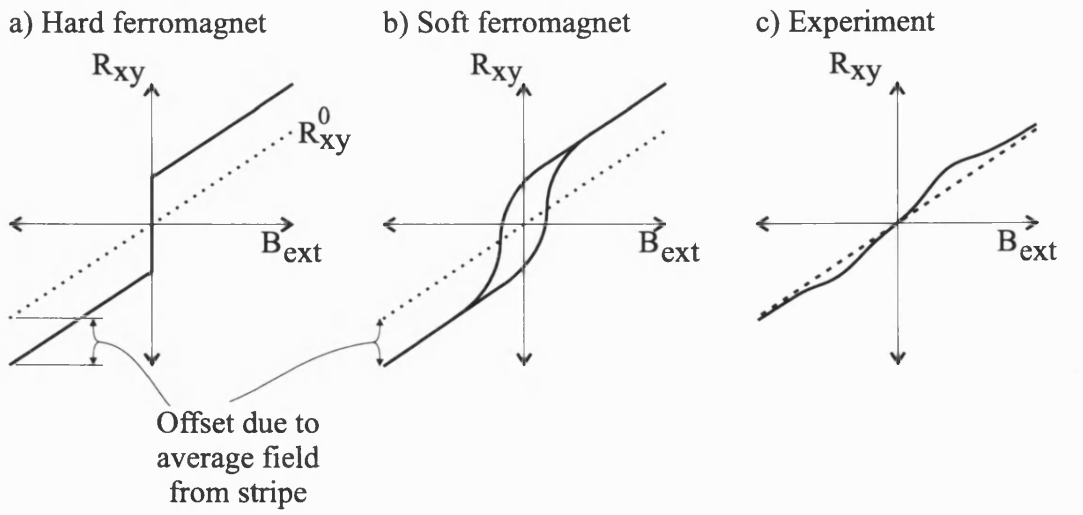

Figure 3.14: Effect of the stripe's magnetisation on the Hall effect. a) and b) show hard and soft magnetisation (with hysteresis) compared to c), the experimental result.

this, it is worth considering whether the stripe's magnetisation could explain the peak structure. The average value of B_z from the stripe's profile will produce an offset in the Hall resistance as shown in figure 3.14. If the stripe is a hard ferromagnet the transition will be abrupt as the field passes through zero, if soft, the transition will be smoother with evident hysteresis. However, in neither case will the Hall resistance then revert to the value of R^0_{xy} due to the external field alone which is precisely the behaviour observed in experiments.

The Hall effect also depends on the current flow in the device and this is a more promising area for possible explanations. Snake and cycloid states represent a obvious perturbation to the normal current flow which becomes less significant as the external field increases. The deviation in R_{xy} extends over the range $B_z \sim$ -1 to +1T indicating a limit to the effects of magnetic channelling in this device.

It is clear that in situations where the magnetic field varies across a sample, the Hall effect cannot necessarily be taken to be measuring the average magnetic field. The proximity of the magnetic stripe to the 2DEG creates strong disturbances in the electron transport which are reflected in the Hall resistance.

3.6 Dysprosium Magnetisation

A recurring theme through this thesis is that although the experiments were designed to explore snake state properties, the experiments actually contain a lot of information about the ferromagnetic stripes as well. This is particularly true of the dysprosium samples where complex behaviour is revealed in the rotation experiments and the temperature experiments of chapter 5.

3.6.1 In-plane Peaks

The results for high angles (magnetic field nearly in the plane of the 2DEG) were only briefly mentioned above, as several new effects are seen in addition to the peak structure. The peak itself is marked ($\triangle$) on the $\theta = 89.1°$ trace of figure 3.11a. It is seen against a rising background which fits a $R = R_0 \exp(\Delta B^2)$ trend characteristic of hopping transport [48] (Δ is a form factor depending on the geometry of the magnetic field with respect to the 2DEG). In the presence of a large in-plane field, the electron wavefunctions become localised on impurity sites in the δ-doped layer; transport becomes increasingly determined by electrons 'hopping' between such sites. The magnetic field reduces the overlap between wavefunctions exponentially reducing the hopping probability.

The other interesting feature is marked by a black triangle (▼). The structure is not clear on figure 3.11a so several 'grazing' angle (external field nearly in the plane of the device hence 'grazing' the 2DEG) traces are reproduced in figure 3.15 with R_{xx} plotted against B_z. Peaks are clearly visible either side of B_z=0 at 0.017 and 0.015T for the 89.2 and 90.7° traces respectively but they are not present for the 81.4 and 96.9° traces. There is also considerable hysteresis in the central two traces. The resistance changes smoothly around the peaks unlike the sharp jumps reported by Kubrak *et al.* [27] which were associated with changes of the magnetisation. The magnetisation of the stripe, and hence the peak behaviour, can be examined using the Stoner-Wohlfarth model of magnetisation reversal.

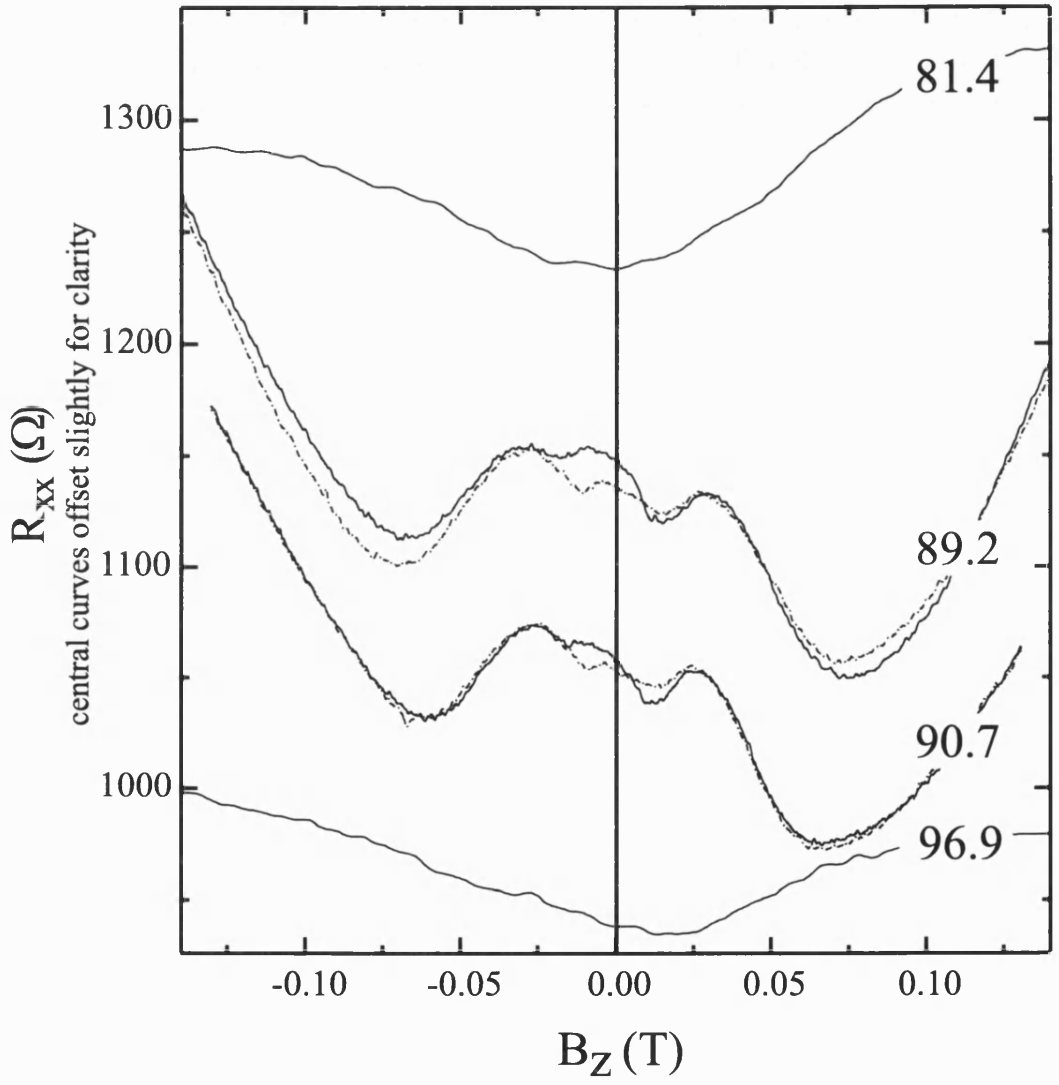

Figure 3.15: Additional peaks seen with the magnetic field 'grazing' the device.

3.6.2 Magnetisation Dynamics

There are two important factors to examine when considering the magnetisation of the stripe. Firstly, the magnetocrystalline anisotropy and secondly, the demagnetising field. The magnetocrystalline anisotropy arises from the interaction of the ions on the crystal surface and the electrons orbiting the dysprosium atoms. The aspherical 4f electron clouds are responsible for the magnetic properties of dysprosium and they react to the crystalline field by aligning the magnetisation in the basal plane (perpendicular to the c-axis). X-ray diffraction can be used to study the crystal structure of dysprosium on GaAs to check this.

Figure 3.16 shows the X-ray diffraction spectrum for a 125nm film of dysprosium evaporated onto a normal GaAs substrate [49]; below the spectrum is shown the spectral lines for powdered dysprosium. Note that in the reference lines, the b-axis is significantly shorter than the c-axis line, whereas this situation is reversed in the spectra from the film sample. From this it can be inferred that the film is polycrystalline with a preference for the c-axis to be in plane (hence low reflections) and growth occurs preferentially along the 'easy' b-axis normal to the surface. The shift in the position of the b-axis peak relative to the reference shows some straining of the dysprosium structure due to the GaAs surface. It should be borne in mind during the following analysis that the values and ideas are based on the properties of crystalline dysprosium which is only an approximation to the situation found here.

If the angle definition from the rotation probe is retained (see figure 3.9), the energy required to overcome the anisotropy and move the magnetisation away from the easy axis is:

$$E_A(\theta) = K_1 \sin^2\theta + K_2 \sin^4\theta + K_3 \sin^6\theta + ..., \tag{3.5}$$

where K_1, K_2 and K_3 are the anisotropy constants per unit volume and θ is the angle of the magnetisation from perpendicular. For dysprosium, $K_1 = 87 \times 10^6 \mathrm{Jm}^{-3} \gg K_2 = 6.4 \times 10^6 \mathrm{Jm}^{-3}$ so to a first approximation, only the first term need be considered.

The anisotropy minimises the energy on the atomic level, however, on a macro-

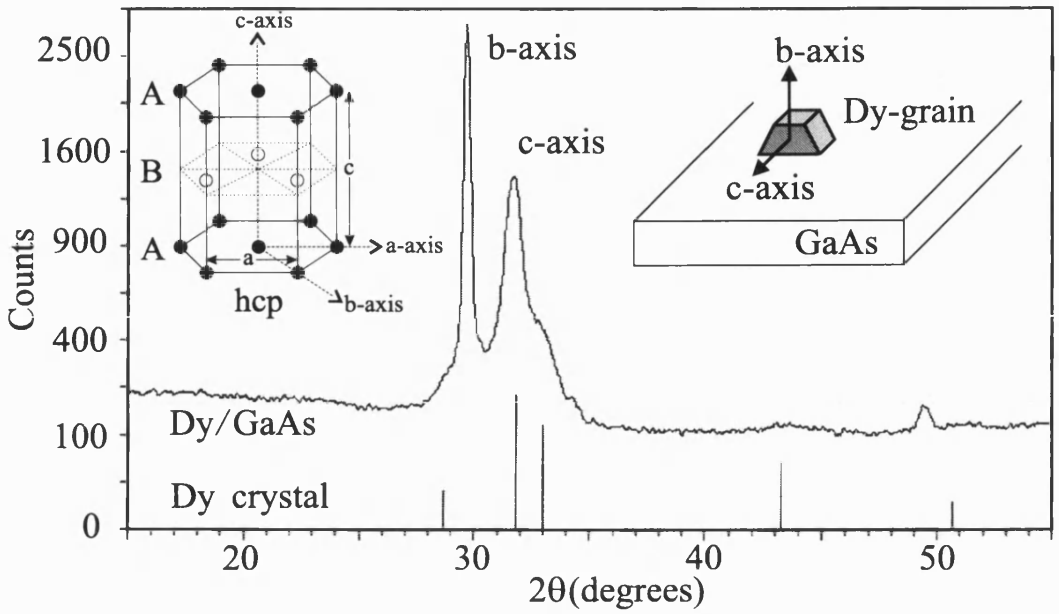

Figure 3.16: X-ray data from a film of dysprosium on GaAs (reference lines from a powdered sample are shown below). Inserts show the crystallographic structure of dysprosium and its orientation on GaAs.

scopic level, the stripe's magnetic dipole also has an energy

$$E_H = -\mu_0 M_s H \cos(\theta_H - \theta), \tag{3.6}$$

in the presence of a field, H, at an angle, θ_H, to the easy axis. There is also an energy cost associated with rotating the dipole:

$$E_D(\theta) = \frac{1}{2}\mu_0 M_s^2 \{(n_\parallel - n_\perp)\sin^2(\theta)\}, \tag{3.7}$$

where $n_\parallel$ and $n_\perp$ are the demagnetising factors for the stripe having the values 0.285 and 0.715 respectively (calculated following the formalism of Rhodes and Rowland [50]).

Combining eq.s 3.5, 3.6 and 3.7 for the total energy in the presence of an applied field at angle θ_H gives:

$$E(\theta) = -\mu_0 M_s H \cos(\theta_H - \theta) + K_1' \sin^2(\theta), \tag{3.8}$$

where

$$K_1' = K_1 hw + \frac{1}{2}\mu_0 M_s^2 (n_\parallel - n_\perp). \tag{3.9}$$

Evaluating both terms in eq. 3.9 shows that the magnetocrystalline anisotropy energy per unit length, $4.87 \times 10^{-6}\mathrm{Jm}^{-1}$, dominates over the dipolar energy, $-2.57 \times 10^{-6}\mathrm{Jm}^{-1}$. The consequence is that with no applied field, the lowest energy state is that in which the stripe is perpendicularly magnetised.

3.6.3 Stoner-Wohlfarth Model

The theory above is the basis of the Stoner-Wohlfarth model [51] where magnetisation rotation occurs by coherent reversal. The equilibrium solutions are deduced from the derivatives of eq. 3.8:

$$\frac{dE}{d\theta} = -\mu_0 M_s H \sin(\theta_H - \theta) + K_1' \sin(2\theta) = 0, \tag{3.10}$$

and

$$\frac{d^2E}{d\theta^2} = \mu_0 M_s H \cos(\theta_H - \theta) + 2K_1' \cos(2\theta) > 0. \tag{3.11}$$

Explained physically, the anisotropy presents an energy barrier for movement of the magnetisation away from the easy axis. The applied field must reach some critical field value before this energy barrier is overcome and the magnetisation can rotate. For the magnetisation to be in-plane, $\theta = 90°$ and $\theta_H = 90°$, requiring $H > 2K_1'/\mu_0 M_s$ from eq. 3.11. This field is 1.25T for dysprosium or $\mathrm{B}_z \simeq 0.016$ (for angles of 90.75 and 89.25°) in fair agreement to the observed peak positions around 0.027T in figure 3.15, especially considering there is some uncertainly in the angles and B_z is highly sensitive to small changes when the angle is near 90°.

However, peaks are not observed in the 97.0 and 81.4° traces. This can be explained by considering the smoothness of the rotation. The orientation of the magnetisation corresponding to the minimum energy state can be derived by rearranging eq. 3.10 as:

$$H = \frac{K_1'}{\mu_0 M_s} \frac{\sin(2\theta)}{\sin(\theta_H - \theta)}. \tag{3.12}$$

Figure 3.17 shows the rotation for different angles where the discontinuity at 90° is rapidly smoothed for fields slightly off 90° as verified experimentally in

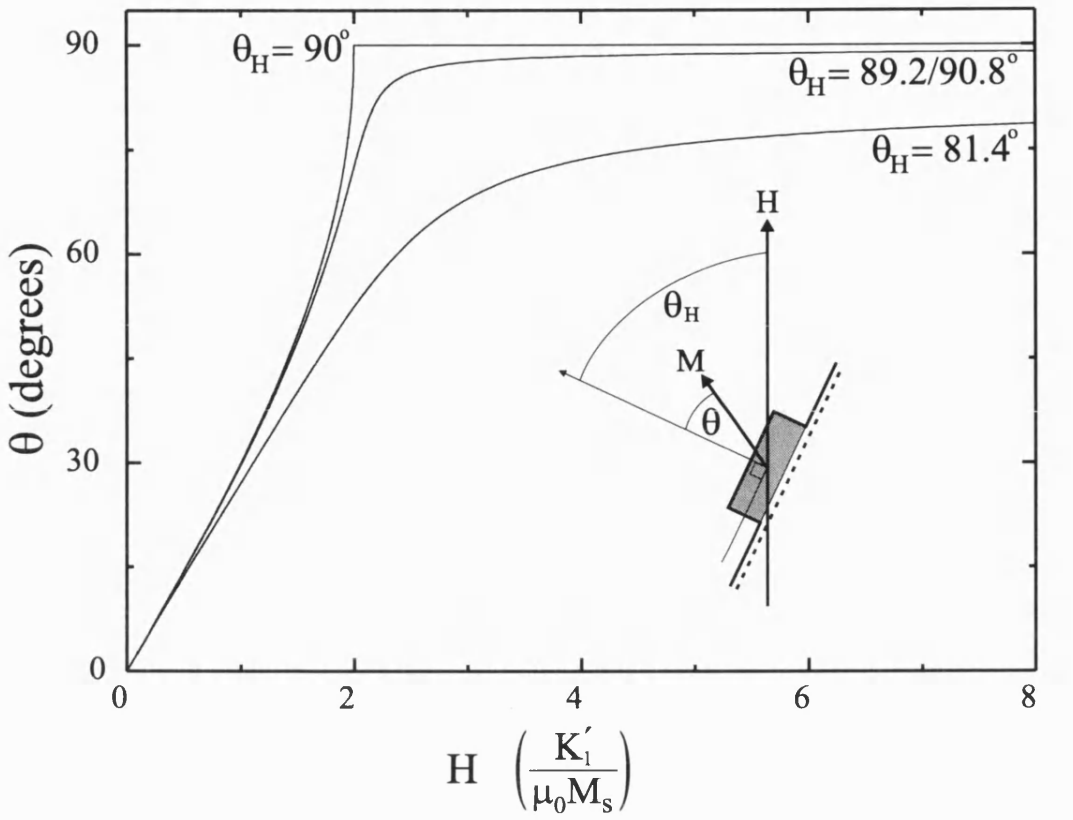

Figure 3.17: Results from the Stoner-Wohlfarth model showing the rotation of the magnetisation for various applied field angles.

figure 3.15.

3.7 Conclusions

The origin of the observed peaks in the magnetoresistance has been examined. The dependence of the R_{xx} peaks on the z-component of the applied field favours an interpretation based on channelling via snake and cycloid states. Possible effects due to the polycrystalline nature of the dysprosium cannot be discounted but neither is there evidence for them. The size effect argument is countered by the lack of peaks in the absence of a stripe and no evidence is found for features forming at a constant value of B apart from those observed when the field is almost in the plane of the device. In this case, the sharp rotation of the magnetisation, overcoming the strong anisotropy, can be observed in the magnetoresistance.

The Hall resistance is observed to be non-linear from -1 to +1T with peaks forming at fairly constant values of B_z in a striking departure from normal Hall effect measurements. This has implications for sensors used in close proximity to magnetic elements.

Chapter 4

Influence of Device Parameters on Peak Position

4.1 Introduction

This chapter is concerned with how the device properties and experimental conditions can be altered to manipulate the peak behaviour. Drift-diffusion and velocity correlation methods for modelling magnetic channelling are introduced and used to examine the magnetoresistance changes when the contact separation is varied, different stripe materials are used and the gate voltage is changed.

4.2 Modelling Diffusion

The two models used in this thesis take alternative approaches to calculating the diffusion of electrons through the device but both are derived from the same basic theory. Resistivity can be expressed in terms of components of the diffusion tensor via the Einstein relation; $\boldsymbol{\rho} = (h/4\pi m^* e^2)\mathbf{D}^{-1}$. The relationships of interest to this report are then:

$$\rho_{xx} = \frac{1}{Ne^2} \frac{D_{yy}}{D_{xx}D_{yy} - D_{xy}D_{yx}}, \tag{4.1}$$

where N is the two dimensional density of states $= 4\pi m^*/h^2$, and:

$$\rho_{xy} = -\rho_{xx} \frac{D_{xy}}{D_{yy}}. \tag{4.2}$$

The individual diffusion components can be calculated from the 'velocity-velocity correlation function' which measures the correlation between electron velocity in direction μ at time t=0 and electron velocity in direction υ a time, t, later:

$$\mathbf{D}_{\upsilon\mu} = \int_0^\infty < \nu_\upsilon(t)\nu_\mu(0) > e^{\frac{-t}{\tau}} dt, \tag{4.3}$$

where τ is the typical relaxation time of the system.

In the presence of a uniform magnetic field ρ_{xx} and ρ_{xy} can be derived and have a simple solution. The x-component of the velocity of an electron in an unmodulated 2DEG in a uniform magnetic field is:

$$\upsilon_x = \upsilon_F \cos(\omega_c t + \phi), \tag{4.4}$$

which allows D_{xx} to be written as:

$$D_{xx} = \int_0^\infty \upsilon_F^2 < \cos(\omega_c t + \phi)\cos\phi > e^{\frac{-t}{\tau}} dt. \tag{4.5}$$

The integral is over a periodic function with period $T_0 = 2\pi/\omega_c$ and so can be rewritten as:

$$D_{xx} = \upsilon_F^2 \int_0^{T_0} dt \frac{< \cos(\omega_c t + \phi)\cos\phi > e^{\frac{-t}{\tau}}}{1 - e^{\frac{-t}{\tau}}}. \tag{4.6}$$

The homogenous field allows the average to be replaced with an integral over ϕ and the t dependence can be dealt with by integrating by parts to give:

$$D_{xx} = \frac{v_F^2 \tau}{1 + (\omega_c \tau)^2} \frac{1}{2\pi} \int_0^{2\pi} d\phi \{\cos\phi - (\omega_c \tau) \sin\phi\} \cos\phi. \tag{4.7}$$

The sin cos term of the integral gives zero on integrating and the $\cos^2$ integrates to leave the exact solution:

$$D_{xx} = \frac{1}{2} v_F^2 \tau \frac{1}{1 + (\omega_c \tau)^2}. \tag{4.8}$$

The same process can be used to calculate the other components of $\mathbf{D}$ giving:

$$\begin{aligned} D_{xx} = \quad D_{yy} \quad &= D_0 \\ D_{xy} = -D_{yx} \quad &= -\omega_c \tau D_0 \\ D_0 \quad &= \frac{1}{2} v_F^2 \tau \frac{1}{1 + (\omega_c \tau)^2}. \end{aligned} \tag{4.9}$$

Substituting the relevant components into eq. 4.1 leads to the simple result:

$$\rho_{xx} = \frac{1}{Ne^2} \frac{2}{v_F^2 \tau}, \tag{4.10}$$

which has no dependence on B and is an equivalent expression to the Drude resistivity, eq. 3.4.

4.3 Drift Diffusion Model

In ref. [32], a simple model was presented to account for the effects of snake and cycloid states. Following the technique used by Beenakker [19] and Ger-

hardts [52], a correction to the diffusion coefficients was calculated by integrating the velocity of the snake and cycloid states over the Fermi surface, with limits provided by the geometry of the sample. As the resistivity can be calculated from the diffusion coefficients, a comparison with experiment can then be made.

4.3.1 Theory

The magnetic profile from the stripe creates a gradient of magnetic field in the y direction (across the channel) which causes electrons to drift along x (along the channel). The drift velocity averaged over one period can be calculated by considering the different electron trajectories. A drift velocity in x will enhance the diffusion coefficient by a factor $\delta D_{xx} = \langle v_d^2 \rangle \tau$ where τ is the scattering time and v_d is the drift velocity. This makes $D_{xx} = D_0 + \langle v_d^2 \rangle \tau$. The resistivity components of interest, ρ_{xx} and ρ_{xy}, are then modified to:

$$\frac{\rho_{xx}}{\rho_0} = 1 - \frac{2\langle v_d^2 \rangle / v_F^2}{1 + 2\langle v_d^2 \rangle / v_F^2}, \tag{4.11}$$

and

$$\rho_{xy} = \frac{B_a}{e n_s} \frac{\rho_{xx}}{\rho_0}, \tag{4.12}$$

where v_F is the Fermi velocity and ρ_0 is the zero field (Drude) resistivity as given in 3.4.

The drift velocity due to the snake states is $v_d = v_F(\sin\phi)/\phi$ where ϕ is the angle of the electron heading away from the stripe edge (see figure 4.3). The velocity can be integrated over the Fermi surface to obtain the average drift velocity. The integral is performed between 0 and ϕ_{max}:

$$\langle v_d^2 \rangle = \frac{v_F^2}{\pi} \int_0^{\phi_{max}} \left(\frac{\sin\phi}{\phi} \right)^2 d\phi, \tag{4.13}$$

where ϕ_{max} is dependent upon the sample geometry as now explained.

To keep the physics analytical, it is necessary to replace the calculated profile with an approximation, shown in figure 4.1. The profile is reduced to a square barrier of

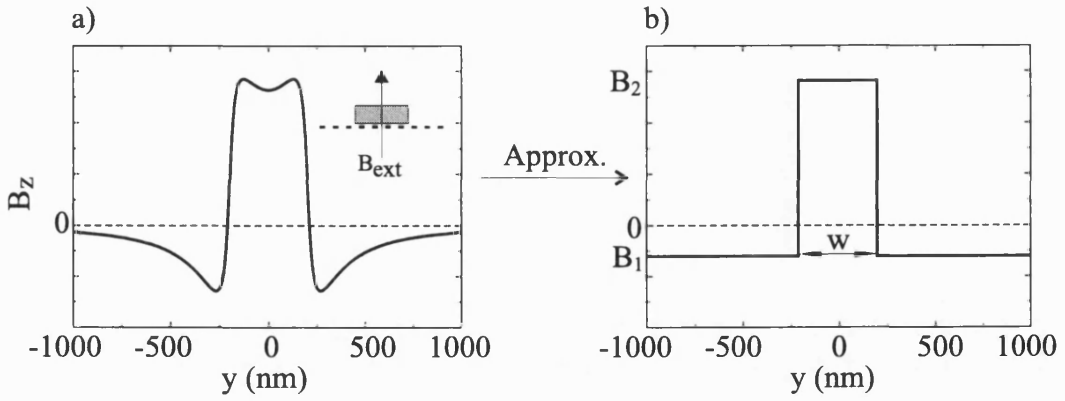

Figure 4.1: a) the real profile from a stripe and b) the approximation used in the drift-diffusion model.

field B_2 under the strip and B_1 elsewhere. One consequence of this approximation is a definite boundary between snake and cycloid states, the former can only exist as long as the applied field, B_a, is less than $|B_1|$ and the latter only if $B_a > B_1$.

Figure 4.2 shows the labelling and dimensions of the stripe and channel that will be used in the following discussion.

The averaging of eq. 4.13 takes place over the Fermi surface. If the channel was infinitely wide, then any electron starting at the boundary between B_1 and B_2 and heading away from the stripe would eventually return to the boundary. The same would be true under the stripe if it were also infinite. However, the sample is not infinite and so snake and cycloid states can only propagate if their orbits fit within the channel and stripe. This introduces the idea of a maximum angle with which, e.g. an electron can head away from the stripe and return without hitting the channel wall. The geometrical considerations for snake states are shown in figure 4.3 where the orbit is separated into trajectories away from the stripe and trajectories under the stripe.

The limiting angle for electrons heading away from the stripe can be calculated by considering the equations for electron motion in a homogenous field (see section 1.3.2). The equations for the time evolution of the position and velocity are reproduced here for convenience.

$$v_y = -v_F \sin(\omega_{c1} t + \phi_1), \tag{4.14}$$

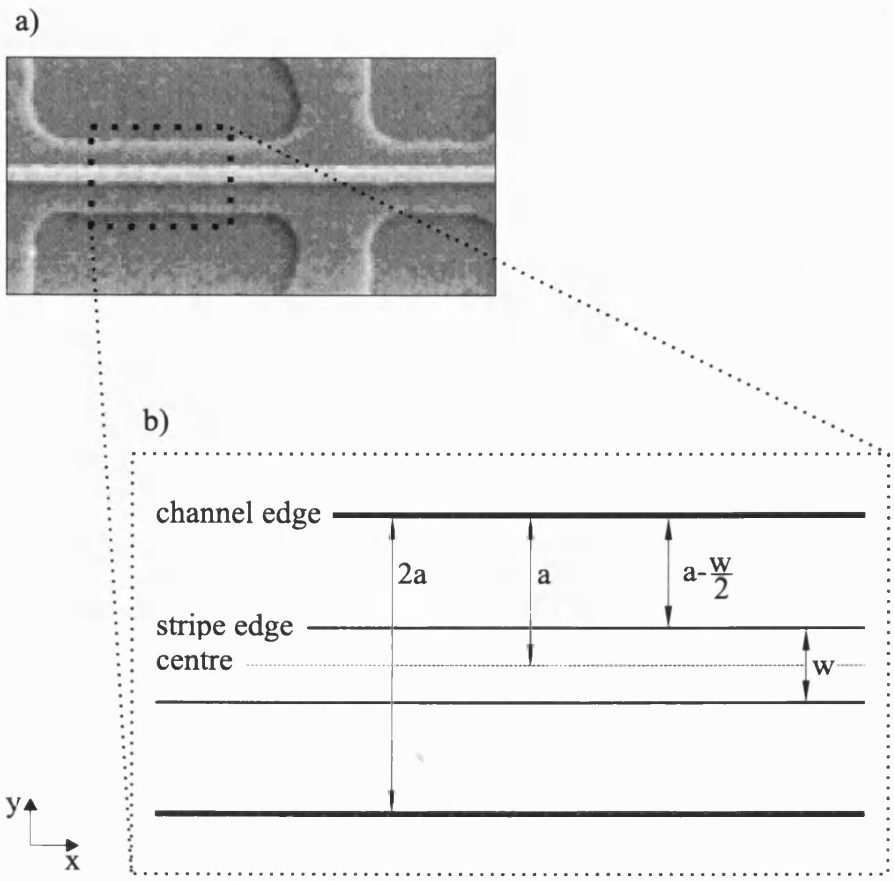

Figure 4.2: Channel dimensions used for modelling.

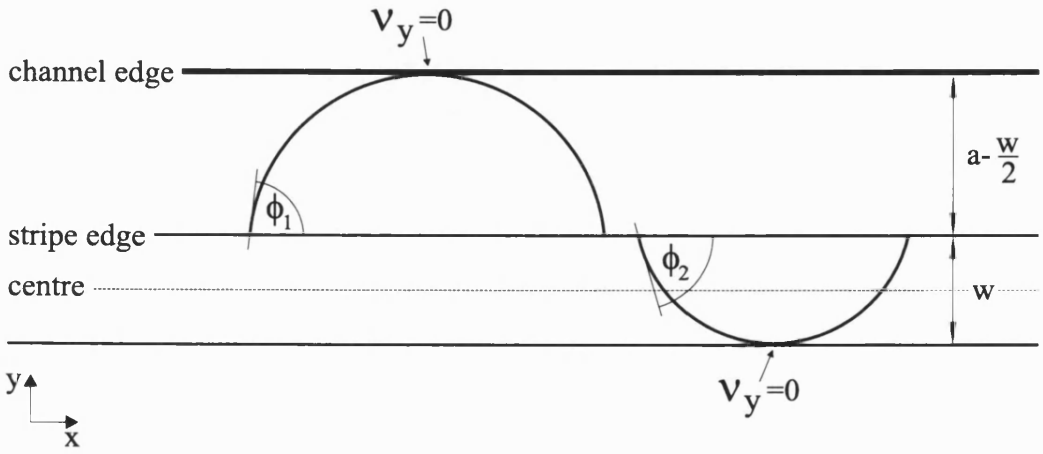

Figure 4.3: Geometry for snake state calculation.

$$y = r_{c1}\cos(\omega_{c1}t + \phi_1). \tag{4.15}$$

At t=0, eq. 4.15 gives $y = r_{c1}\cos(\phi_1)$. The most extreme point of the orbit will occur when $v_y = 0$ requiring $\omega_{c1}t + \phi_1 = n\pi$ and therefore at the most extreme point $y = r_{c1}$. The difference between these two points must be smaller or equal to the space between the stripe edge and channel edge, $a - \frac{w}{2}$, leading to the condition:

$$\begin{aligned} r_{c1} - r_{c1}\cos(\phi_1) &\leqslant a - \frac{w}{2} \\ \text{or} & \\ \cos(\phi_1) &\leqslant 1 - \left(\frac{a - \frac{w}{2}}{r_{c1}}\right). \end{aligned}$$

Re-arranging for ϕ_1 gives:

$$\phi_1 = \begin{cases} \cos^{-1}[1 - (a - w/2)/r_{c1}] & \text{if } 2r_{c1} > a - w/2, \\ \pi & \text{otherwise,} \end{cases} \tag{4.16}$$

the second case represents the limit where an entire cyclotron orbit fits into the space between stripe and channel edge so the condition is satisfied for any starting angle.

The same argument leads to the restrictions on ϕ_2 by simply replacing the stripe edge - channel edge separation with the stripe width, w.

$$\phi_2 = \begin{cases} \cos^{-1}(1 - w/r_{c2}) & \text{if } 2r_{c2} > w, \\ \pi & \text{otherwise.} \end{cases} \tag{4.17}$$

The snake state must satisfy the conditions for both ϕ_1 and ϕ_2 hence the upper limit for the integral in eq. 4.13 is the smaller of the two or $\phi_{max} = min(\phi_1, \phi_2)$.

The situation for cycloid states is more complicated but along the same lines.

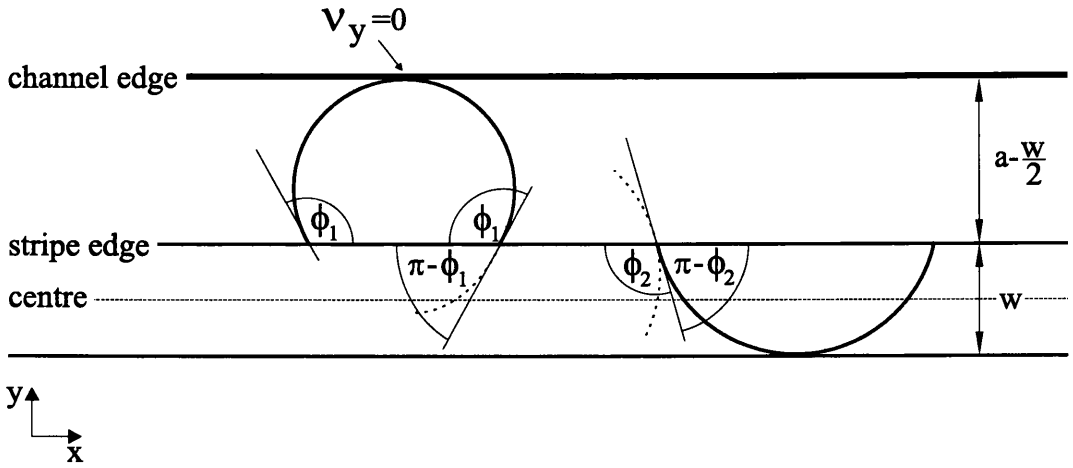

Figure 4.4: Geometry for cycloid state calculation. Note the angle ϕ_2 has been reversed to allow the same calculation as for snake states even though the field sign doesn't change across the sample.

There are two significant differences both arising from the magnetic field having the same sign throughout the device. Firstly, the angles need to be slightly redefined to remain compatible with the snake state calculation. As shown in figure 4.4, an electron starting with angle ϕ_1 returns to the boundary and should then proceed along the dotted path. However, note that the angle would then be $\pi - \phi_1$. Instead, the trajectory can be flipped about the vertical and considered it as if it were a normal snake state, but with angle $\pi - \phi_2$ under the stripe.

It follows that the expression for $\langle v_d^2 \rangle$ now becomes:

$$\langle v_d^2 \rangle = \frac{v_F^2}{\pi} \int_{\phi_2'}^{\phi_1} \left(\frac{B_2 - B_1}{\pi B_1 + \phi(B_2 - B_1)} \sin\phi \right)^2 d\phi, \tag{4.18}$$

where $\phi_2' = \pi - \phi_2$.

The limits on the integration are different because of the need to define the angle under the stripe as $\pi - \phi_2$.

4.3.2 Implementation

As the model is analytical, finding solutions is simply a case of setting up the initial conditions (magnetic profile, device dimensions and properties such as

n_s), stepping through values of B_a, working out the angles for each case and integrating to get the final result. The numerical integration was performed using Mathcad [53].

4.3.3 Limitations

This model is solely concerned with the effect of the snake and cycloid states on the diffusion coefficients. It does not attempt to model any other transport phenomenon such as boundary scattering or temperature effects and treats the situation classically. To retain an exact solution, it uses an approximate modulation profile resulting in an artificial separation into snake and cycloid regimes.

To examine the importance of the profile approximation, a C program was written which performed the snake state integration only but used the actual profile and iterated the electron motion to determine ϕ_{max}. The results for the two approaches are shown in figure 4.5. The exact magnetic field profile allows snake states to exist to higher values of the external magnetic field as the exact profile has a greater amplitude (see figure 4.1). The results for the iron stripe are fairly similar but dysprosium's larger modulation produces a greater discrepancy. However, this is only a comparison of snake states and it is clear that cycloid states would start forming in different regions of the sample at lower field. The combined effect, therefore, might lead to a similar overall look between the approximate and exact profiles. Unfortunately, the iterated motion and exact profile are not compatible with the calculation for cycloid states so the comparison cannot be extended.

4.4 Velocity Correlation

A second approach to modelling these devices has been developed by directly considering the velocity correlation function, eq. 4.3. By iterating the electron motion from multiple initial conditions in the presence of a magnetic field and recording the changing velocities, the average correlation (taken over all initial positions and angles) can be calculated. By moving to an iterated process, individual trajectories are considered, weighted by the scattering probability and the

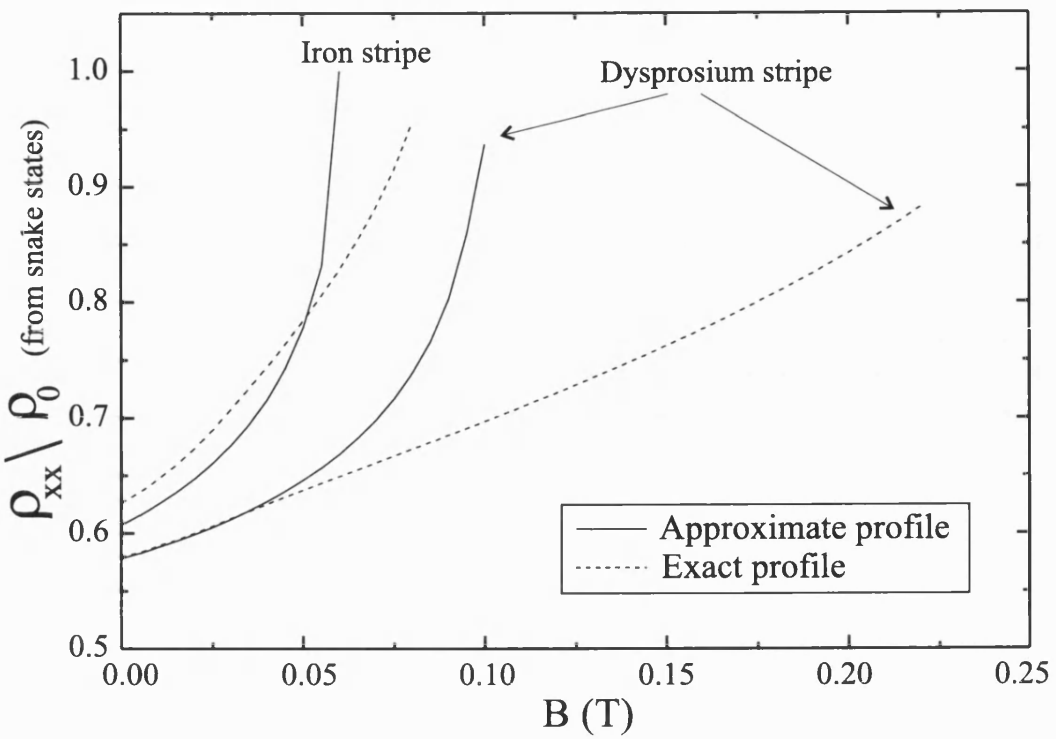

Figure 4.5: Comparison of the effect of snake states on ρ_{xx} calculated with approximate and exact magnetic profiles.

actual potential can be included as well as effects such as boundary scattering.

The uniform field case, derived in section 4.2 above, provides a good test for the model. Figure 4.6 shows the result from the velocity correlation simulation for three simple examples, $v_F = 200,000$ ms^{-1} and $\tau = 20$ ps ($\triangle$), $v_F = 200,000$ ms^{-1} and $\tau = 10$ ps ($+$) and $v_F = 100,000$ ms^{-1} and $\tau = 10$ ps ($\times$). The three straight lines agree with the theoretical values ($1/Ne^2 \times 2/v_F^2\tau$) of 2.5, 5 and 20. The inset shows ρ_{xy} which was given earlier (eq. 4.2) as being ρ_{xx} multiplied by D_{xy}/D_{yy}. Checking eq. 4.9 gives:

$$\rho_{xy} = \rho_{xx}\omega_c\tau. \tag{4.19}$$

By inspection, the gradient of the curves should be proportional to $\rho_{xx}\tau$ explaining why the two lower ρ_{xx} traces overlap in ρ_{xy} and why the upper trace has four times the gradient of the other two.

These initial results show the simulation can successfully reproduce the theoret-

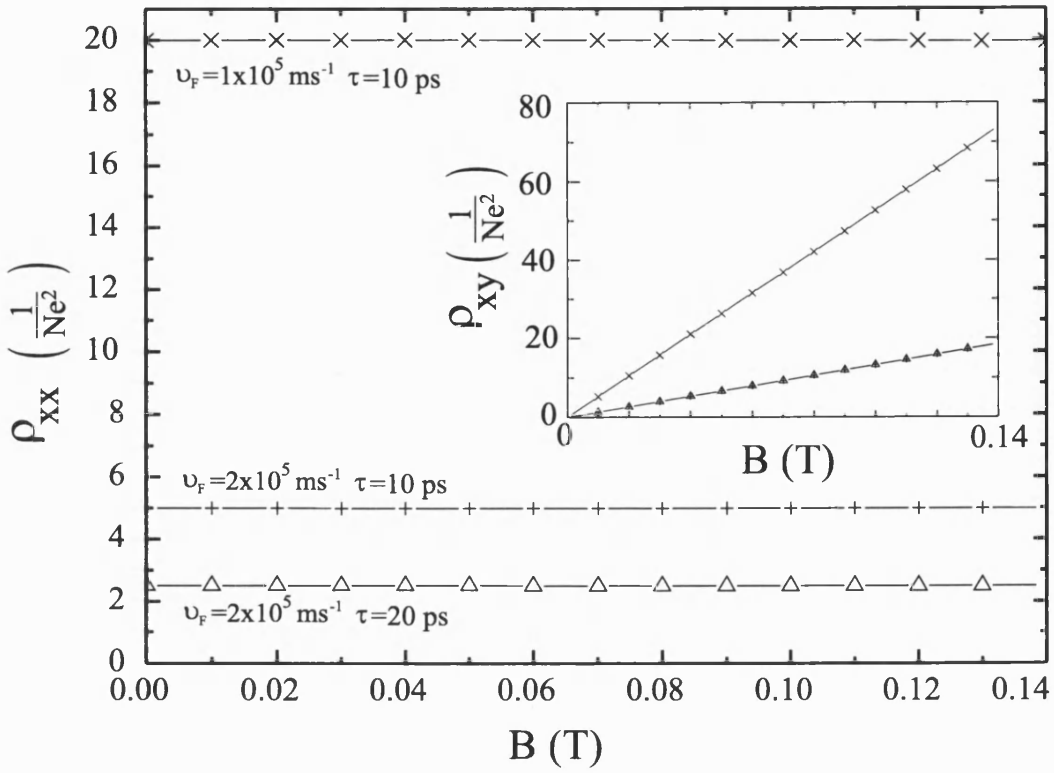

Figure 4.6: ρ_{xx} and (inset) ρ_{xy} results for the velocity correlation simulation.

ical values to a high accuracy over a range of parameters.

4.4.1 Implementation

Simulating the motion of a large number of electrons in a magnetic field requires significant processing time. The program was written in C to take advantage of some of the standard Runge-Kutta routines for iteration [54]. The program outline is shown in figure 4.7.

4.4.2 Limitations

The biggest drawback of this approach is the amount of time required to obtain a solution. The drift diffusion model calculates an answer in seconds whereas this simulation can take days depending on the number of initial conditions considered and the accuracy of the iteration/integration. Including the effects of diffuse

Equation to simulate

$$\mathbf{D}_{\upsilon\mu} = \int_0^{\infty} dt \quad < \nu_{\upsilon}(t)\nu_{\mu}(0) > \quad e^{\frac{-t}{\tau}}$$

Integral performed by simple trapezoidal rule at each timestep. Upper limit replaced by multiple of τ.

Key calculation

Multiplying factor

Method

Loop magnetic field
- Loop starting position
  - Loop starting angle
    - Calculate electron trajectory
      - Store initial velocity
        - Calculate changes in position and velocity in time δt
        - Multiply initial velocities by new velocities
        - Add weighted answer to diffusion coefficients
        - Advance time and repeat

Calculate resistivity from final diffusion coefficients

Figure 4.7: Outline of the velocity correlation program.

Ferromagnet	Saturation Magnetisation M_s (T)	Curie Temperature T_c (K)
Dysprosium	2.92	88
Iron	1.74	1043
Nickel	0.51	627

Table 4.1: Saturation magnetisation and Curie temperature of selected ferromagnets [41]. (It has come to the attention of the author that the values of M_s given here are all too small by a factor of $4\pi/10$. This is a problem with the source used.)

boundary scattering make this slower still as the sample size has to be increased to average the randomness of the process.

4.5 Results of Experiments and Modelling

The preceding sections have looked at the techniques which can be used to model the device behaviour. It is now time to examine the experimental evidence and attempt to explain it.

4.5.1 Ferromagnetic Stripe and Magnetic Profiles

Three different ferromagnets have been used as stripe materials (the values shown in table 4.1 are used for the following analysis. The values of M_s are all too small but their magnitudes with respect to each other are correct and so do not fundamentally alter the validity of the analysis). Results for iron and nickel were shown in ref. [32]. New samples with a higher carrier density and narrower stripes of iron and dysprosium were fabricated for comparison. Figure 4.8a shows the experimental results for devices with stripes of nickel, iron (Fe I as used in ref. [32] and Fe II newly fabricated) and dysprosium. The resistance has been normalised to the zero-field value to make comparisons easier.

In each curve, the resistance rises smoothly, gently peaks and then falls. However, the peak separation changes from 26mT for nickel to 58 and 66mT for iron and 105mT for dysprosium. These values correlate with the increasing saturation

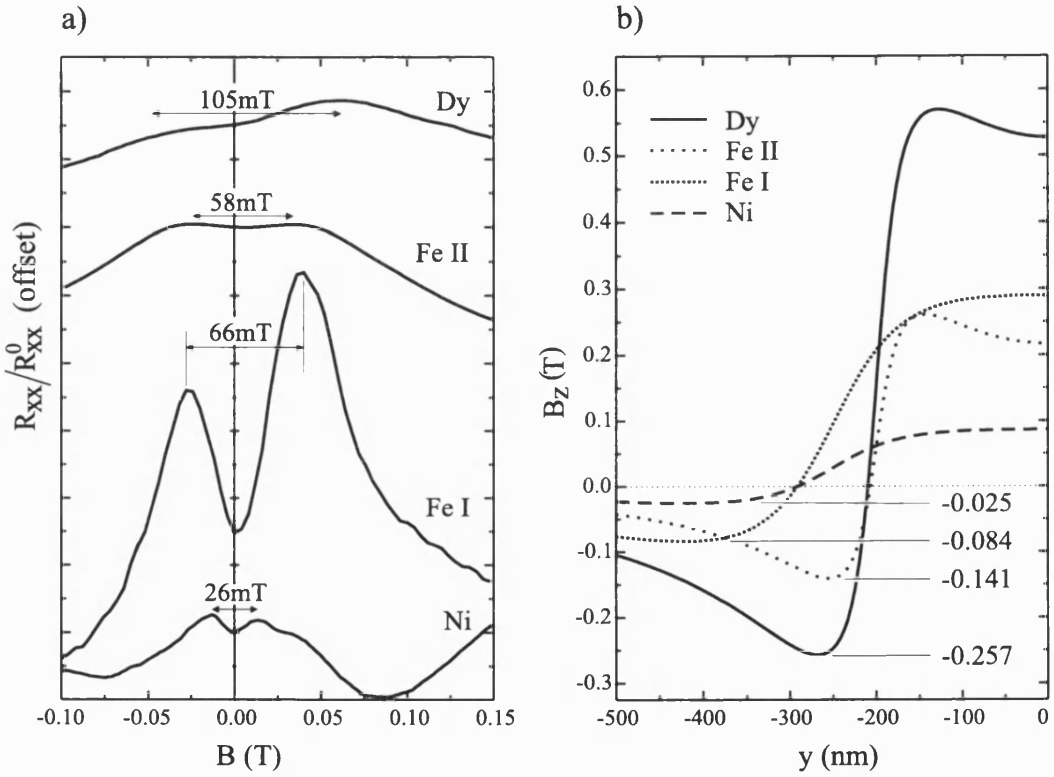

Figure 4.8: a) Comparison of the resistance peaks for nickel, iron and dysprosium samples. b) Magnetic profile for each stripe with the minimum field value, B_m, indicated.

magnetisation of the materials.

A more detailed comparison can be made by comparing the average peak position to the minima of the field profile for each stripe (the calculated profiles for each stripe are shown in figure 4.8b). As the devices were manufactured in different runs, the stripe dimensions and 2DEG parameters are not uniform between the devices. In particular, the Ni and Fe I samples had 500nm wide, 200nm high stripes over a 2DEG 90nm below the surface. The Fe II and Dy samples had stripes which were 400nm wide, 90 and 140nm high respectively and the 2DEG was only 24nm below the surface. The values for the ratio between the magnetic field at which the peak forms, B_p, and the minima of the profile, B_m, fall in the range 0.2 to 0.52 whilst the saturation magnetisation varies by almost a factor of six. This confirms the link between the strength of the stripe's field and the peak position at the same time as prompting questions about the exact relationship. It is interesting to note that the ratio B_p/B_m is highest for nickel (0.52) and that nickel's profile is the most step-like. Next highest is Fe I with a ratio of 0.39 and again, a profile which is more like a step function. Fe II and Dy both have more varying profiles (due mainly to the reduced stripe width) and have similar ratios around 0.2. It seems likely that the electrons are affected by some average magnetic field which would agree with the results for the rotation in chapter 3 where the electrons seem unaffected by the changing magnetic profile.

In addition, it is not surprising that the ratio is not unity, as it has already been stated that snake and cycloid states are not mutually exclusive (see figure 4.9) which would agree with the peak occurring before B_m.

Modelling Results - Drift Diffusion Model

Figure 4.10 shows the results from the drift diffusion model considering the different ferromagnets shown in figure 4.8. The snake states are cancelled out when the applied field equals the average field away from the stripe, B_1, making the resistivity rise to unity at 16mT (Ni), 60mT (FeI), 45mT (FeII) and 99mT (Dy). It can be seen that the peak position correlates with the experimental data, i.e. Ni has the smallest peak position followed by Fe II, Fe I and Dy in agreement with figure 4.8. This is a success for the model as simply comparing the maximum negative field value would put Fe I before Fe II.

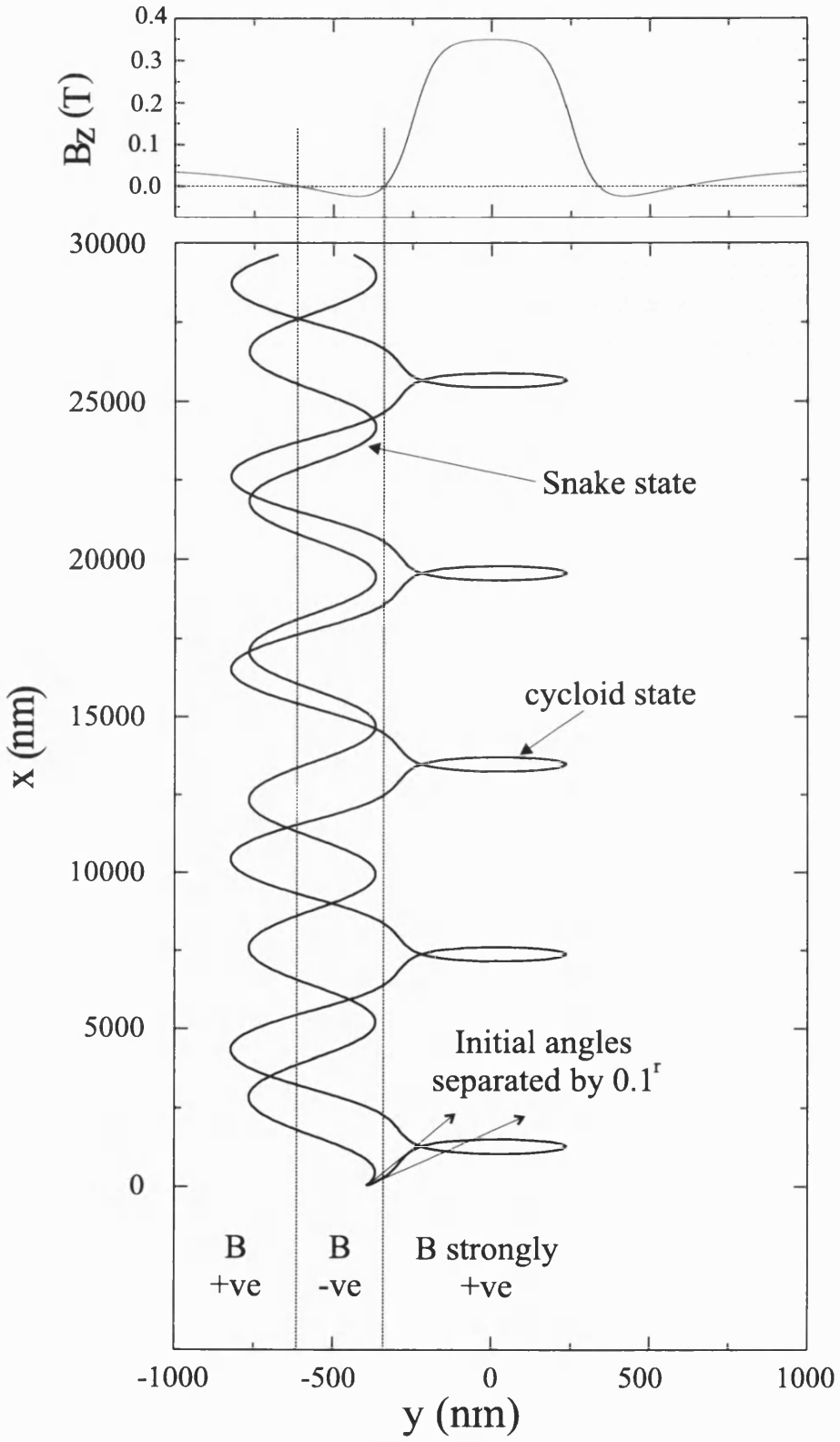

Figure 4.9: Coexistence of snake and cycloid states in an iron sample with an external field of 0.06T.

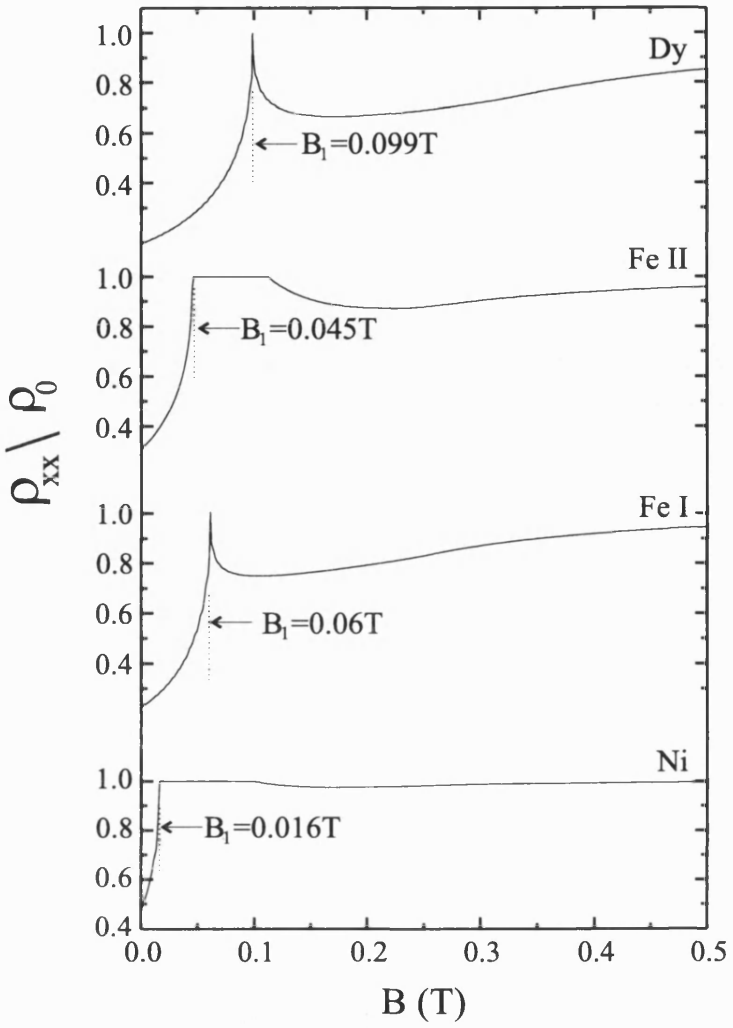

Figure 4.10: Results from the drift diffusion model after averaging the magnetic barrier.

The flattened region for the Ni and Fe II samples reveals a drawback with using the average profile. When the applied field is close to the average negative field, B_1, the cycloid states are controlled by the region under the stripe. Cycloid states only exist if the stripe is wider than the cyclotron diameter set by the difference between B_1 and B_2. The nickel device has values B_1 = -0.0157T and B_2 = 0.0656T so when the applied field cancels B_1 the field under the stripe will be 0.0813. This is significantly less than the ~0.28T required for a sample with a Fermi velocity of 1.9×10^5 ms^{-1} and stripe width of 500nm. The Fe II sample encounters the same issue whereas the Fe I and Dy samples have a large enough modulation for cycloid states to form immediately.

The model performs less well when examining the predicted magnitude of the

effects. Dysprosium has the largest dip at zero-field and the deepest valley after the peak whereas experimentally FeI shows the largest effects.

The results suggest that the peak position correlates well to the average field away from the stripe. Performing a similar ratio calculation as before, average experimental peak position / average negative field, gives higher values 0.81, 0.55 0.64 and 0.53 for Ni, Fe I, Fe II and Dy respectively with significantly less variation than the previous calculation, 0.67 ± 0.14 versus 0.36 ± 0.16 although it should be noted that the variation in average negative field values is less than the variation in the minimum field.

Modelling Results - Velocity Correlation

Figure 4.11 shows the results of including diffusive boundaries into the model. They are included to better match the experimental results which show signs of having ~40% diffuse boundaries [49, 7]. This introduces a number of problems, the biggest being the need to average the data or use significantly more trajectories in the model to smooth the randomness which diffuse boundaries introduce. The second problem is identifying small peaks from the background. Looking at the nickel result, the peak forms at 0.026T but there is also a small discontinuity at $\sim$ 0.012T which would bear more resemblance to the experimental result.

Looking at the results generally, the velocity correlation model correctly shows that the Fe I sample gives the largest resistance dip at zero-field and gives the correct order of peaks from Ni to Fe II to Fe I. However, comparisons with the experimental peak positions show the nickel peak at almost twice the field value and a lot larger than in reality.

Generally, the results from the drift diffusion model are more sensitive to the details of the magnetic profile and the peak positions correlate well to the experiments, whereas the velocity correlation results are not as precise but predict the overall behaviour better.

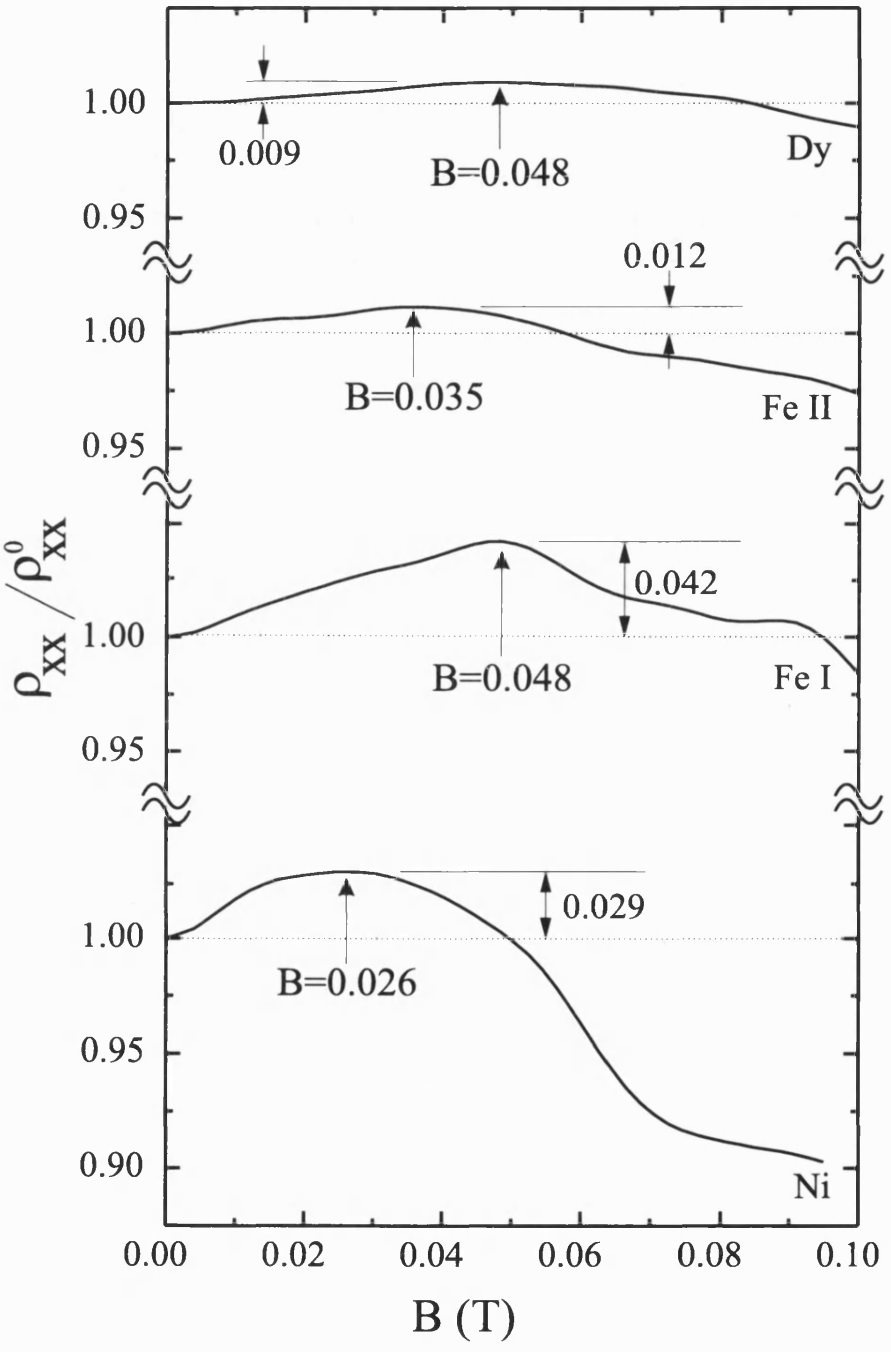

Figure 4.11: Results for the velocity correlation model with 40% diffusive boundaries and the magnetic profiles shown in figure 4.8b.

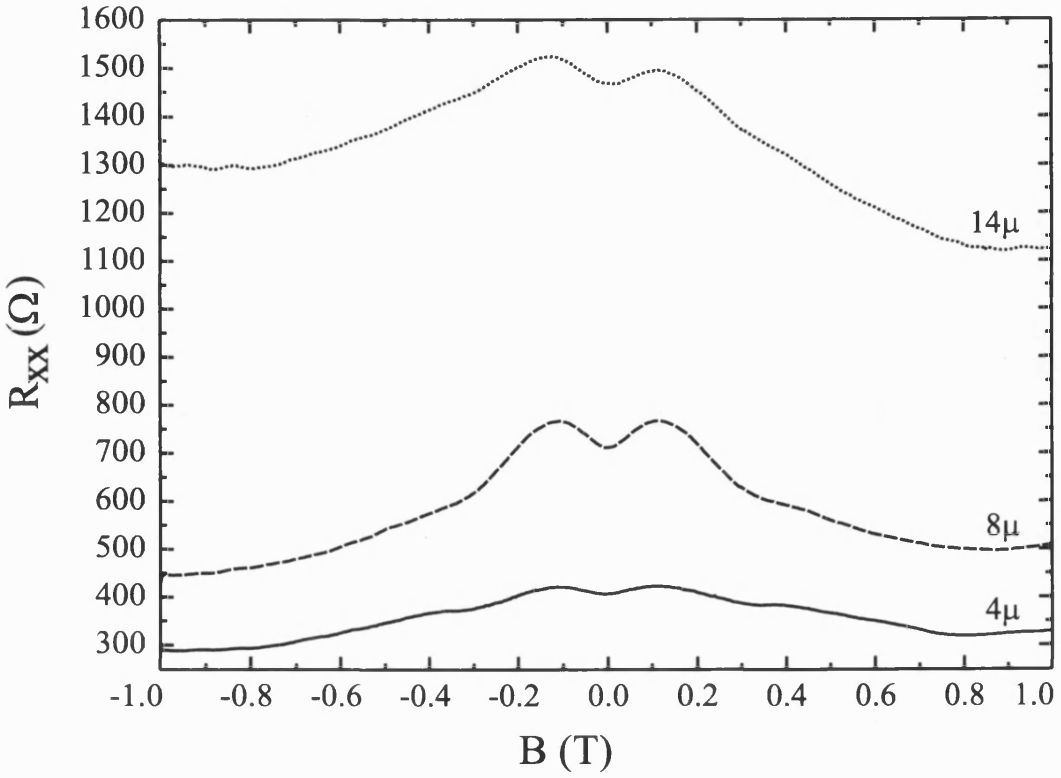

Figure 4.12: Effect of increasing contact separation on resistance.

4.5.2 Contact Separation

Figure 4.12 shows the resistance data for a dysprosium sample (gate voltage = -0.4V) recorded over 4, 8 and 14μm separations. There appears to be some slight variations in the carrier density or possibly the channel geometry is having an effect as the zero field resistances do not quite scale consistently with the contact separation. However, the variation is small and all three traces clearly show the peak structure.

It is easier to compare the normalised resistance, as shown in figure 4.13. It can now clearly be seen that the peak position has not been changed by varying the contact spacing. The peaks are most pronounced in the 8μm trace with the 4 and 14μ traces behaving in a relatively similar manner. There is certainly no evidence for the peaks disappearing even though the spacing is many times the mean free path, $l \sim 2\mu$m.

There are shoulders in the 4 μm data around B=0.4T but otherwise the general shape of the traces is similar with features such as the onset of SdH oscillations on

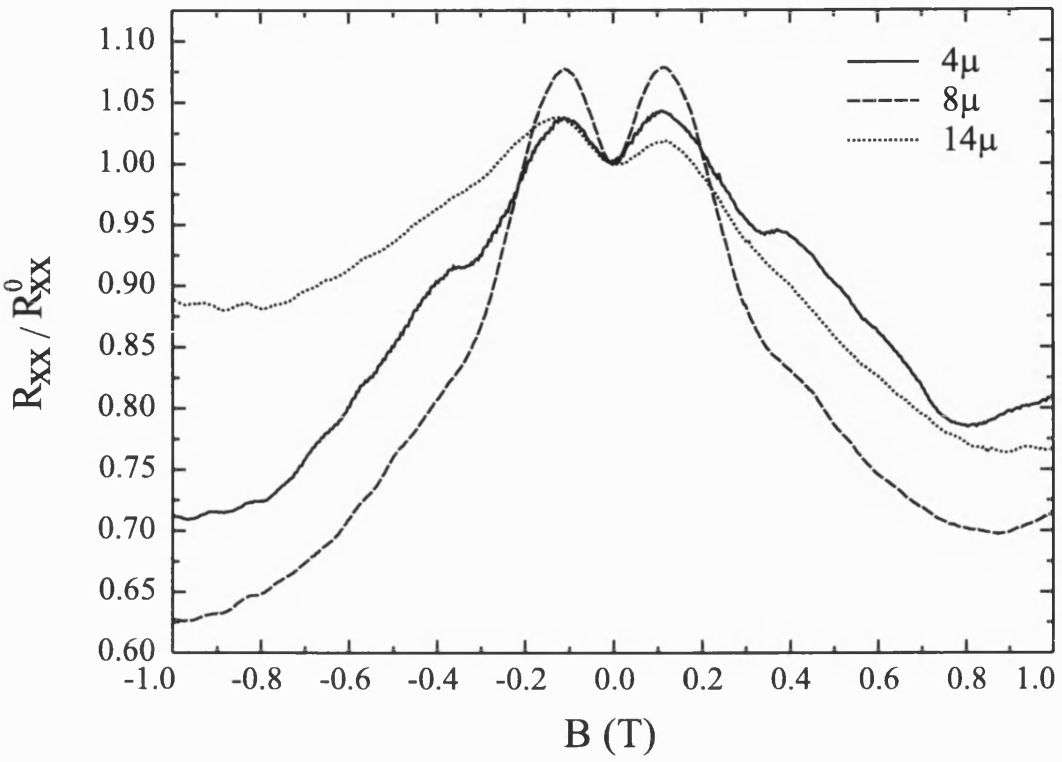

Figure 4.13: Normalised separation resistance data.

the left and the dip on the right occurring at similar values and being of similar sizes.

These results confirm that the origin of the peaks is diffusive supporting the approach taken in the modelling.

4.5.3 Gate Voltage - Effect of Vg on υ_F

As was discussed in the experimental techniques chapter, the gate voltage has an effect on the Fermi level resulting in a change in carrier density. This can be seen clearly in figure 4.14 which shows the Hall effect in a dysprosium stripe sample as the gate voltage is varied. With a positive V_g of 0.2V the Hall coefficient is 1570 giving a carrier density of almost $4 \times 10^{11}\text{cm}^{-2}$. For $V_g = -0.2\text{V}$, the carrier density is around $3.3{\times}10^{11}\text{cm}^{-2}$.

Figure 4.15 shows the change in carrier density and the value of R_{xx} at B=0 for this sample. Note that the change in carrier density is linear from -0.3 to -0.05

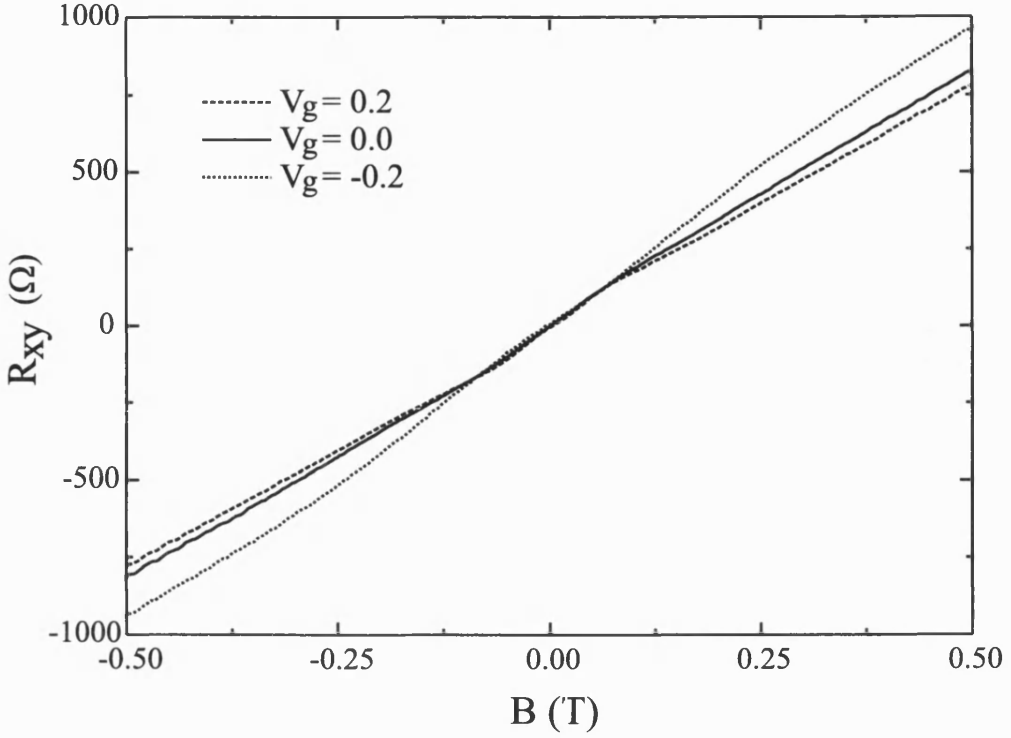

Figure 4.14: Hall traces for varying gate voltages.

and only increases by 25% over the entire range whereas the resistance is non-linear and increases by a factor of 10 from V_g=+0.2 to -0.3. This is probably the result of impurity screening. When the carrier density is high, the electrostatic potential from the donor impurities is well screened. However, as the carrier density falls, the remaining carriers are less screened from the impurities giving an additional resistance increase.

The longitudinal resistances are shown in figure 4.16. There are two major changes in the peak structure as the gate is made progressively more negative. Firstly, the structure becomes more prominent and secondly, the peak separation increases from less than 0.08T to just over 0.3T.

The amplitude of the structure is more than just a general scaling in line with the overall increased resistance. This can be seen by normalising the R_{xx} traces as shown in figure 4.17. The peaks at V_g=0.2 are only 2.7% (on average) bigger than the resistance value at B=0 whereas the peak resistances at V_g=-0.3 are 12% larger than the zero-field value. Also shown in figure 4.17 is the increasing peak separation.

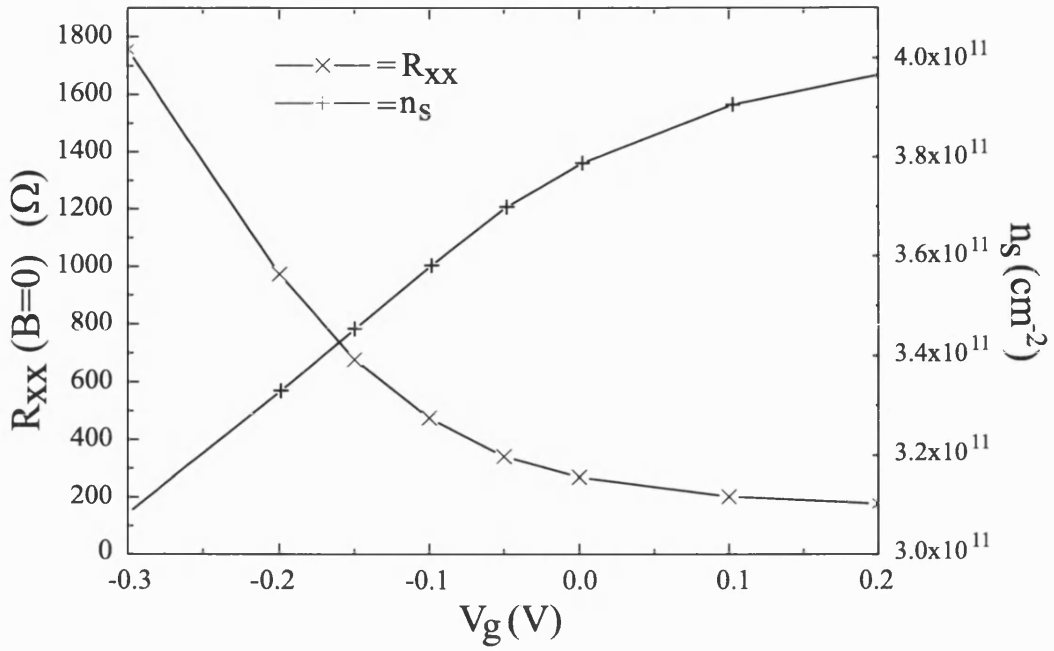

Figure 4.15: Variation of n_s and R^0_{xx} with gate voltage.

The peaks becoming more prominent with decreasing carrier density can be understood by considering the decrease in Fermi velocity. The cyclotron radius is directly proportional to the Fermi velocity, hence, with decreasing velocity, electrons that would have just escaped the magnetic potential, fall into snake/cycloid state trajectories. This appears in the drift diffusion model as an increased maximum allowed angle which reduces the zero field and valley resistances as shown in figure 4.18.

So, although the carrier density is falling, the proportion of electrons trapped in snake/cycloid states is greater and hence the effect is more pronounced. This may also explain one of the differences between the old nickel and iron results compared to the newer iron and dysprosium samples. The older samples had a lower carrier density and the peaks were very clear with no applied bias. It has been repeatedly found with the dysprosium samples that a negative bias is needed to clearly see the peaks.

What is harder to explain is the increased peak separation. There is nothing to suggest that the magnetic profile is changed by altering the gate voltage so any explanation has to come from considering the trajectories.

One possible factor in explaining the behaviour comes from considering the effect

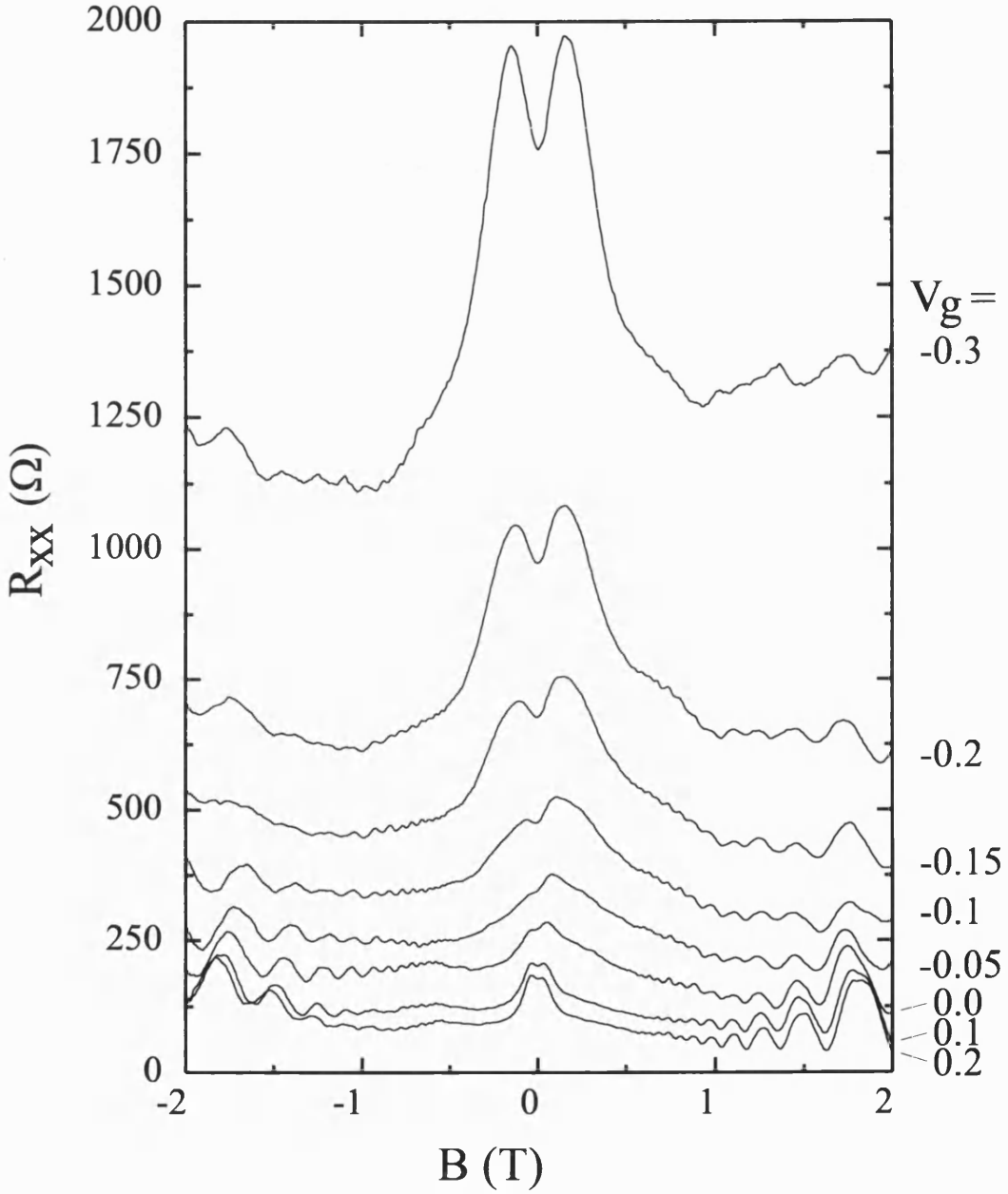

fig:gateRxx

Figure 4.16: R_{xx} traces for V_g from 0.2V to -0.3V.

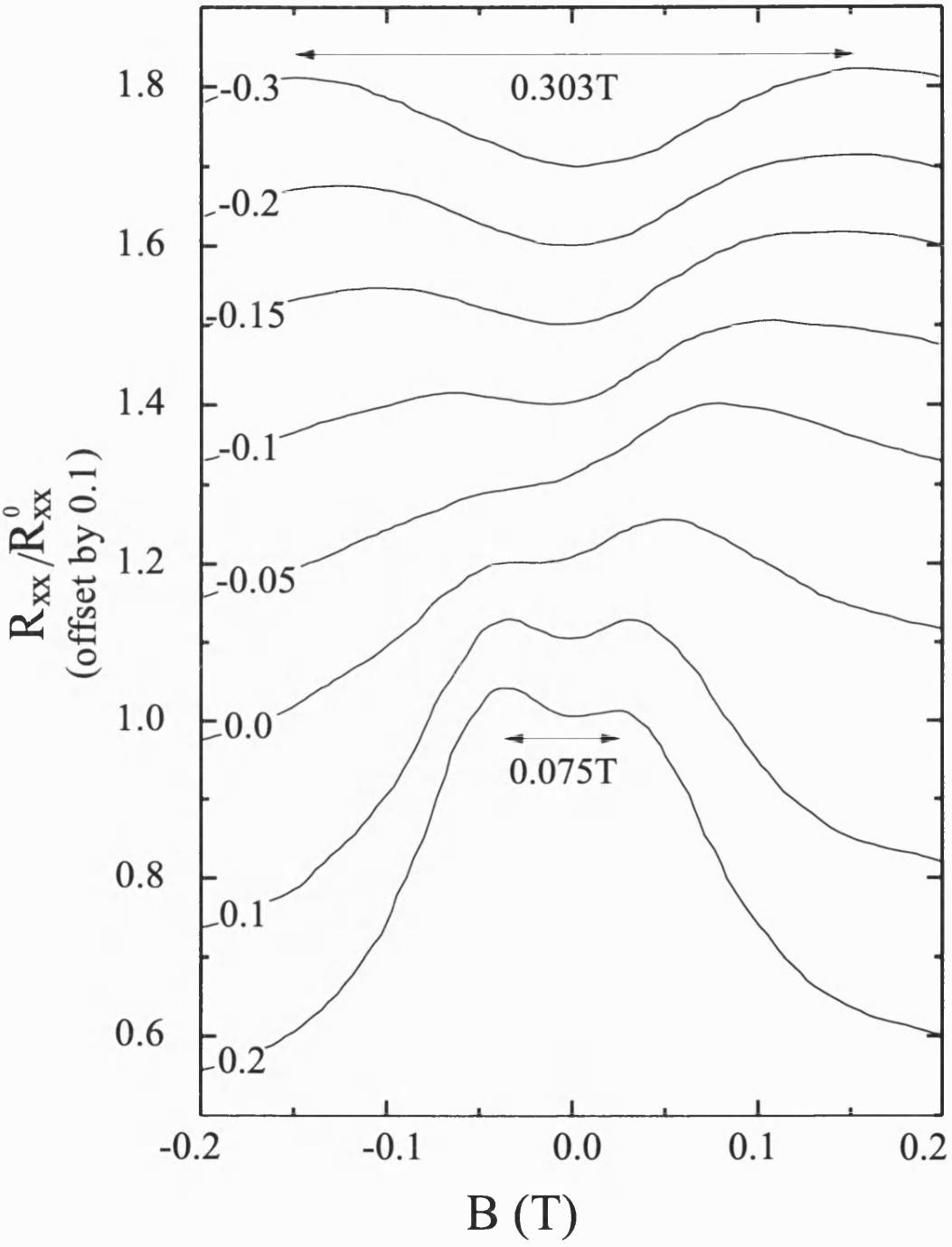

Figure 4.17: Normalised R_{xx} traces for V_g from 0.2V to -0.3V showing peak separation.

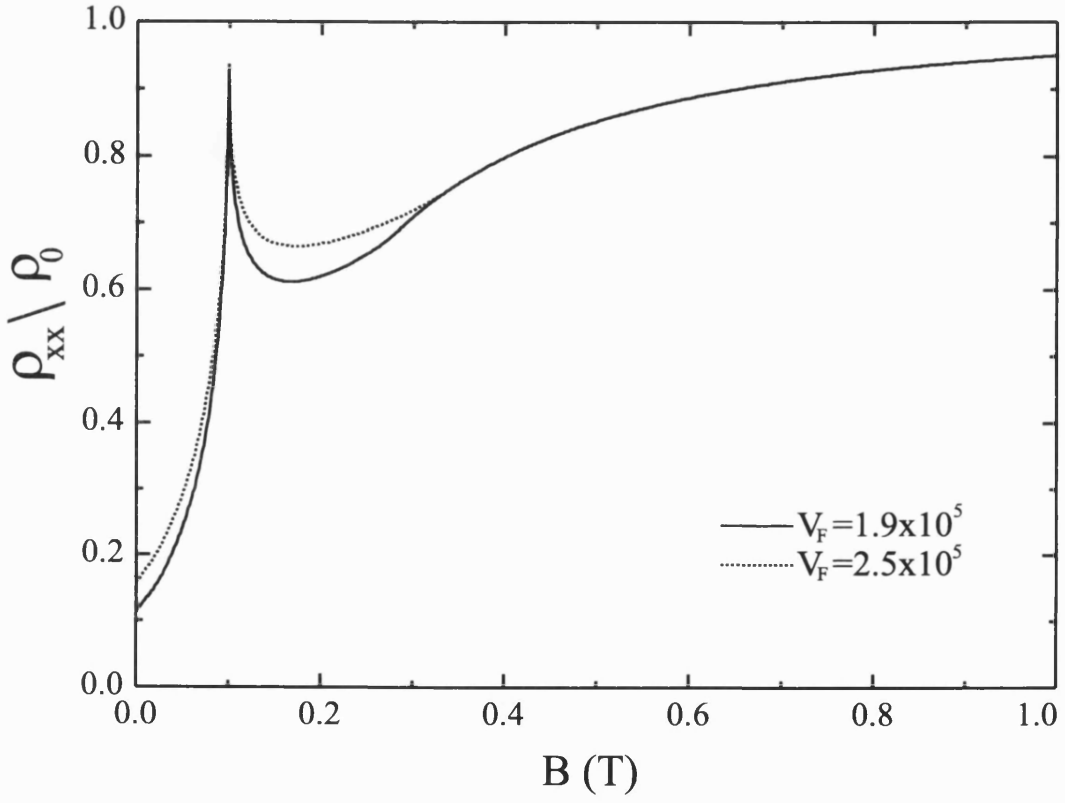

Figure 4.18: Drift diffusion results for ρ_{xx} in a dysprosium sample with increasing Fermi velocity.

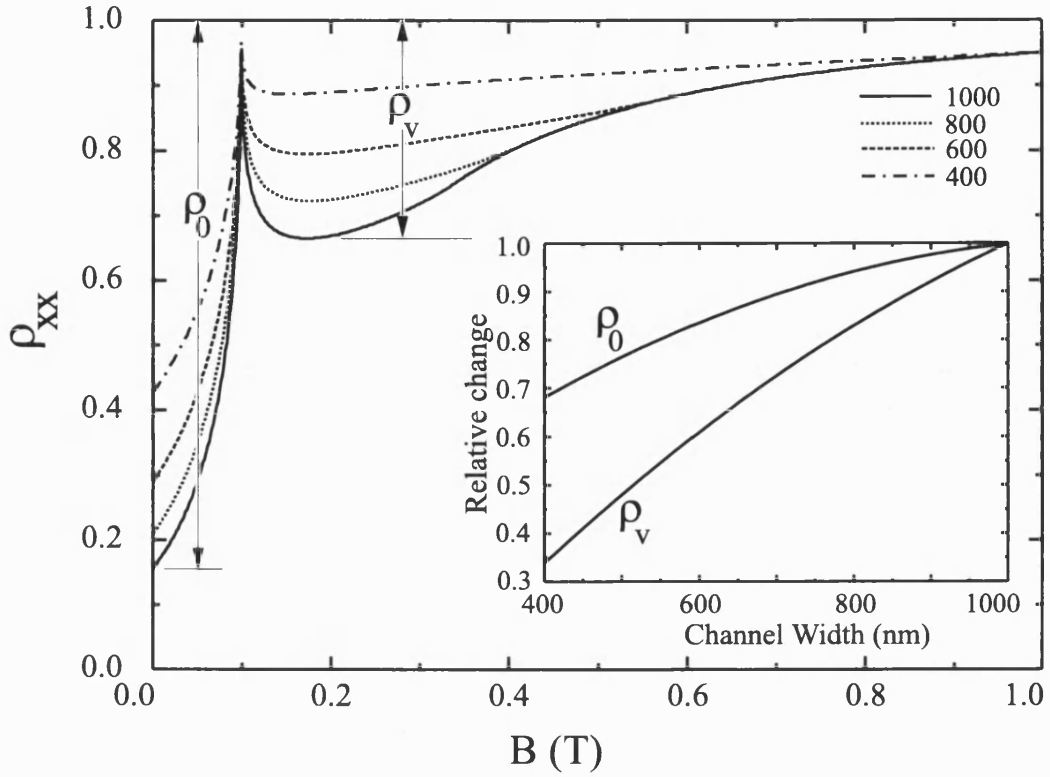

Figure 4.19: Effect of the channel width on snake and cycloid states. Inset shows the stronger effect on cycloid states of reducing the width relative to snake states.

of scattering on snake and cycloid states. Snake states propagate by travelling along lines of zero-field and as such, they can make rapid progress. Cycloid states are inherently slower, their motion being similar to cyclotron orbits, and so are more susceptible to scattering which will increase as the gate voltage is made more negative. This is an idea which will be developed further in chapter 5.

Another factor is that cycloid states are disproportionately affected by the channel width and part of the effect of the increased gate voltage will be to reduce the effective width as the 2DEG depletes from the edges inwards. This effect can be partially seen in the drift diffusion model (figure 4.19). Although the peak position is constant (due to the limitations of the model), the valley caused by the cycloid states shows a 55% decrease when the channel width is reduced by 50% whereas the effect on the zero field resistivity is only 25%. If, as these figures show, the cycloid states are weakened with respect to the snake states, the crossover will occur at higher fields and so the peaks will move to higher magnetic fields.

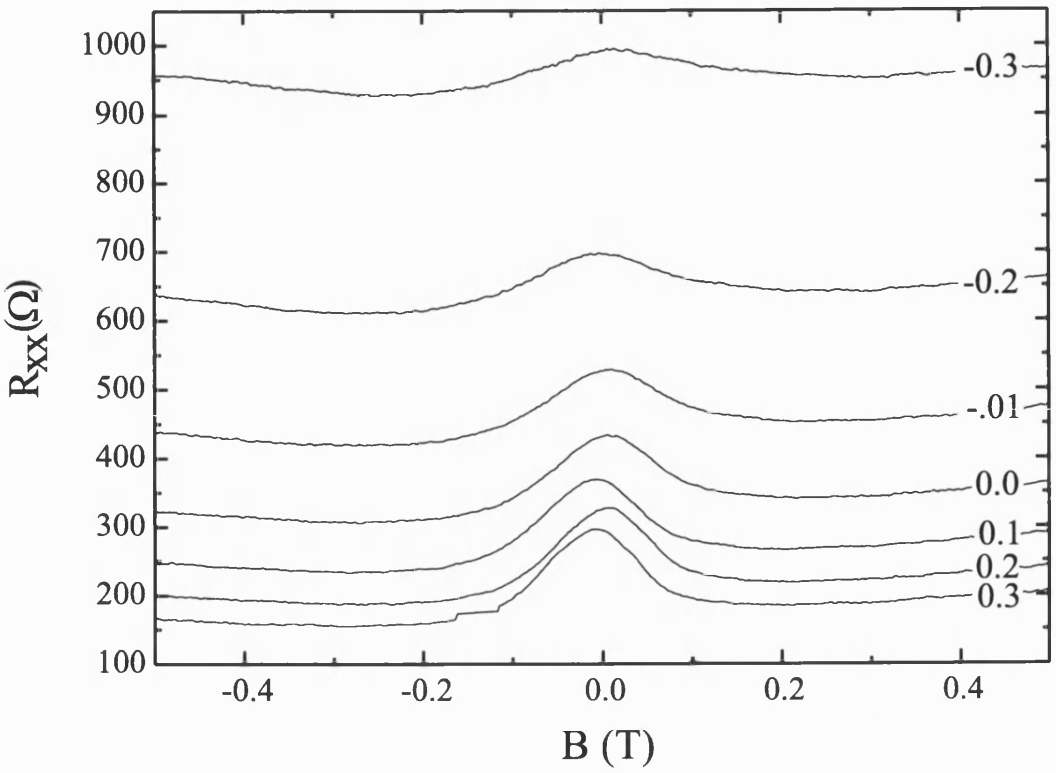

Figure 4.20: Resistance traces as the gate voltage is varied for a sample with no stripe.

Both these factors would reduce the effect of the cycloid states with respect to the snake states and hence the crossover region would move to higher field.

There is, however, a third effect which is more obvious in the samples without a stripe. Figure 4.20 shows the resistance of a 2μm wide sample with no stripe for a range of gate voltages. As before, the resistance increases as the gate becomes more negative but it is also obvious that the shape of the background is changing. The rise around zero field becomes shallower as the 2DEG depletes. This can be attributed to the quenching of the magnetosize effect as the mean free path becomes less than the channel width.

Shown in figure 4.21 are resistance traces for samples with and without a stripe. They are both taken with zero-bias and have been normalised to their respective zero-field resistances for easier comparison. If the result for the sample with stripe is considered as a convolution of the no-stripe sample and peaks resulting from the effects of snake and cycloid states then the relative effect of the channelling only can be extracted by dividing one trace by the other. Although it might seem more natural to take the difference between the traces, that would imply that

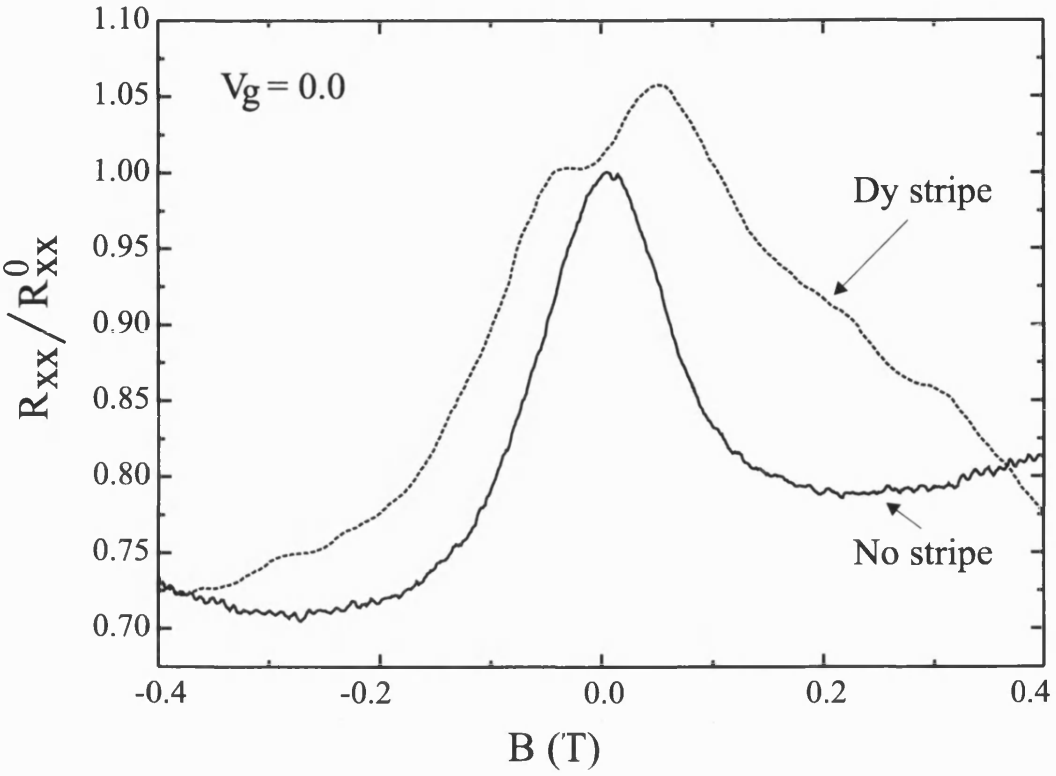

Figure 4.21: Normalised resistance for samples with and without stripes with no gate bias.

the effect of the snake and cycloid states was of a fixed magnitude irrespective of the background resistance. Returning to the data from varying the contact separation (see figure 4.12), it is clear that the magnitude of the effect from the snake and cycloid states increases as the background resistance changes; the peaks in the 14μm trace are significantly larger than those in the 4μm trace. That is not to say that using the idea of a convolution is completely accurate but it is more accurate than the alternative.

Having obtained the effect due to channelling, it can be applied to the other traces from figure 4.20 to show the effect of the changing background on the peak position. The results of this are shown in figure 4.22 and although the results are not particularly clear for positive gate voltages, the negative gate results show over a doubling in peak separation from 0.082 to 0.166T as the gate voltage decreases from 0V to -0.3V.

The actual peak separation is plotted in figure 4.23. The separation goes from around 0.07T with a positive bias to over 0.3T at -0.3V. The value changes

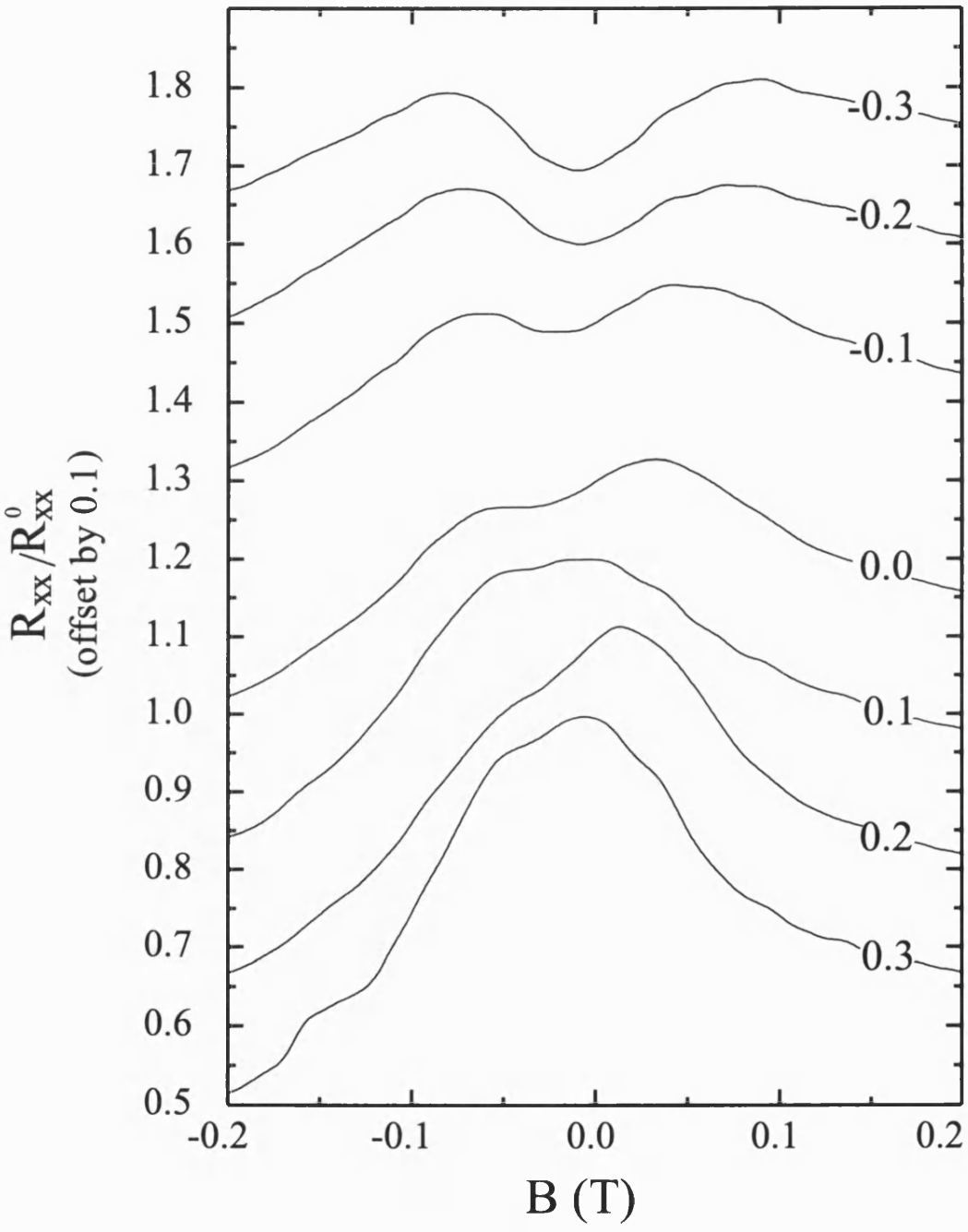

Figure 4.22: Effect of convoluting the varying background of a no-stripe sample with the the channelling peak structure as the gate voltage is varied.

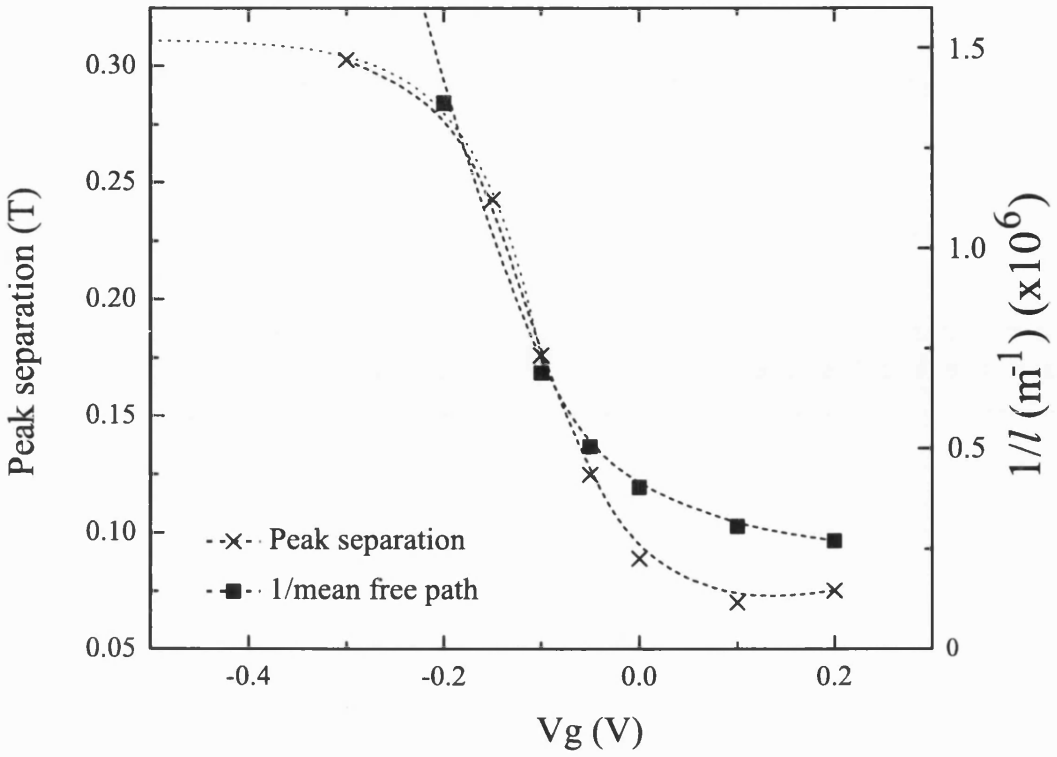

Figure 4.23: Gate voltage dependence of the peak position (×) and inverse mean free path (■) (dashed lines are a guide to the eye). Also shown is the extrapolated behaviour of the peak separation (dotted line).

rapidly in the middle of the voltage range but is tailing off from -0.1V to -0.3V. The separation asymptotically approaches a value of 0.311T suggesting a limit to how far the peak can be moved. This limit would be equivalent to peaks at B=0.155 in between the average negative field of 0.099T and the largest negative field, 0.257T. Also plotted (■) is the inverse of the mean free path to see how the scattering changes with gate voltage. The trends of the two datasets are similar enough to suggest that the scattering may be a factor.

The increase in peak spacing is a very large effect (350% increase) and none of the possible explanations above are entirely convincing. The scattering argument is not entirely consistent with results in chapter 5, the reduction in the 2DEG width is a small effect and using the convolution of a peak structure with the changing background is suggestive rather than conclusive. It is again worth considering alternative explanations.

There is still no sign of peaks in the resistance of the sample without a stripe, so explanations based simply on electrons interacting with the sample boundaries

must be rejected. The presence of the stripe and gate layer may have produced some electrostatic potential in the sample. However, the increasing gate voltage depletes the 2DEG, reduces the Fermi velocity and hence increases the cyclotron radius. If there were any commensurability effects involved, they would occur for fixed values of the cyclotron radius and so the peaks would move together as the negative bias was increased.

Overall, it is hard to explain the magnitude of the peak splitting by any argument. The idea of a peak position on top of a changing background in addition to small changes in that peak position could account for it but there is not enough evidence to push this idea any further.

4.6 R_{xx} and R_{xy}

In section 4.3, equations were given for ρ_{xx} and ρ_{xy} from the drift diffusion model. In particular, eq. 4.12 stated that ρ_{xy} was proportional to ρ_{xx}, implying that peaks seen in the R_{xx} traces due to magnetic channelling should also be seen in R_{xy}. The validity of eq. 4.12 has already been observed in chapter 3 where the angular dependence of R_{xy} showed peaks forming at a constant value of B_z. Further confirmation can be added by examining the effect of gate voltage on the R_{xy} peaks. It has already been shown that the R_{xx} peak separation increases as the gate voltage is made increasingly negative. Figure 4.24 shows the normalised R_{xy} results (linear Hall background removed) which look very similar to the normalised R_{xx} results (figure 4.17). The peak separation increases from 0.092 to 0.476T as V_g changes from +0.2 to -0.3. Over the same range, the peak separation in R_{xx} increased from 0.075 to 0.303T. The greater magnitude of the peak spacing in R_{xy} is a consistent trend through all of the data on these devices but there is currently no explanation for why this should be the case.

4.7 Conclusions

This chapter has tried to provide more information on the factors that can affect snake and cycloid states. Of the three factors investigated, the least significant

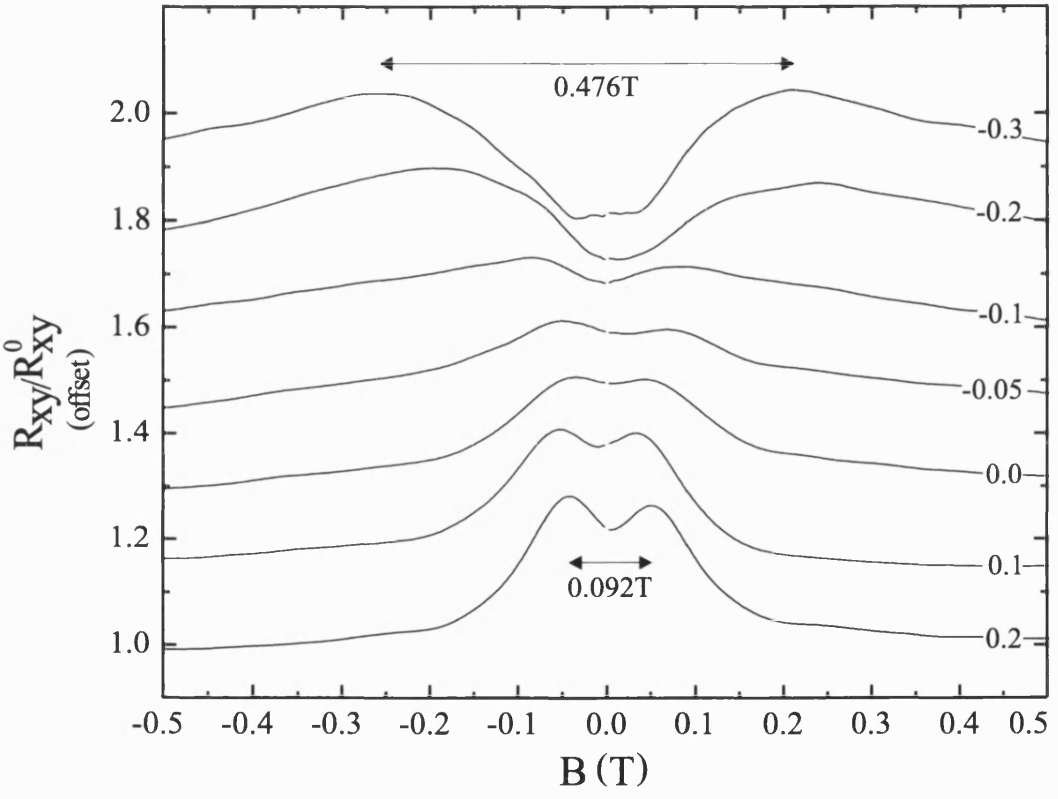

Figure 4.24: Peak separation in the normalised R_{xy} traces with varying gate voltage.

was contact separation. The peak structure was clearly visible from 4 – 16μm with no change in the peak position and generally the same magnetoresistance shape, validating the diffusive approach taken in the modelling.

The other two variables, stripe material and gate voltage both have a significant effect on the peak position and shape. That the peak position varies with the magnetic profile is fairly clear. Relating the peak position, B_p, to the average negative field value, B_1, showed a more consistent trend (ratio of B_p/B_1=0.67 $\pm$ 0.14) than relating it to the minimum field value, B_m, (ratio B_p/B_m=0.36 $\pm$ 0.16).

The situation is complicated by the carrier density in the sample. Lower density samples show a more pronounced effect as the lower carrier velocities lead to a higher proportion of the electrons performing snake orbits. In addition, the peak separation increases as the 2DEG becomes more depleted, which could be linked to an increase in the ratio of snake states to cycloid states at intermediate fields resulting in the crossover moving to higher fields, and a changing background resistance. Reduction in the effective width of the 2DEG and the relatively greater susceptibility to scattering of the cycloid states are possible mechanisms for the changing ratio.

Examining the gate dependence of the normalised Hall resistance reveals a similar trend to the longitudinal resistance with the peaks becoming more widely spaced as the 2DEG becomes depleted.

Two models based on diffusion have been presented in an attempt to examine the effects. The different approaches have different strengths: the velocity correlation model is better at predicting the magnitude of the effect but the drift diffusion model, based on the average magnetic profile, is more accurate for reproducing the peak positions and provides simple feedback on parameter changes.

Chapter 5

Temperature Dependence Of Magnetic Channelling

5.1 Introduction

This chapter investigates the effects of temperature on magnetic channelling. The first section examines the general effects of temperature on 2DEGs before leading into a simple theory for considering the effects on the transport in the specific devices of this thesis. Modifications to the drift diffusion model from chapter 4 are introduced which impose new limits on the snake and cycloid states and enable comparisons to be made with the experimental results. The experimental data falls into two temperature ranges: low temperature from 0-40K and higher temperatures from 50-100K, with different effects in each. Again, the magnetisation of dysprosium proves to have an observable role due to magnetic phase transitions.

5.2 Effects of Temperature

5.2.1 Scattering

Scattering in two dimensional electron gases at low temperature (<100K) is dominated by two interactions: those between electrons and impurities and those between electrons and phonons. Impurities are the most significant factor at normal experimental temperatures (4.2K or lower) and can again be separated into two contributions: scattering from the remote ionized impurities in the AlGaAs layer and scattering from the residual impurities in the 2DEG region. The ionized impurities are normally more important but residual impurities can become important if the spacer layer used to separate the ionized impurities from the 2DEG is particularly wide. Scattering is normally considered through its effect on mobility. The effect of impurity scattering on mobility is normally of the form $\mu \propto T^{3/2}$ [55].

Phonon scattering becomes a major influence once the temperature has risen to around 50K. The exact temperature range is determined by the purity of the sample. Acoustic phonons (disturbances of the lattice) typically interact at lower temperatures but do not couple to the electrons as strongly as the polar optic phonons (movements of the charged atoms within each unit cell) which interact at slightly higher temperatures and dominate above 100K. The effects of phonon scattering on mobility act in the opposite manner to impurity scattering and reduce the mobility as $\mu \propto T^{-3/2}$ [56].

The temperature range over which these processes act is dependent upon the sample; purer materials with higher mobilities are affected more by phonon scattering and the mobility can decrease monotonically with temperature from 4K upwards [57]. Systematic experimental and theoretical studies by Lin and Tsui [58, 59] on devices with mobilities ranging from 4.3×10^3 cm^2/Vs to 8.76×10^5 cm^2/Vs show a transition in behaviour around μ=1×10^5 cm^2/Vs. Samples with mobilities above this threshold behaved in the same way as ref. [57]. Below this value, the samples were affected by impurity scattering and displayed an increase in mobility with temperature up to 70K before the polar optic phonon scattering became dominant and the mobility fell rapidly.

Scattering can also be measured through its effect on properties such as resistance and mean free path.

5.2.2 Carrier Density

So far, the silicon dopant atoms have been assumed to be simply ionized and their electrons transported into the 2DEG. This is not necessarily true as the silicon atoms can also form DX centres [60]. The silicon atoms exist as impurities in the surrounding AlGaAs and it is possible for the lattice to relax around the impurity atoms deepening the potential well for the associated electrons. Depending on the x factor of the $Al_xGa_{1-x}As$, the energy of the DX centre can be within or below the conduction band. For the devices in this report (with x$\sim$0.3) the DX centres are below the conduction band and, as the temperature is lowered below $\sim$150K [60], trap electrons resulting in what is known as 'carrier freeze-out'. In extreme cases this can result in a sample becoming insulating at low temperature [61].

The effect is reversible by illuminating the sample, often through an infra red LED. The potential well of a DX centre has a barrier to entry as well as exit so once the electrons are excited out of the well, they can remain free as long as the thermal energy is less than the entry barrier height. This is referred to as the persistent photoconductivity (PPC) effect.

As the temperature is raised again, the electrons can gain the energy to overcome the entry barrier and can be re-trapped in the DX centres resulting in a drop in carrier density [61].

5.3 Theory

Whether an electron is scattered by an impurity or phonon, the effect is still to alter the electron's trajectory. As the basis of the last two chapters has been electrons being guided by magnetic fields into certain trajectories, scattering represents a potential obstacle. As the temperature is increased, the electron mean free path will decrease and electrons will be in guided orbits for shorter periods.

The question then becomes, how far must an electron travel along a snake or cycloid trajectory for its effect to be felt?

The period of a snake state orbit depends upon the angle, ϕ, at which it departs from the zero-field boundary. The period can be calculated by considering the time spent away from and under the square magnetic barrier (shown in figure 5.2). Away from the stripe the field is B_1 and the cyclotron frequency is ω_{c1} whereas under the stripe the field is B_2 and the cyclotron frequency is ω_{c2}. Adding the time spent in both regions gives a period of:

$$\tau = \frac{2\phi}{\omega_{c1}} + \frac{2\phi}{\omega_{c2}}. \tag{5.1}$$

As the period of a snake state is dependent on the angle, it is possible for it to be vanishingly small, corresponding to the electron travelling directly along the line of zero field between the two regions of different magnetic field ($\phi = 0$).

The cycloid states, however, always have a finite period determined by the magnitude of the modulation introduced by the stripe. If the initial angle is zero (as for the snake state's zero period) the electron will have to perform an entire cyclotron orbit in the second region taking time $2\pi/\omega_{c2}$. This behaviour can be integrated into a calculation of period by modifying the angle with which the electron heads into the region under the stripe in the same way as in chapter 4. The period for a cycloid orbit then becomes:

$$\tau = \frac{2\phi}{\omega_{c1}} + \frac{2(\pi - \phi)}{\omega_{c2}}. \tag{5.2}$$

A simple way to consider the effect of temperature is to compare the scattering time to the period of the orbits. It should be impossible to completely randomise the drift due to snake states as there will always be some with a sufficiently small enough period to survive. However, the drift due to cycloid states should become increasingly randomised once the mean free time becomes comparable with the period given in eq. 5.2.

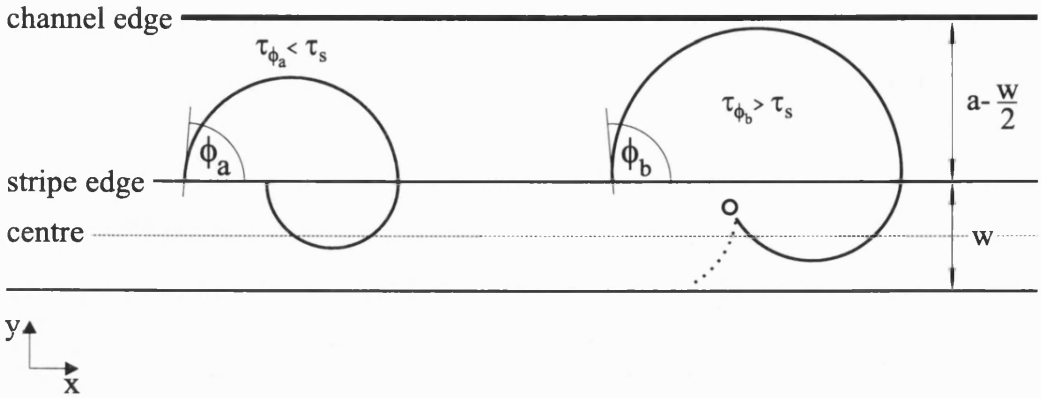

Figure 5.1: New angular limits on the drift diffusion model based on time to complete one orbit.

5.3.1 Modelling

These ideas can be incorporated into the drift diffusion model by requiring the orbits to be completed in less than the scattering time, τ_s.

This introduces new limits on the angle (shown in figure 5.1) obtained simply by rearranging eq. 5.1 and eq. 5.2. The additional limits then become:

$$\phi_{ss} = \left(\frac{\tau_s}{2(\frac{1}{\omega_{c1}} + \frac{1}{\omega_{c2}})} \right), \tag{5.3}$$

for snake states and:

$$\phi_{cs} = \left(\frac{\frac{\tau_s v_F}{2} - \pi r_{c2}}{r_{c1} - r_{c2}} \right), \tag{5.4}$$

for cycloid states.

The new equations for the drift velocity then become:

$$\langle v_d^2 \rangle = \frac{v_F^2}{\pi} \int_0^{\phi_{max}^{ss}} \left(\frac{\sin\phi}{\phi} \right)^2 d\phi, \tag{5.5}$$

where $\phi_{max}^{ss} = \min(\phi_1, \phi_2, \phi_{ss})$

and:

$$\langle v_d^2 \rangle = \frac{v_F^2}{\pi} \int_{\phi_2'}^{\phi_{max}^{cs}} \left(\frac{B_2 - B_1}{\pi B_1 + \phi(B_2 - B_1)} \sin\phi \right)^2 d\phi, \tag{5.6}$$

where $\phi_2' = \pi - \phi_2$ and $\phi_{max}^{cs} = \min(\phi_1, \phi_{cs})$. Note ϕ_1 and ϕ_2 retain their original definitions from chapter 4.

Figure 5.2 shows the results of this model on a 2μm wide dysprosium sample with a step profile from B_1=-0.099T to B_2=0.498T. As the scattering time decreases, both the zero-field dip and the valley beyond the peak are affected. The valley resistance, as well as diminishing in magnitude also moves to higher field values. This is because the cyclotron frequency increases with magnetic field strength so the orbital period decreases as the field increases, see eq. 5.2. Eventually, the period will drop below the scattering time and the cycloid states re-emerge. The 50ps trace represents the unscattered result as even the longest possible orbits are completed in less than this time.

The snake states are slow to be affected by the scattering, the change between 50ps and 10ps is small compared to the changes for 5ps and 3ps. The cycloid orbits are more strongly affected, the valley minimum moves from 0.172T to 0.272T, 0.489T and finally 0.805T with a decrease in magnitude each time. As the scattering time was the only parameter varied, the curves tend toward the same behaviour as the 50ps trace once the field is high enough to overcome the scattering time.

These results show the snake states still having an effect even when the cycloid states have been almost eliminated, confirming that the snake states vanishingly small period gives them far greater resistance to scattering.

5.4 Temperature Dependence of Magnetic Channelling

As mentioned in the introduction to this chapter, the experimental data falls neatly into two regimes, 1-40K and 50-100K. The first of these regimes allows us

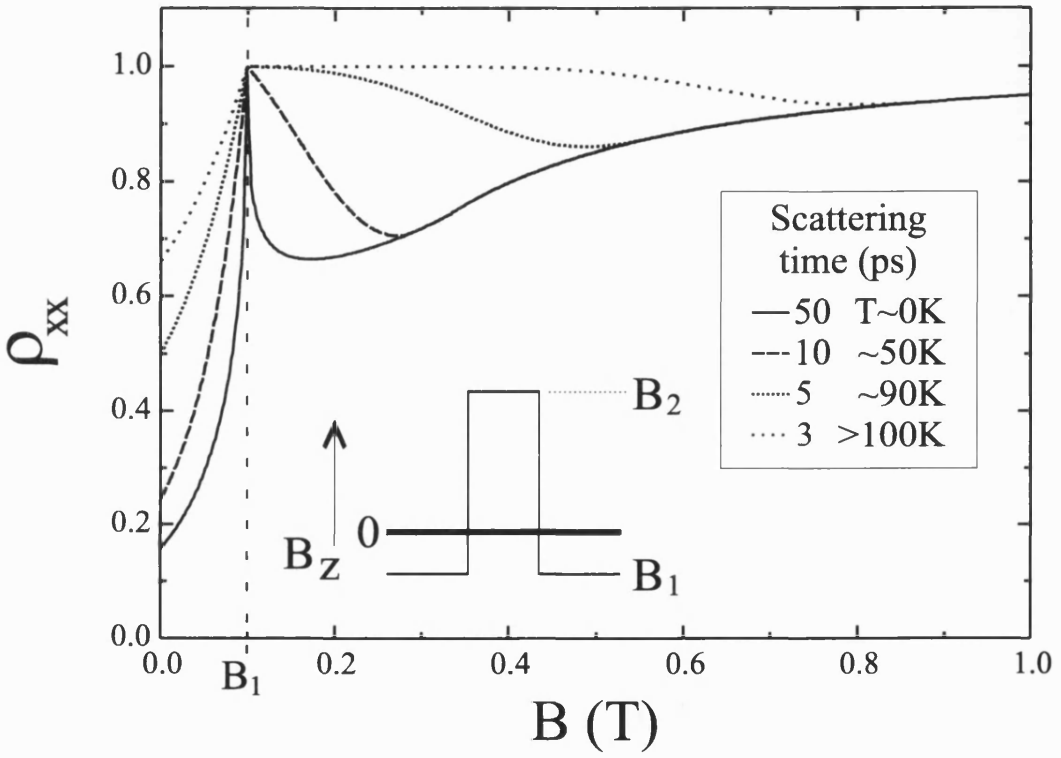

Figure 5.2: Drift diffusion model showing the effect of decreasing scattering time on snake and cycloid states. The potential used (a step from -0.099T to 0.498T) is also shown.

to investigate the relative temperature dependence of snake and cycloid states and also shows some interesting behaviour of the 2DEG itself. In the higher temperature regime, only the effect of snake states can be observed but changes in the peak structure around the Curie temperature of dysprosium reveal more information on the robustness of snake states and the magnetisation of dysprosium.

5.4.1 Low Temperature Results - 1 – 40K

All the results in this thesis so far have been taken at 4.2K or below. These temperatures are necessary for the superconducting magnets but it is possible to heat the sample without quenching the magnet by using a variable temperature insert (VTI). The results for different temperature were taken approximately one hour apart giving the temperature time to stabilise.

This first section focuses on the behaviour below 50K as shown in figure 5.3. Two features are marked on the figure, R_0 and R_v, corresponding to the differences between the peak and zero-field resistance and the peak and subsequent valley resistance respectively. The peak marks a crossover between snake and cycloid states, hence R_0 and R_v can be considered indicators of the channelling by snake states and cycloid states respectively.

Examining the high field regions (>1T) of figure 5.3 first, there is a clearly increasing background resistance as the temperature is increased. However, this trend is reversed below 1T where the 1.35K and 9.7K traces show the highest resistance and the 40K curve has the lowest zero-field resistance. Hall resistance measurements (figure 5.4) show the carrier density increasing over this temperature range and the same decreasing resistance is observed in a sample without a stripe indicating that this is a feature of the 2DEG rather than the channelling. R_0 is present in all the curves and even becomes larger as the temperature increases. R_v does not display the same robustness and is a successively smaller effect with each temperature increase up to 20K. There is no valley for T $\geq$29K although this is somewhat confused by the increasing background. The Shubnikov-de Haas effect also become weaker with increasing temperature with the strong oscillations at 1.35K barely discernable at 20K. These observations are clearly in line with the theory of the last section, namely that the snake states are robust with

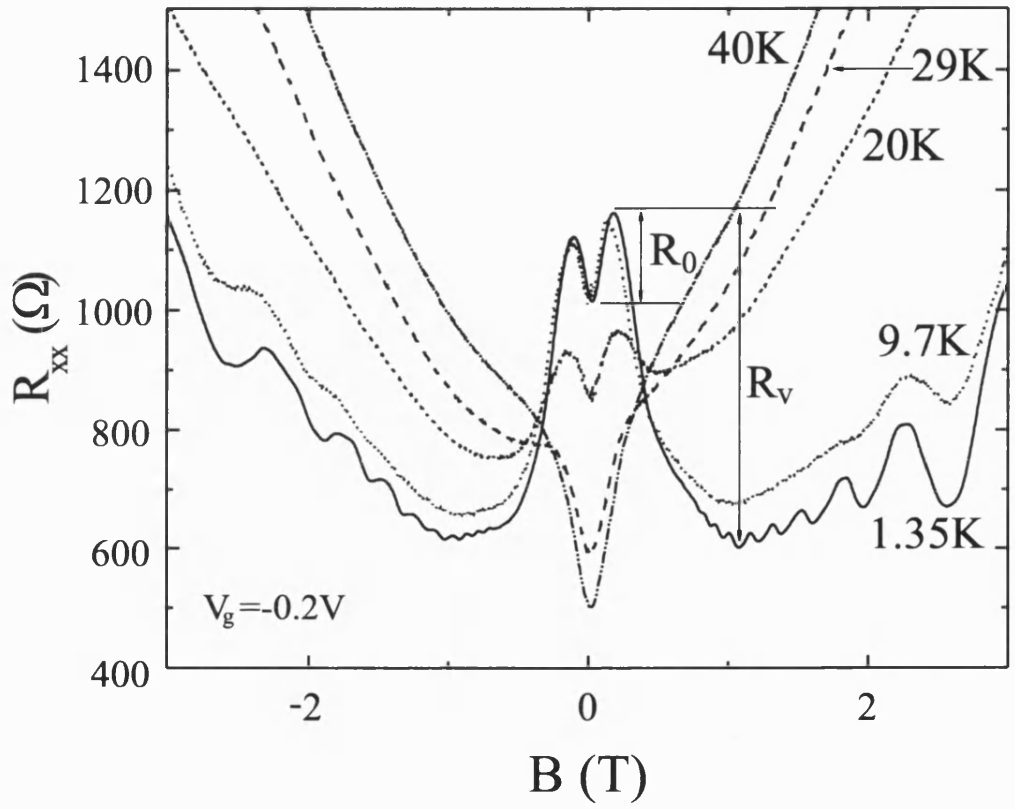

Figure 5.3: Temperature dependence of R_{xx} showing the peak size, R_0, and the valley magnetoresistance, R_v.

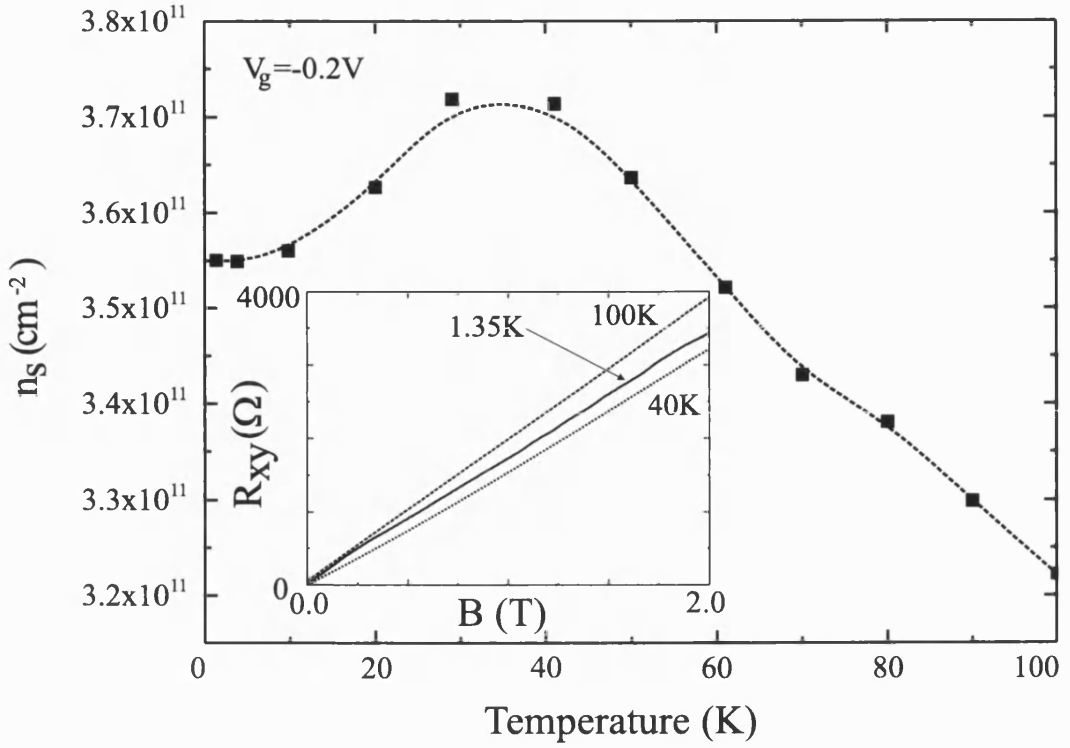

Figure 5.4: Carrier density for T=1.35K to T=100K (dashed line is a guide to the eye). Inset shows selected Hall resistance traces for 1.35K, 40K and 100K.

respect to temperature increases whereas the cycloid states (and Shubnikov-de Haas oscillations) are rapidly quenched by increasing temperature.

Another aspect that can be considered is the similarity between the period of cycloid states and cyclotron orbits. If the period to complete a cycloid state is τ_{cs} then a cyclotron orbit will take the same time in the same average magnetic field:

$$\overline{B} = \frac{B_1\tau_1 + B_2\tau_2}{\tau_1 + \tau_2}\ \text{(cycloid)}\ \equiv \frac{2\pi m}{e\tau_{cs}}\ \text{(cyclotron)}, \tag{5.7}$$

where $\tau_1 = 2\phi/\omega_{c1}$ and $\tau_2 = 2(\pi - \phi)/\omega_{c2}$ are the times the electron in the cycloid state spends away from and under the stripe respectively and $\tau_{cs} = \tau_1 + \tau_2$.

This average magnetic field will depend upon the profile of the stripe but as a rough calculation, a cycloid state period of 10ps would be equivalent to the time taken for a cyclotron orbit in a field of 0.24T. Because of this similarity, the manifestations of cyclotron orbits and cycloid states (evidenced through the Shubnikov-de Haas oscillations and valley resistance respectively) should decay in a similar fashion as the temperature is increased. The magnitude of these

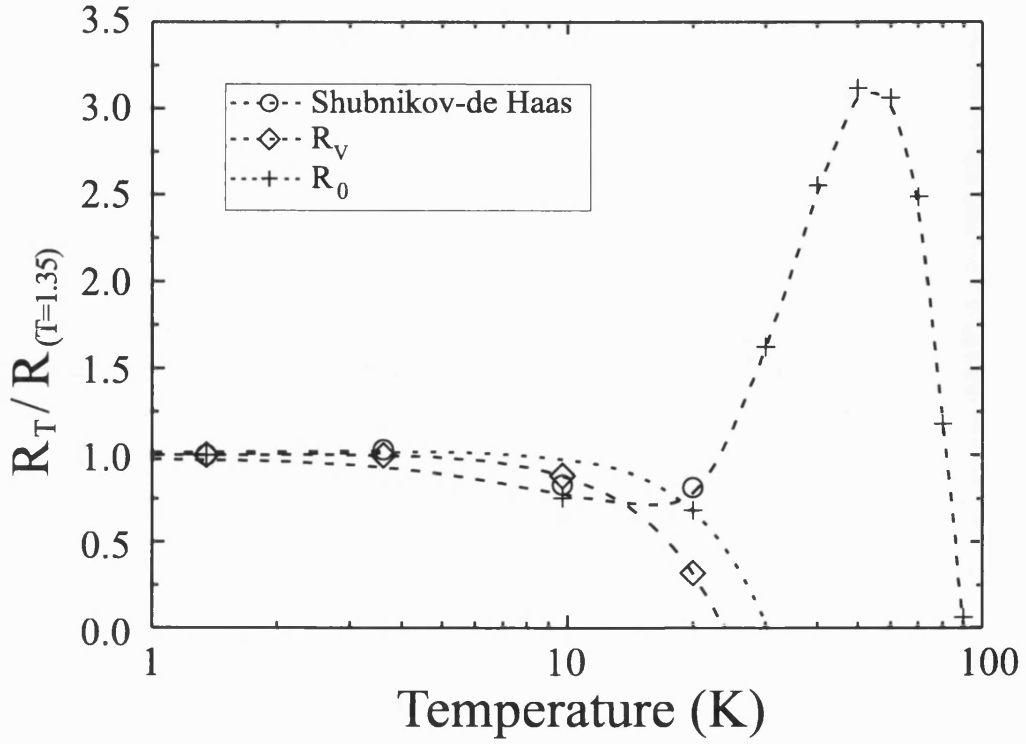

Figure 5.5: Temperature dependence of the peak amplitude, R_0, the valley resistance, R_V, and the Shubnikov-de Haas oscillations showing the similar decline of latter two. Dashed lines are guides to the eye. (log scale).

effects (taken from figure 5.3 and normalised to the value at T=1.35K) is plotted against temperature in figure 5.5 which also plots the peak amplitude. Up to 10K the three curves are very similar; after 10K they diverge with the snake states becoming stronger (exaggerated by the changing background resistance) and the cycloid states and Shubnikov-de Haas oscillations diminishing. The cycloid states show a smoother decay than the Shubnikov-de Haas oscillations but both disappear between the 20K and 30K readings.

Comparison to Chapter Four

Explanations of the results seen when varying the temperature in this chapter (see figure 5.3) and the gate voltage in the last chapter (see figure 4.16) have both been linked to scattering. However, the observed behaviour is different for the two cases. How can this difference be reconciled?

Examining the chapter four results first, as the gate voltage was made increasingly

negative (up to -0.3V), the peak separation increased but the overall shape of the magnetoresistance was similar. Importantly, the Shubnikov de-Haas oscillations were still obvious even at V_g=-0.3V. By contrast, the results for T=1.35 to 40K show little variation in peak separation but the shape varies considerably with both the valley resistance, R_v, and the Shubnikov de-Haas oscillations being rapidly quenched. It should also be noted that the temperature results were taken with a gate bias of -0.2V; figure 4.23 showed that with this bias, the peak separation was already approaching saturation.

With the information from both experiments, it is possible to build a picture of what may be happening. It was shown in the last section that the Shubnikov de-Haas oscillations and cycloid states have a similar dependence on scattering. As the Shubnikov de-Haas oscillations were not significantly disrupted by the gate voltage variation, it is not surprising that the valley resistance, indicative of cycloid state channelling, was also not affected. Similarly, there was not a large change between the peak position for -0.2 and -0.3V so it is not unreasonable that there should be little change when the temperature is varied.

Essentially, these results suggest that increasing the temperature represents a far more effective way of disrupting the transport than depleting the 2DEG. The situation is complicated, in both cases, by the complex response of the 2DEG itself but the results are not necessarily contradictory.

5.4.2 High Temperature Results - 40 – 100K

In the low temperature results, it was seen that the snake states were better able than cycloid states to resist the scattering introduced by temperature. This robustness is now examined at higher temperature.

First though, the results at high field and high temperature are examined. Figure 5.6 plots the changing resistance at different values of the magnetic field to examine the scattering. The best fit to the curves above 1T was found to be a $T^{1/2}$ behaviour (dashed line), characteristic of piezoelectric acoustic phonon scattering [55]. The $T^{1/2}$ lines for 0 and 0.1T were fitted to the 100K point (well above dysprosium's Curie point) to avoid any channelling effects. It can be seen that the experimental points do not display the same behaviour as the fit provid-

ing the first evidence for the persistence of snake states all the way to the Curie point.

Moving to the actual resistance traces, figure 5.7 shows the results for T=50K to T=100K. The absence of the valley due to cycloid states makes these traces look somewhat unfamiliar but R_0 is still present. It is difficult to determine the peak position from the R_{xx} data so the 2nd derivative has been used (inset to figure 5.7) to identify the positions. The slight decrease in peak separation can be attributed to dysprosium's weakening ferromagnetism as the Curie temperature is approached and the reduction of R_0 between 50K and 80K can be explained by increased scattering. However, at 90K, there are still small peaks whose separation actually increases from 0.42 to 0.55T as the temperature is raised to 100K. The origin of this unexpected behaviour lies in the magnetisation of dysprosium changing from ferromagnetic to helical and will be explained in section 5.5.

It has already been shown that the theory connecting the period of cycloid and cyclotron orbits could help explain their similar decay. The drift diffusion model can now be used to examine R_0 from 1.35K to 100K. This is done by using the carrier density of the sample and the experimental zero-field resistances to calculate an approximate value of the scattering time. Inputting this value into the drift diffusion model allows R_0 to be calculated. The comparison between the model and the experiment is shown in figure 5.8. The height of the peak has been normalised to the zero-field resistance to aid comparison. The model predicts a similar trend to the data but overstates the size of the effect (note different axes for experiment and model). Both traces show small variations until T=20K at which point they start a rapid increase which peaks between 40 and 50K. Both then decrease rapidly until 80 - 90K when the snake states are quenched due to going above dysprosium's Curie temperature.

One reason for the model showing a larger effect is the assumption that one orbit must be completed within the scattering time. If more than one orbit was required, the size of the effect would decrease. Putting the different amplitudes aside, there is a qualitative agreement between the measured and calculated temperature dependence of snake states.

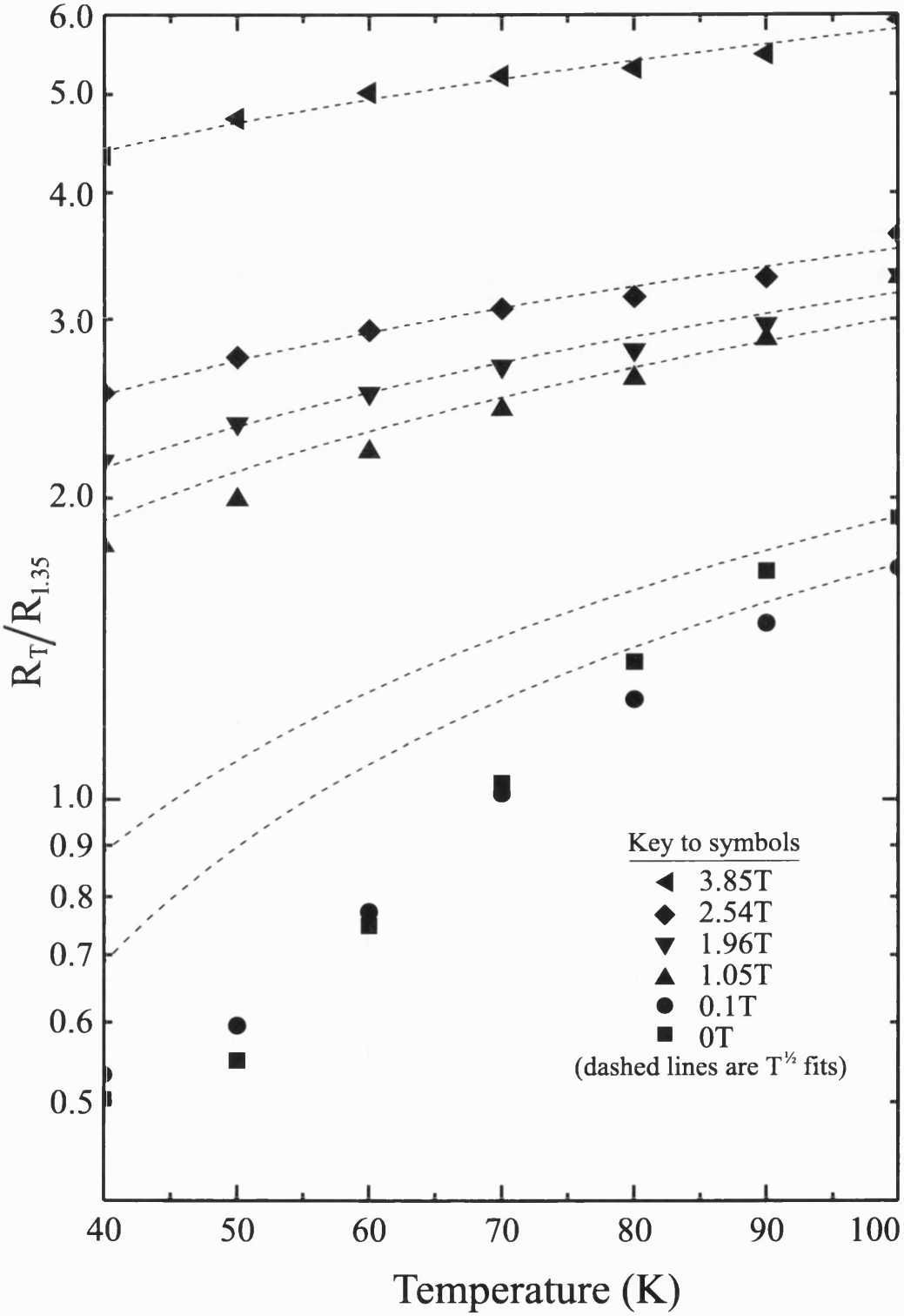

Figure 5.6: $T^{1/2}$ fits (dashed lines) to the resistance changes at varying values of magnetic field (see key for values). The departure from the $T^{1/2}$ behaviour for the two lower data sets is the consequence of snake state channelling.

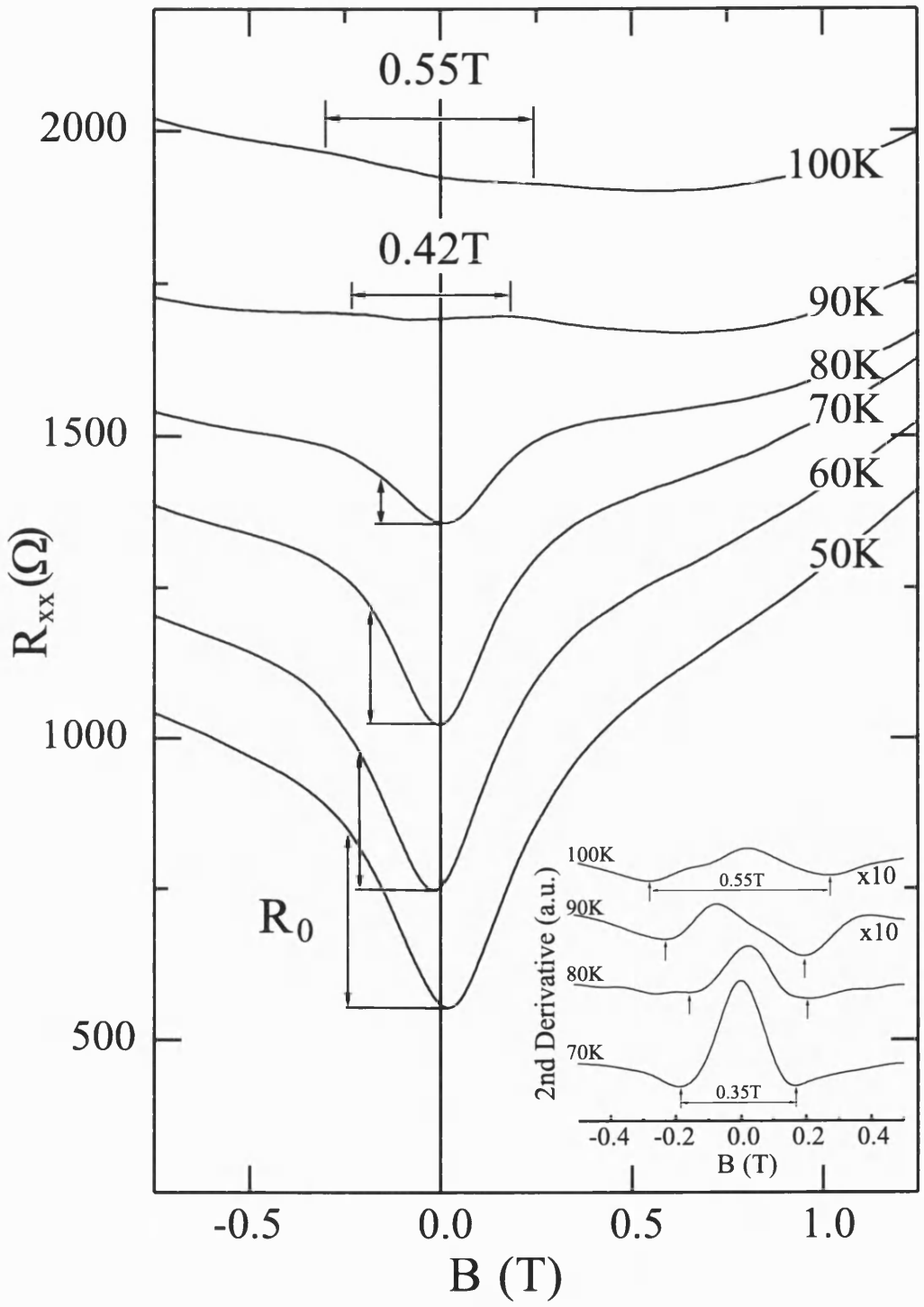

Figure 5.7: R_{xx} traces from 50 to 100K. Insert shows the 2nd derivatives used to identify peak positions.

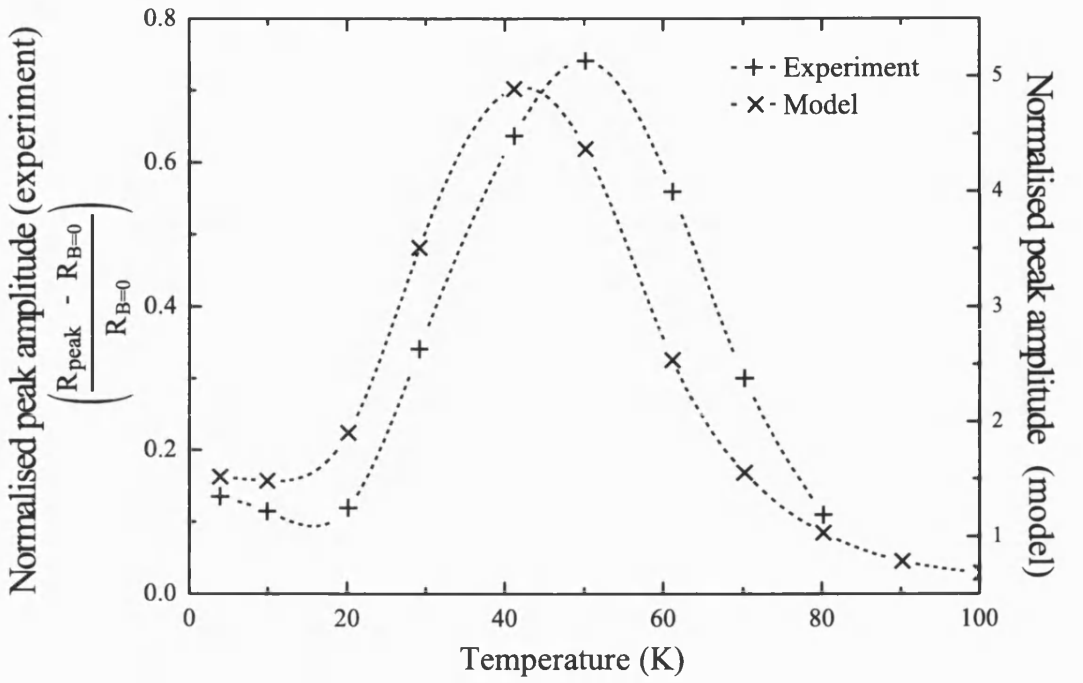

Figure 5.8: Comparison of the normalised peak amplitude from the experimental data and model. Dashed lines are guides to the eye.

5.4.3 Hall Resistance Measurements

The similarities between R_{xx} and R_{xy} have been shown in both of the last two chapters. The changing shape of R_{xx} due to the suppression of cycloid states presents an additional opportunity to investigate the connection between R_{xx} and R_{xy}. Figure 5.9 shows the normalised Hall resistance for temperatures from 1.35 to 100K. The changes that occur in R_{xx} are duplicated here with the 1.35 and 9.8K showing an almost identical peak structure which then changes to just a zero field dip at 40K. As the temperature is raised further, the size of the dip decreases until there is only a slight disturbance around zero-field at 100K.

Every experimental parameter varied has resulted in the behaviour in R_{xx} being duplicated in R_{xy}. As the angle was changed, so the R_{xy} peaks formed at constant B_z. As the gate voltage varied the separation in R_{xx}, so did the separation change in R_{xy}. Now, the changing shape in R_{xx} due to the quenching of cycloid states has been mimicked in the changing R_{xy} profiles.

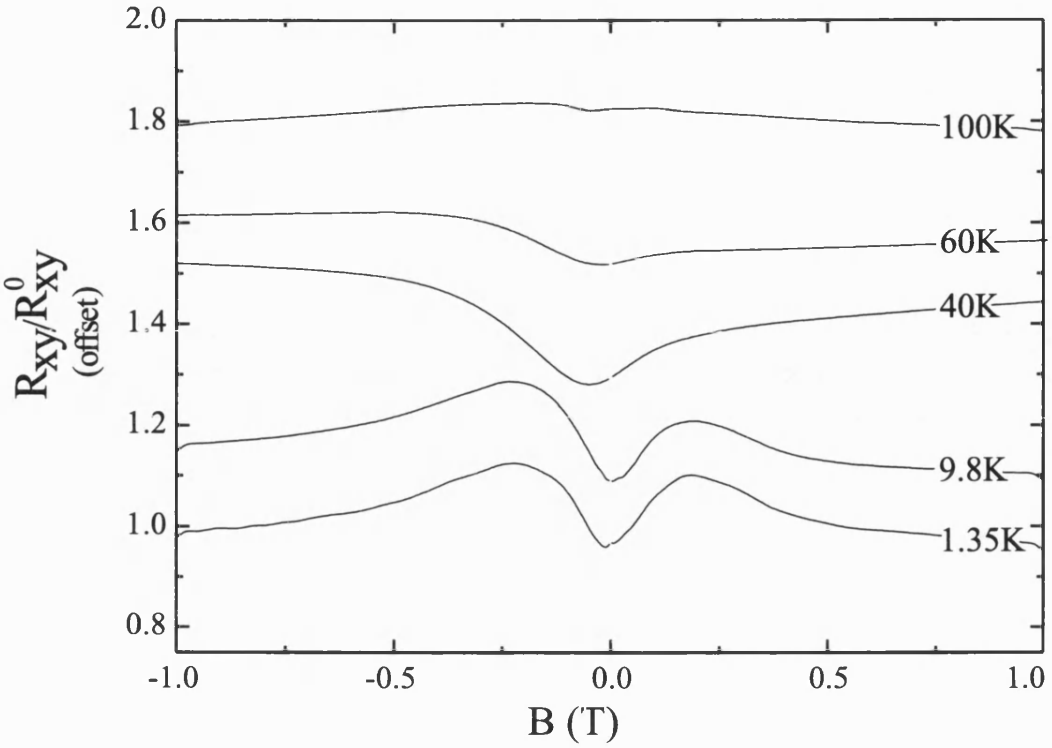

Figure 5.9: Normalised R_{xy} traces (background Hall resistance removed) for temperatures from 1.35 to 100K.

5.5 Dysprosium Magnetisation II

The end of chapter 3 looked at the magnetisation of dysprosium at low temperature as the stripe was rotated in an external field. Then, the large crystalline anisotropy resulted in the stripe preferentially magnetising perpendicularly to the 2DEG. The stripe's ferromagnetism has not been an issue so far as iron and nickel's Curie temperature are over 500K. However, dysprosium's Curie temperature is 88K, which falls in the temperature range of the experiments in this chapter. Most ferromagnets become paramagnetic above the Curie temperature but this is not the case for dysprosium which has an additional magnetic phase between ferro- and paramagnetism.

5.5.1 Helical Spin Configuration

Magnetic spin structures in the rare earth metals were investigated by neutron diffraction experiments at the beginning of the 1960s. Wilkinson *et al.* [62] stud-

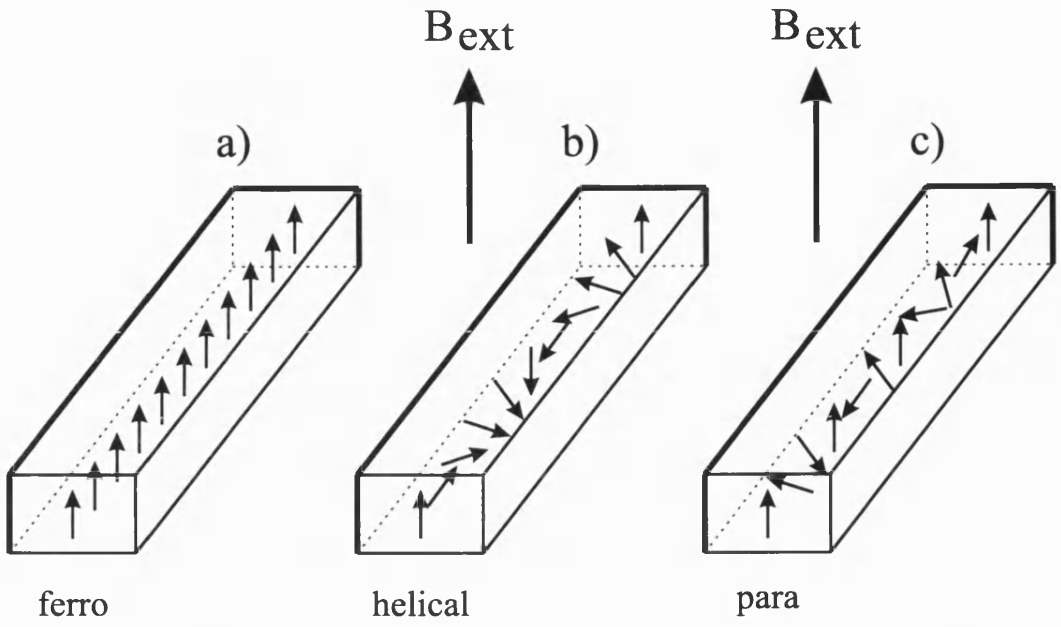

Figure 5.10: The three phases of dysprosium's magnetisation; a) ferromagnetism where all the magnetic moments align, b) helical magnetisation where the moments rotate to minimise the overall magnetisation but can be realigned by a sufficiently large field and c) paramagnetism where there is a weak alignment increasing with the external field. See text for further explanation.

ied dysprosium and found it to have a helical spin structure between the Curie and Néel temperatures. The Néel temperature represents the point above which the spin ordering is randomised (normally used to characterise antiferromagnetic materials) and is 179K for dysprosium [43]. Figure 5.10 illustrates the behaviour in the three phases. Part a) shows the ferromagnetic phase where the moments align to a small external field, b) shows the more complicated helical phase. The spins in each plane (parallel to the front face) are aligned with each other but the next plane's spins are all slightly rotated. The overall effect is to minimise the total magnetisation of the material. However, a feature of helical magnetisation is that the spins can be brought back into ferromagnetic alignment by applying an external field above a critical value. As the temperature is increased the external field required also increases. Finally, c) shows the paramagnetic state where the temperature has disordered the spins. As the external field is increased, these spins gradually rotate to align to the external field resulting in a magnetisation proportional to the external field.

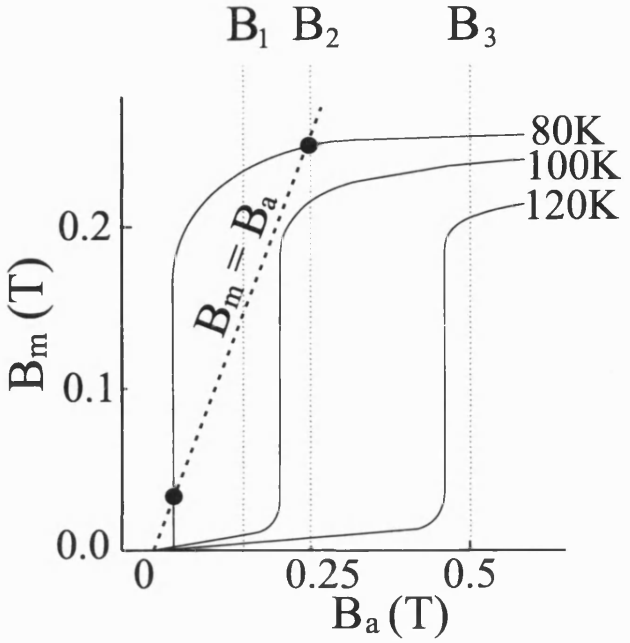

Figure 5.11: Dysprosium isotherms showing the modulation, B_m, against the applied field, B_a. The dashed line shows where the applied field is equal to the negative modulation from the stripe.

5.5.2 Residual R_{xx} Peaks Explained

It was mentioned above that there is a critical field for the restoration of spin alignment in the helical phase. The magnetisation isotherms for dysprosium can be seen in figure 5.11 (adapted from Legvold [43]). B_a is the applied field and B_m was obtained by taking the value of M_s from Legvold and then finding the minimum of the magnetic profile for a stripe with that saturation magnetisation. The isotherms are given for three temperatures, 80, 100 and 120K. At 80K dysprosium is still ferromagnetic so a small applied field results in the magnetisation rising rapidly. At 100K the dysprosium is in its helical phase and the magnetisation rises slowly as the applied field is increased. A field of 0.2T must be applied before the spins suddenly align resulting in the magnetisation rising rapidly again. Note that the entire isotherm is to the right of the $B_m = B_a$ line showing that the magnetisation is never larger than the applied field. The 120K isotherm has the same behaviour as the 100K trace but a field of almost 0.5T is required to magnetise it. It is also noticeable that the final value of the magnetisation decreases as the temperature increases. This behaviour also extrapolates to lower temperature where the ferromagnetic effect is slightly stronger [63].

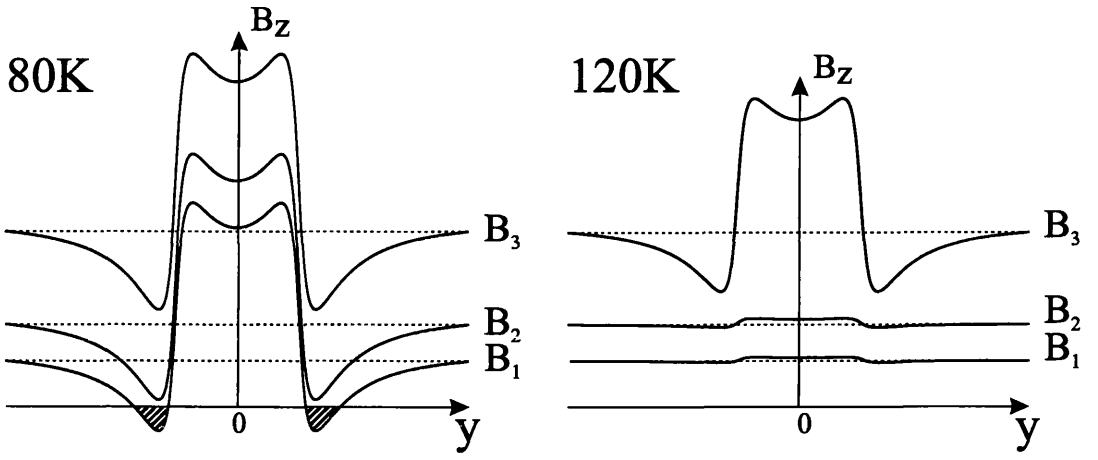

Figure 5.12: The magnetic field profile experienced by electrons in the 2DEG at different temperatures and different applied fields.

Figure 5.12 shows the resulting field profiles in the 2DEG at temperatures of 80 and 120K, for the three values of B_a indicated in figure 5.11. At 80K the dysprosium is ferromagnetic and B_1 lies in the region where the modulation is greater than the applied field. For this reason, the profile still has negative regions and so snake states can propagate. B_2 marks the end of snake states as all the negative regions have disappeared. At field B_3, cycloid states would be dominating if it weren't for their temperature dependence. As it is, the combination of temperature and lack of negative field regions remove the possibility of magnetic channelling. For the 120K traces, fields B_1 and B_2 are not sufficient to turn-on the magnetism and B_3 is larger than the size of the modulation, so even once the stripe has magnetised, there are still no negative regions. In fact, for temperatures of 100K and above, the turn-on field is always larger than the negative modulation from the magnetised stripe so channelling cannot occur.

Having ruled out channelling as the cause of the residual R_{xx} peak at 100K, another explanation is required. Figure 5.13 shows the field value at which the peaks form (■ with error bars showing the variation between the peaks at positive and negative magnetic fields) and the value of magnetic field required to restore the alignment in dysprosium (○). The similar trend and values of these curves leads to the conclusion that the residual peaks are caused by the dysprosium magnetising. Reijniers and Peeters explanation of peak formation due to magnetisation of the stripe was based on a quantum mechanical model which is inappropriate at 100K. Instead, a classical explanation is needed to explain the increased resistance. The most likely explanation is that the jump in mag-

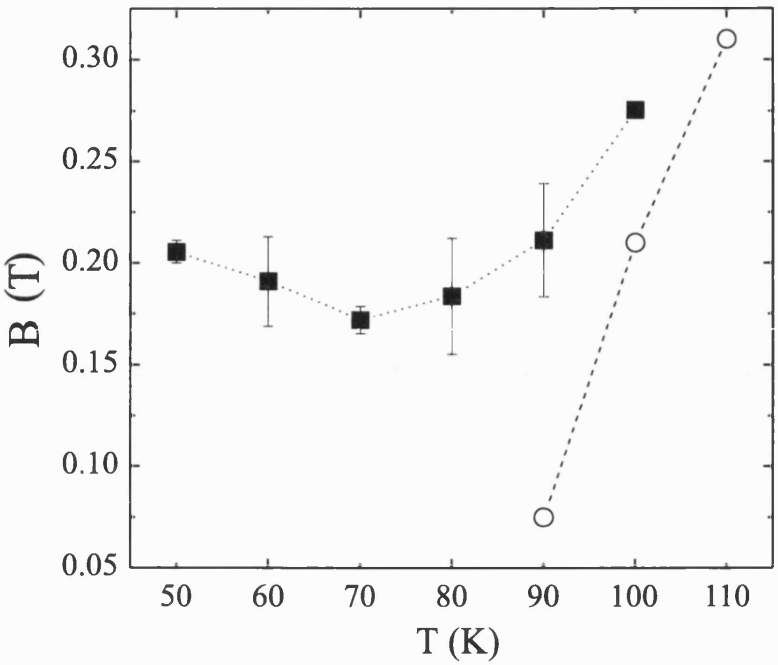

Figure 5.13: Comparison of experimentally measured peak positions (■) and the turn-on field (○) for dysprosium in its helical state.

netic field, as the stripe magnetises, increases the collision rate of electrons with the sample boundaries and with diffuse boundary scattering, this leads to an increased resistance (similar to the size effect explained in section 3.4.1). The exact cause of the peaks at 90K is unclear. In principle, the turn-on field of ~0.075T should enable the modulation to be bigger than the applied field and so snake states should be possible. However, ΔR_{xx} does decrease significantly between 70 and 80K so potentially the 90K result is showing a combination of snake state channelling and increased scattering.

It should be noted that the comparison between the stripe's modulation and the applied field in figure 5.11 is for the specific dysprosium sample studied. In principle, with a thicker dysprosium layer, the modulation would be larger and channelling could continue above the Curie temperature if scattering limitations were also overcome.

5.6 Conclusions

The robustness of snake orbits relative to cycloid orbits has been demonstrated experimentally and theoretically. Although the cycloid states and cyclotron orbits are rapidly quenched, snake states are less affected and persist to higher temperature. A simple theory can account for the similarities between the cycloid states and cyclotron orbits and a drift diffusion model shows features in agreement with the experimental behaviour. These findings have implications for relaxing the stringent requirements of device fabrication as snake states are capable of surviving considerable disorder.

The results initially appear to conflict with those obtained in chapter four when the gate voltage was varied. However, closer examination suggests that the increasing temperature presents a far more effective disruption to the transport as the Shubnikov de-Haas oscillations are quenched rapidly which was not observed for any value of the gate voltage.

The measurements at higher temperature have shown the device's sensitivity to changes in the magnetisation of the ferromagnetic stripe and the order of magnitude difference between effects of the magnetisation and effects of channelling.

Chapter 6

Ongoing Research and Future Work

6.1 Introduction

This chapter holds several pieces of research that have only been briefly investigated so far. Work is presented on rectification effects and quantisation due to the quantum mechanical confinement of snake states. This chapter also contains some plans for future experiments with new sample designs and experimental regimes to be investigated.

6.2 Electrical Rectification

Work by O. V. Kibis over the last four years has shown [64, 65] that in low dimensional systems with an asymmetric quantizing potential, the effects of interactions between electrons and quasi-particles of the system, like photons and phonons, also become asymmetric. In the presence of any isotropic perturbation, this imbalance in interactions leads to an electromotive force being established.

This can best be understood by considering figure 6.1. An electron with momentum, k_1, is shown interacting with phonons of momentum $\pm q$ in an asymmetric

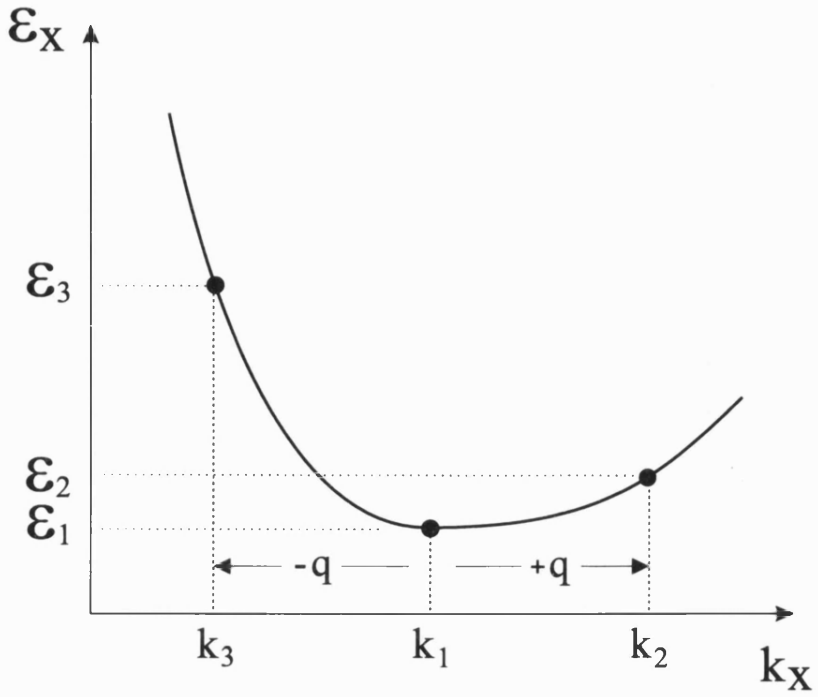

Figure 6.1: The effect of an asymmetric energy dispersion relationship in the presence of phonon interactions.

potential. The interaction with the phonon of momentum $-q$ leads to the electron being in a higher energy state with a higher velocity than the electron in state k_2. If a system with this energy asymmetry is perturbed in an isotropic manner so that equal numbers of $\pm q$ interactions occur, the difference in velocities will result in an electron drift leading to the establishment of an electromotive force. (See ref. [66] for more a more detailed explanation.)

Experimental evidence for this effect has been seen in thermopower experiments [67] where a heating current is applied between two opposite contacts of a Hall bar and the resistance is measured further down the Hall bar. In ref. [67], the asymmetry was provided by the nature of the 2DEG and an in-plane magnetic field. A common first approximation to the confinement created by a 2DEG is to use a triangular well potential. By applying a magnetic field in the y-direction (see figure 6.2), the effect is to move the maximum of the electron wavefunction in the potential of the 2DEG. Depending on the direction the electron is travelling, this will either increase or decrease the electron energy, hence the electron energy spectrum is made asymmetric by the asymmetry of the 2DEG potential and the applied field.

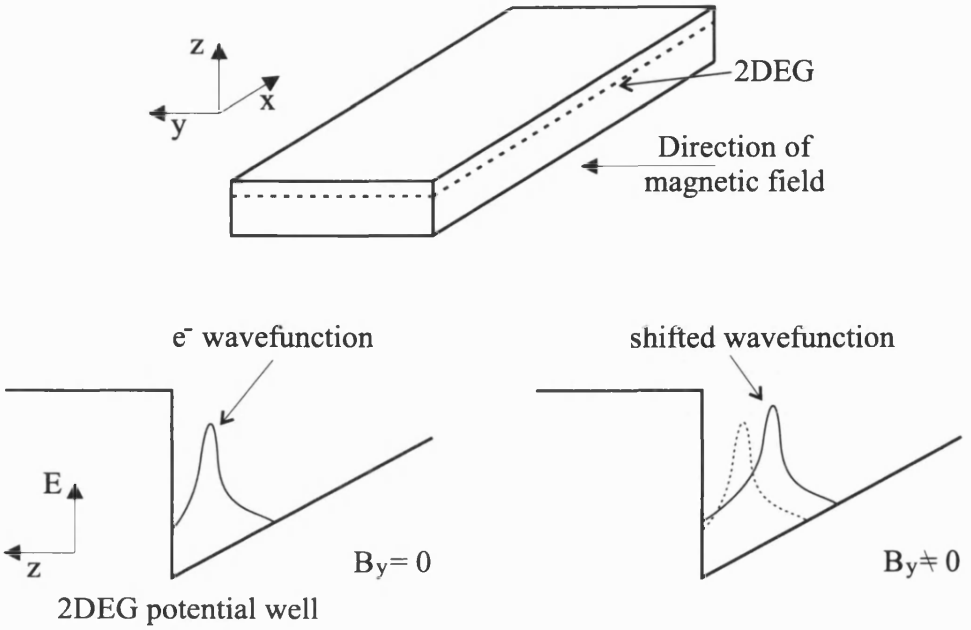

Figure 6.2: Using the 2DEG as an asymmetrical quantizing potential.

The samples used in this report are mainly δ-doped 2DEGs so the potential well is practically square. However, an asymmetric energy dispersion curve can be realised in the snake state devices by magnetising the stripe parallel to the 2DEG. This results in a magnetic profile which is asymmetric about y=0 (see figure 3.3 in section 3.2). This profile is approximated to a magnetic step to enable analysis and results in the energy levels shown in figure 6.3.

The rectification process can also be understood in terms of energy and momentum conservation. For an electron excited slightly above the Fermi energy, relaxing back to the Fermi energy can be achieved by emitting a phonon of momentum q. The probability of phonon emission is greater for small q, therefore emission will occur towards the $k_x > 0$ direction as there are no available states in the opposite direction. It would also be possible to relax into a lower subband but that would require a phonon with greater momentum and is less likely.

6.2.1 Experimental Results

Figure 6.4 shows the resistance of a dysprosium striped device magnetised parallel to the stripe. The traces show opposite current directions for two different values of the gate voltage at 1.35K. The measurements were made non-locally i.e. four

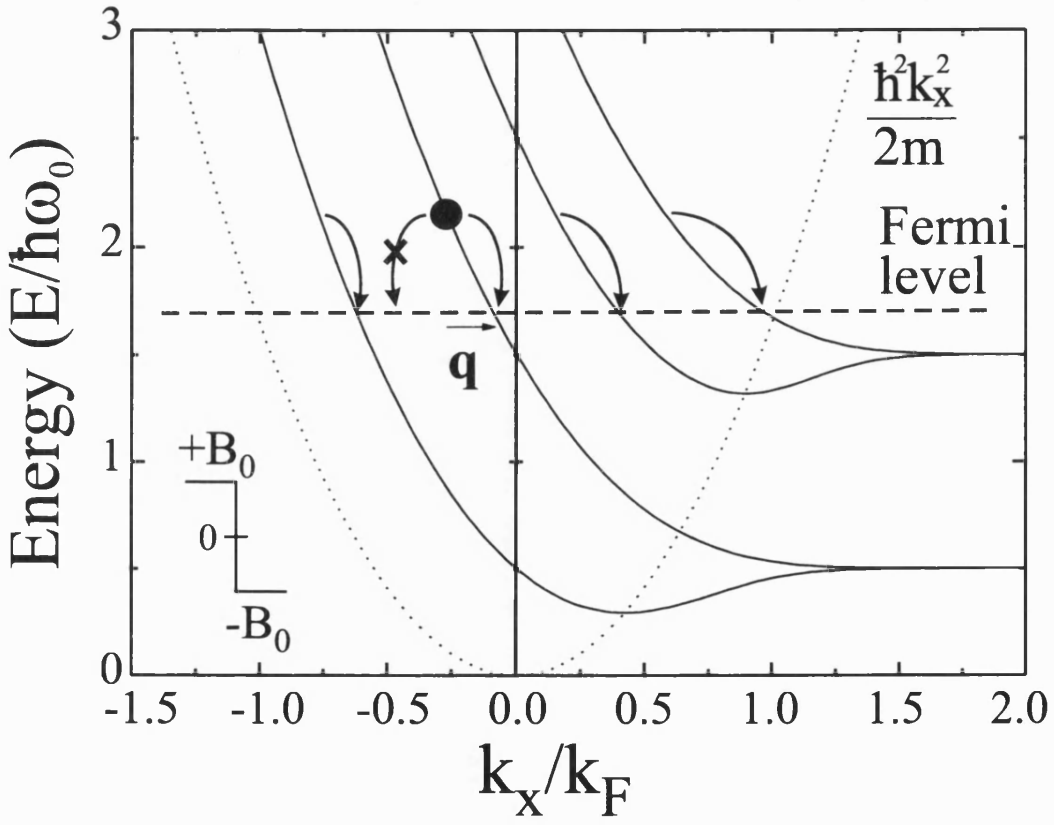

Figure 6.3: Calculated energy levels for snake state orbits in an step potential from $-B_0$ to $+B_0$.

consecutive contacts were used, the current passed between the first two and the resistance measured between the third and forth.

The upper curves are with no applied gate bias, the solid line shows the magnetic field being swept up and the dashed line shows the field being swept down. There is some hysteresis in these curves but they have similar trends. In the region from -1T to -3T the curves are fairly evenly separated with a splitting of around 10Ω. The lower set of curves show a larger splitting resulting from the negative gate bias; the reduction in carrier density leads to a larger effect as explained further in section 6.2.2. In both cases, the splitting decreases as the field approaches zero and the magnetisation of the stripe is diminished. From the splitting value of 10Ω the experimental e.m.f. per unit length is calculated as $|E_x/L_x| \sim 3 \times 10^{-2}$ V/cm.

6.2.2 Theory

This section contains an abbreviated version of the theory developed by O. V. Kibis [68] for the specific case of asymmetry introduced by a step-like magnetic potential.

The system is setup by considering a 2D electron system in {x, y, z} co-ordinates (same geometry as in figure 6.2) and approximating the effect of the magnetic stripe by introducing the non-uniform magnetic field, $B_z(y)$, shown in the inset to figure 6.3:

$$B_z(y) = \begin{cases} B_0 & \text{y} > 0, \\ -B_0 & \text{y} < 0. \end{cases} \tag{6.1}$$

where the z-axis is perpendicular to the plane of the device. The Hamiltonian for electrons in this magnetic field is $\hat{H} = \hat{H}^{(0)} + \hat{H}^{(1)}$ where:

$$\hat{H}^{(0)} = -\frac{\hbar^2}{2m}\frac{d^2}{dy^2} + \frac{\hbar^2 k_x^2}{2m} + \frac{\omega_0^2 m y^2}{2}, \tag{6.2}$$

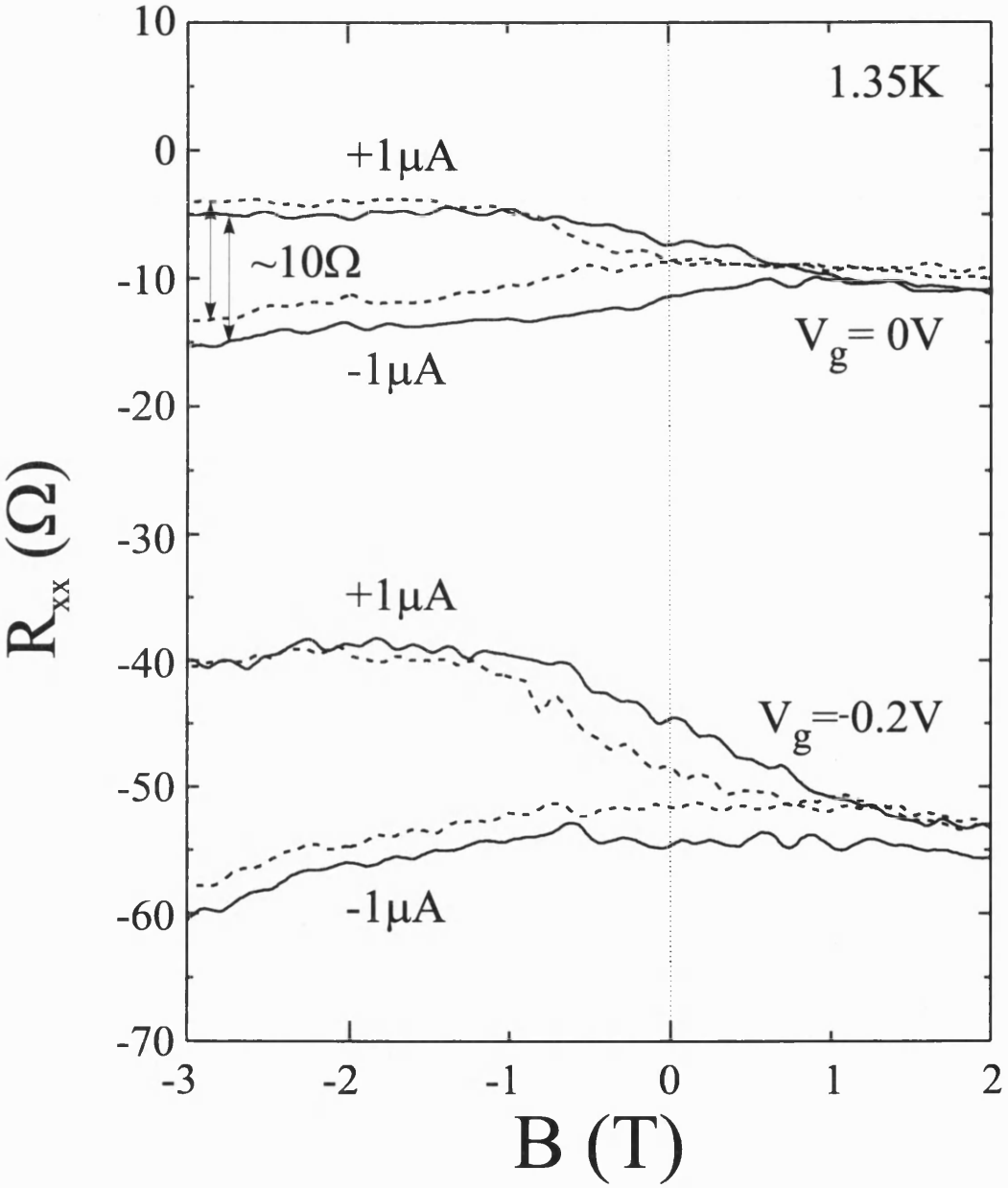

Figure 6.4: Non-local measurements of R_{xx} showing a splitting for different current directions.

$$\hat{H}^{(1)} = -\hbar\omega_0 k_x |y|, \tag{6.3}$$

and $\omega_0 = eB_0/m$ is the Larmor frequency. For small wave vectors, k_x, the Hamiltonian, $\hat{H}^{(1)}$, can be considered as a perturbation and to the first order of the time independent perturbation theory, the energy and wave function in the first magnetic subband are:

$$\varepsilon(k_x) = \frac{\hbar\omega_0}{2} + \frac{\hbar^2 k_x^2}{2m} - \frac{l_H k_x}{\sqrt{\pi}}\hbar\omega_0, \tag{6.4}$$

$$\phi(k_x, y) \approx \psi_0^{(0)}(y) + \frac{l_H k_x}{2\sqrt{2\pi}}\psi_2^{(0)}(y), \tag{6.5}$$

where $l_H = \sqrt{\hbar/eB_0}$ is the characteristic magnetic length and $\psi_n^{(0)}(y)$ are the standard harmonic oscillator wavefunctions.

As shown in figure 6.3, the electron energy spectrum is asymmetric, $\varepsilon(k_x) \neq \varepsilon(-k_x)$. It follows that the interaction between the electron system and phonons of wave vector q and -q is different. The wavefunctions in eq. 6.5 are used to calculate the phonon emission and absorption scattering rates. The imbalance in phonon emission and absorption results in the emergence of an e.m.f., E_x, of phonon drag of electrons along the x-axis. The effect is prominent here due to the large $\varepsilon(k_x)$ asymmetry arising from the magnetic potential. The application of the theory, in the quantum limit situation where B_0 is large and the temperature is low, yields the e.m.f. in a magnetic edge channel as:

$$E_x \sim \left(\frac{\Xi m}{\pi}\right)^2 \frac{L_x l_H^3}{\rho \nu_l^5 e\hbar^7}(2k_B\Delta T)^5, \tag{6.6}$$

where Ξ = the deformation potential constant, ρ = the crystal density, ν_l = the longitudinal speed of sound in the crystal, L_x = the length of magnetic edge channel, and $\Delta T = T_e - T_l$ (the difference in temperatures of the electrons and crystal lattice). It should be noted that this result assumes a non-degenerate electron gas and describes the fraction of the Fermi surface near $k_x = 0$.

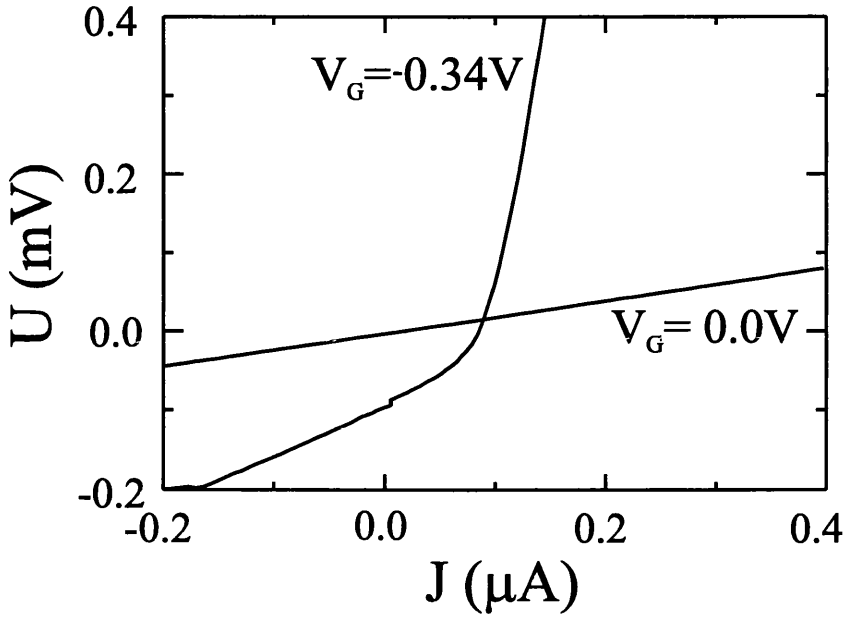

Figure 6.5: The rectified IV characteristic for different gate bias. B = -1T.

The temperature difference between the electrons and the lattice can be found from standard thermo-exchange theory [69, 67] using the expression, $\Delta T \sim P\tau/n_s k_B$ where $P = J^2R/S$, the power of the electrical current per unit area, R is the resistivity of channel, S is the area of the channel and τ is the relaxation time. Values for the experiment are $J \sim 10^{-6}$A, $R \sim 10\Omega$ and $n_s \sim 10^{11}\text{cm}^{-2}$. When the carrier density is reduced, ΔT increases leading to the larger effect seen with negative gate biases. The area of the channel is $S \sim l_H L_x$ being $\sim 10^{-8}\text{cm}^2$ for a value of B_0 of $\sim$1T and the acoustic phonon lifetime in GaAs is $\tau \sim 10^{-9}$s. These values give a temperature difference $\Delta T \sim 1$K.

Substituting the value for ΔT back into eq. 6.6 and using tabulated values for m, ρ, Ξ and ν in GaAs the electromotive force per unit length is calculated to be $|E_x/L_x| \sim 10^{-2}$ V/cm. This is in good agreement with the earlier calculated value of 3×10^{-2} V/cm for the e.m.f corresponding to the 10Ω split in figure 6.4

Additionally, figure 6.5 shows the IV characteristic for a sample with zero gate voltage and also when heavily depleted. In this experiment, Joule heating is independent of the direction of current flow and ΔT and the e.m.f. are even with respect to the electrical current, J. The I-V characteristic of the channel will then include both the even phonon drag and the odd ohmic contributions leading to the voltage drop, U, along the channel having current-reversal asymmetry, $U(J) \neq U(-J)$. These results were taken at 4.2K and with a field of -1T which

may explain why the rectification isn't obvious with no applied gate voltage even though it is clear in figure 6.4.

6.3 Electronic Structure of Snake States

Figure 6.3 shows the calculated energy levels for snake states in a step-function magnetic field. With the idea of discrete energy levels comes the possibility of observing the effect of individual subbands on the device conduction. A simple way to investigate this is to measure the resistance as the gate voltage is changed. An increasingly negative gate voltage will affect the Fermi energy, moving it down through the snake state energy levels. The reduction in number of subbands intersecting the Fermi energy will result in increases in resistance. Knowing the carrier density change with gate voltage allows the calculation of the 'leverage factor' between the gate voltage and Fermi energy by considering the following equations:

$$\begin{aligned} n_s &= f(V_g) \\ k_F &= \sqrt{2\pi n_s} \\ E_F = \frac{(\hbar k_F)^2}{2m} &= \frac{\hbar^2 \pi n_s}{m}. \end{aligned}$$

Hall measurements show the carrier density changing from 3.97 to 3.09×10^{11} cm^{-2} when the gate voltage is changed from 0.2 to -0.3V. This corresponds to the Fermi energy changing from 14.2 meV to 11.1 meV giving:

$$\Delta E_F \simeq \frac{1}{160}\Delta V_g. \tag{6.7}$$

The energy spacing of the snake states is of order $\hbar\omega_c$ and will be constant once the stripe is fully magnetised parallel to the stripe. The profile from the parallel magnetised stripe is hard to approximate as it contains sharp peaks of up to $\pm$1.8T but using the average value of B $\sim$0.3T gives energy level spacings of 0.52

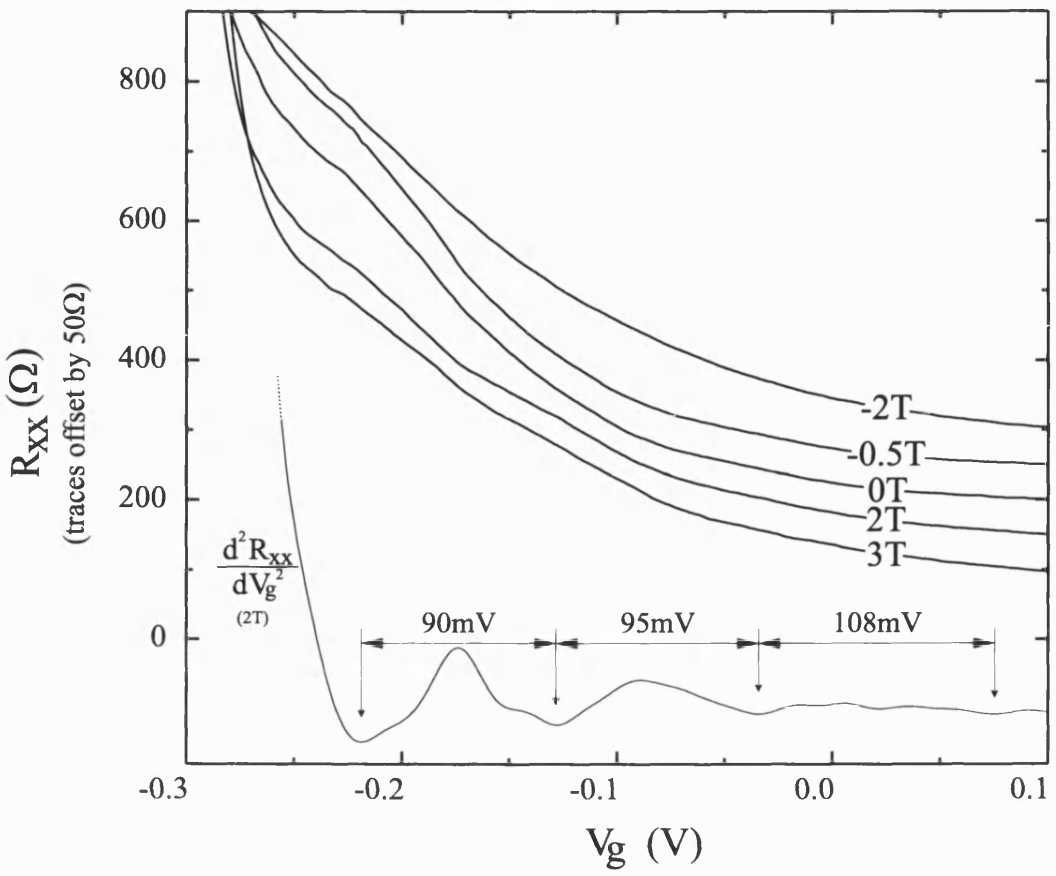

Figure 6.6: Gate voltage sweeps showing possible quantisation of snake state energy levels. The 2nd derivative of the 2T trace is also shown.

meV. Using this value in eq. 6.7 gives $\Delta V_g = 83$ mV.

Figure 6.6 shows several resistance traces (at different values of the external field) as the gate voltage is swept from 0.1 to -0.3V. Features are apparent in the traces which are clearer in the 2nd derivative (also shown). The spacing of the features is around 100 mV in all the traces in good agreement to the rough value of 83 mV obtained above.

All the curves from 3T to -0.5T show these features but they have practically disappeared in the -2T curve and do not reappear at higher negative fields. There is no immediately obvious reason why this should be the case.

6.4 Device Design

All the results in this thesis come from very similar devices incorporating a Hall bar with a ferromagnetic stripe and gate layer. The only differences are in the wafer properties and the composition of the stripe. The following sections look at two new designs to allow better comparison between samples with and without snake states and further probing of the quantum mechanical aspects of snake states.

6.4.1 Symmetrical Design

Comparing samples with different fabrication histories is not ideal as the sample properties change during fabrication. Minor damage to the surface can affect carrier density and mobility and building up composite layers can induce strain and piezoelectric effects. Add to this the slight variations in experimental conditions (exact placement in magnetic field, minor temperature variations etc.) and inevitable errors are introduced. In the case of devices exhibiting magnetic channelling, these issues are compounded by snake and cycloid effects on the Hall and longitudinal resistance. At least at low field, the Hall resistance is enhanced but does this signify a lower carrier density?

One solution for making accurate assessments of the effect of magnetic channelling would be to have a stripe which only covered certain portions of a device, leaving spare contacts in the uninfluenced region. Figure 6.7a shows a symmetrical contact arrangement connected to the active region shown (enlarged) in 6.7b. The Hall bar contact spacing is the same on the left and right areas of the design with the stripe over only the left hand contacts. The area with the stripe would experience some additional strain but this should be minimised by the gate layer.

Experiments performed on the stripe covered contacts could be repeated on the uncovered contacts with the results being directly comparable. The difference between the two results would show exactly what effect the snake and cycloid states were having.

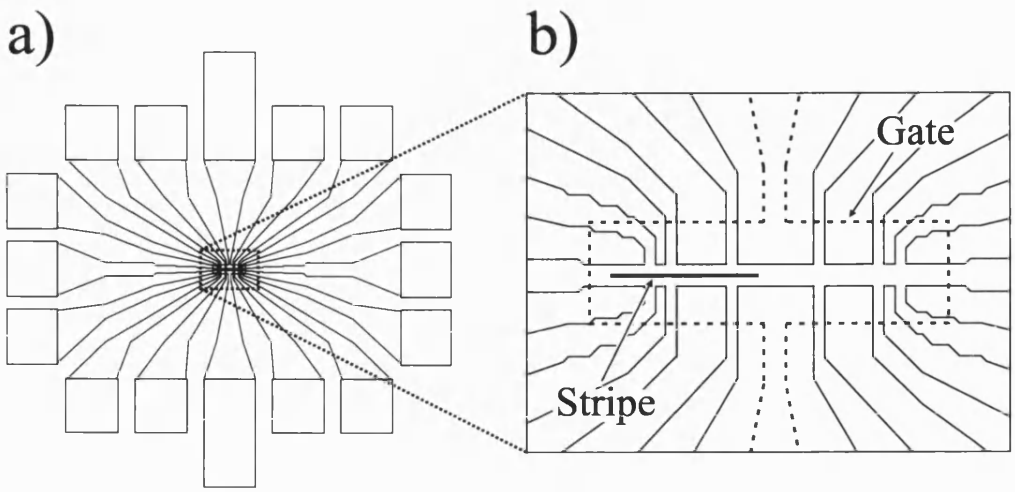

Figure 6.7: Design for a new symmetrical device. a) shows the contact layout, the dotted box is enlarged in b) showing the active area.

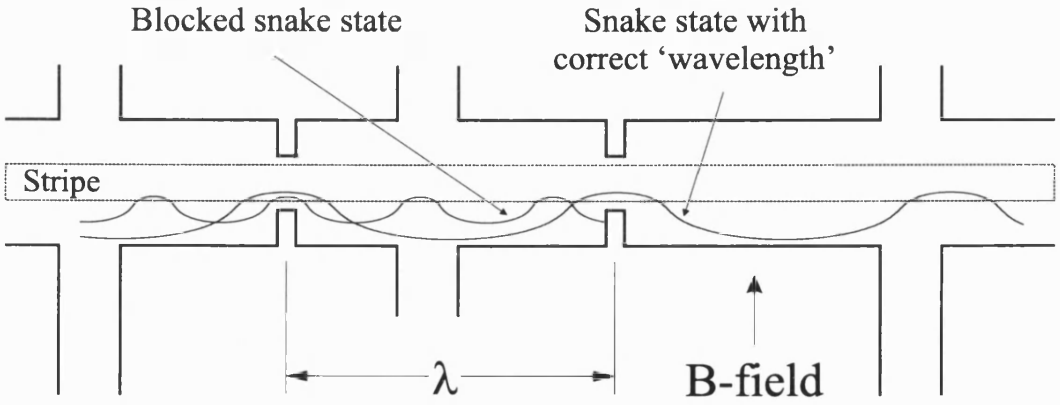

Figure 6.8: 'Spectrometer' sample designed to examine quantised snake states.

6.4.2 Spectrometer

Figure 6.8 shows the 'spectrometer' design for low temperature experiments where the snake states should form well defined quantised states.

Constricting the channel (by making additional etches across the channel), will isolate snake states of a certain 'wavelength'. The magnetic field is applied in the plane of the 2DEG so as the field is increased and the stripe magnetises, different states will be allowed to pass between the etches. This would allow further investigation of the energy levels of snake states.

6.5 Fractional Quantum Hall Experiments

It has always been an aim of this work to investigate the behaviour of composite fermions (CFs). The analogue between CFs in the ν=1/2 region and electrons at zero-field suggest that it should be possible to observe magnetic channelling of CFs but investigating this requires the high magnetic fields ($\gtrsim$20T) only available at Grenoble. This would be another situation where it would be useful to have the symmetrical design for comparing the shape of the magnetoresistance around ν=1/2 with and without the stripe's influence.

Two attempts were made at observing CF behaviour but unfortunately in both cases the sample mobility was too low. Higher mobility could be obtained by reverting to a conventional 2DEG structure which would bring the ν=1/2 regime to lower fields.

6.6 Conclusions

The presented experimental results concerning magnetically induced rectification effects show a change in resistance depending on whether the current flows along or against the direction of propagation of snake states. A theory is described based on the phonon drag of snake states which predicts the e.m.f to be of the same order as that calculated from the resistance splitting.

The experiments involving sweeping the gate voltage shows features with an energy spacing of around 100 mV. This spacing is in good agreement with the calculated spacings of snake state energy levels ($\sim$83 mV) in a magnetic field stepping from -0.3 to +0.3T.

Two possibilities for new sample designs have been outlined, a symmetrical design where the stripe affects only half the contacts and a 'spectrometer' design. The first would be useful for examining the actual magnitude of the effect of snake and cycloid states, the second presents an alternative method for examining discrete snake states.

The work presented in this chapter is still at an early stage but represents the next steps in investigating the effects and possibilities of magnetic channelling.

Chapter 7

Conclusions

The work contained in this thesis represents the continuation of initial research into snake and cycloid states. Three major areas have been investigated to look at specific issues.

The first area examined was whether snake and cycloid states were the best explanation for the peaks formed in the magnetoresistance. The most credible alternative explanation was concerned with the stripe magnetising rather than the profile from the stripe. However, the dependance of the peaks in R_{xx} and R_{xy} on the z-component of the applied field favoured the channelling interpretation. Approaches based on the size effect were countered by the absence of peaks in a sample without a stripe and later observations of the peak separation increasing as n_s decreased. An unlooked for result was the observation of features forming when the field was almost in the plane of the device. A theory based on the rotation of the magnetic moment overcoming the anisotropy in dysprosium produced a possible explanation. The precise details of the magnetisation of dysprosium are still unclear and moving to a system based on multi-layer magnetic films with well determined magnetic characteristics would be a useful step.

The second aspect of this work was the attempt to manipulate the peak formation by altering the contact spacing, stripe material and gate voltage. The results obtained by varying the contact separation showed there was no obvious length scale for the effect. Peaks were observed with contact spacing varying from 4 to 16μm with no change in the peak position. This supported the diffusion based

approach taken in attempts to model the devices.

Varying the material of the stripe confirmed the link between peak position and the profile. The best correspondence was to the early nickel and iron samples whose profiles bore closer resemblance to a square barrier. Comparing the peak position to the average negative magnetic field value was more accurate than simply comparing to the maximum negative value.

The effect of different carrier densities could also be seen. Varying the gate voltage produced a shift in peak position of over 350% with the peak structure also becoming more pronounced. Three factors contributing to the increasing peak separation were identified: greater scattering of cycloid orbits relative to snake orbits, the channel width dependence of the two types of orbit and the changing background. The peaks becoming more pronounced was understood through the lower carrier velocities leading to a higher proportion of the electrons performing snake and cycloid orbits.

Two models were developed to examine the situation; one from a semi-classical drift diffusion approach and the other from considering the velocity correlation. The former was useful for examining the peak position and the latter allowed more realistic conditions to be considered and was closer to matching the size of the effects.

The third major area for investigation was the temperature dependence of snake and cycloid states. Experimentally, the effects of snake states were observed up to the Curie temperature of the dysprosium striped sample but the cycloid states were quenched around a temperature of 30K. Examining the periods of the two types of state showed the robustness of snake states was explainable by their, potentially, very short period whereas the cycloid state's periods were similar to cyclotron orbits (also quenched by 30K). This idea was successfully incorporated into the drift diffusion model.

In addition, the measurements at higher temperature showed some small structure even above dysprosium's Curie temperature. This was attributable to dysprosium entering a helical magnetisation phase, the features forming as the magnetisation was switched on.

One of the most interesting results has been the verification of R_{xy} depending on R_{xx}. A non-linear Hall effect has been observed when the angle, carrier density and temperature have all been varied. Removing the linear background left a peak structure with the same shape as R_{xx} even when that shape was being dramatically changed by the effects of temperature.

In the final chapter, some current research based on a quantum mechanical picture of snake state subbands was outlined and several effects observed. Firstly, non-local measurements of resistance showed a splitting in the resistance for different current directions; current voltage characteristics were also seen to become non linear as the 2DEG was depleted. An explanation was presented based on the emergence of an e.m.f. due to the asymmetry of the snake state energy dispersion.

Secondly, features with a periodicity of around 100 mV were observed in the longitudinal resistance as the gate voltage was swept. This spacing corresponded well to calculated spacings of snake state subbands ($\sim$83mV in a field of 0.3T). The good agreement suggested that these features were the effect of snake state subbands becoming depopulated.

Two new device designs were suggested for examining the actual magnitude of the effect of snake and cycloid states and further probing the discrete energy spectrum of snake states. The rectification and gate effects that have been observed require further study to confirm their true origins. It would also be interesting to measure the temperature dependence in a iron sample between cryogenic and room temperatures.

The above observations lead to three conclusions about magnetic channelling:

- Hall effect measurements are sensitive to magnetic channelling and hence caution should be exercised when using Hall magnetometers in close proximity to magnetic elements.
- Magnetic channelling via snake states is robust in the face of disorder making it a viable means of controlling electron motion in less pure semiconductors.
- Magnetic channelling can be a valuable tool for studying the magnetic properties of the stripe material.

References

[1] H. C. Casey Jr., A. Y. Cho, and P. A. Barnes, IEEE J. Quantum Elect. **11** (1975), 467.

[2] L .L. Chang, L. Esaki, and R. Tsu, Appl. Phys. Lett. **24** (1974), 593.

[3] F. Capasso, K. Mohammed, A. Y. Cho, R. Hull, and A. L. Hutchinson, Phys. Rev. Lett. **55** (1985), 1152.

[4] S. M. Sze. *Physics of Semiconductor Devices.* John Wiley & Sons Ltd., New York, 2nd edition, 1981.

[5] C. Weisbuch and B. Vinter. *Quantum Semiconductor Structures - Fundamentals and Applications.* Academic Press Inc., San Diego, 1991.

[6] M. J. Kelly. *Low-Dimensional Semiconductors - Materials, Physics, Technology, Devices.* Clarendon Press, Oxford, 1995.

[7] C. W. J. Beenakker and H. Van Houten. *Quantum Transport in Semiconductor Nanostructures*, volume 44 of *Solid State Physics - Advances in Research and Applications.* Academic Press, Inc., San Diego, US, 1991.

[8] K. Von Klitzing, G. Dorda, and M. Pepper, Phys. Rev. Lett. **45** (1980), 494.

[9] D. C. Tsui, H. L. Stormer, and A. C. Gossard, Phys. Rev. Lett. **48** (1982), 1559.

[10] J. K. Jain, Phys. Rev. Lett. **63** (1989), 199.

[11] B. I. Halperin, P. A. Lee, and N. Read, Phys. Rev. B **47** (1993), 7312.

[12] W. Kang, H. L. Stormer, L. N. Pfeiffer, K. W. Baldwin, and K. W. West, Phys. Rev. Lett. **71** (1993), 3850.

[13] J. H. Smet, D. Weiss, K. Von Klitzing, P. T. Coleridge, Z. W. Wasilewski, R. Befgmann, H. Schweizer, and A. Scherer, Phys. Rev. B **56** (1997), 3598.

[14] G. M. Gusev, D. K. Maude, X. Kleber, et al., Solid State Comms. **97** (1996), 83.

[15] D. G. Polyakov, F. Evers, A. D. Mirlin, and P. Wölfle, Physica B **256-258** (1998), 441.

[16] D. Weiss, K. Von Klitzing, K. Ploog, and G. Weimann, Europhys. Lett. **8** (1989), 179.

[17] R. R. Gerhardts, D. Weiss, and K. Von Klitzing, Phys. Rev. Lett. **62** (1989), 1173.

[18] R. W. Winkler, J. P. Kotthaus, and K. Ploog, Phys. Rev. Lett. **62** (1989), 1177.

[19] C. W. J. Beenakker, Phys. Rev. Lett. **62** (1989), 2020.

[20] P. Vasilopoulos and F. M. Peeters, Superlatt. Microstruct. **7** (1990), 393.

[21] H. A. Carmona, A. K. Geim, A. Nogaret, P. C. Main, T. J. Foster, and M. Henini, Phys. Rev. Lett. **74** (1995), 3009.

[22] P. D. Ye, D. Weiss, R. R. Gerhards, M. Seeger, K. von Klitzing, K. Eberl, and H. Nickel, Phys. Rev. Lett. **74** (1995), 3013.

[23] M. L. Leadbeater, C. L. Foden, J. H. Burroughes, M. Pepper, T. M. Burke, L. L. Wang, M. P. Grimshaw, and D. A. Ritchie, Phys. Rev. B **52** (1995), R8629.

[24] F. M. Peeters, J. Reijniers, S. M. Badalian, and P. Vasilopoulos, Microelectron. Eng. **47** (1999), 405.

[25] J. Reijniers and F. M. Peeters, J Phys.: Condens. Matter **12** (2000), 9771.

[26] A. K. Geim, S. V. Dubonos, J . G. S. Lok, I. V. Grigorieva, J. C. Maan, L. Theil Hansen, and P. E. Lindelof, Appl. Phys. Lett. **71** (1997).

[27] V. Kubrak, F. Rahman, B. L. Gallagher, et al., Appl. Phys. Lett. **74** (1999), 2507.

[28] M. Johnson, B. R. Bennet, M. J. Yang, M. M. Miller, and B. V. Shanabrook, Appl. Phys. Lett. **71** (1997), 974.

[29] F. G. Monzon, M. Johnson, and M. L. Roukes, Appl. Phys. Lett. **71** (1997), 3087.

[30] J. Reijniers and F. M. Peeters, Appl. Phys. Lett. **73** (1998), 357.

[31] J. Reijniers and F. M. Peeters, J. App. Phys. **87** (2000), no. 11, 8088.

[32] A. Nogaret, S. J. Bending, and M. Henini, Phys. Rev. Lett. **84** (2000), 2231.

[33] Department of Physics and Astronomy, University of Nottingham, Nottingham, NG7 2RD.

[34] H. Van Houten, B. J. Van Wees, M. G. G. Heijman, and J. P. André, Appl. Phys. Lett. **49** (1986).

[35] Ralph E. Williams. *Galluim Arsenide Processing Techniques.* Artech House, Dedham, USA, 1984.

[36] Intel Corporation, http://www.intel.com/pressroom/archive/releases/20020813tech.htm (20/8/02).

[37] A. C. Rose-Innes. *Low Temperature Laboratory Techniques.* Elliott Bros. & Yeoman Ltd., Liverpool, 2nd edition, 1973.

[38] J. E. Müller, Phys. Rev. Lett. **68** (1992).

[39] A. Nogaret, S. Carlton, B. L. Gallagher, et al., Phys. Rev. B **55** (1997), R16037.

[40] D. J. Craik. *Magnetism : Principles and Applications.* John Wiley & Sons Ltd., New York, 1995.

[41] C. Kittel. *Introduction to Solid State Physics.* John Wiley & Sons Ltd., New York, 5th edition, 1976. Note, quoted values for M_s are a factor $4\pi/10$ too small.

[42] P. D. Ye, D. Weiss, K. von Klitzing, K. Eberl, and H. Nickel, Appl. Phys. Lett. **67** (1995), 1441.

[43] S. Legvold. *Ferromagnetic Materials*, volume 1. North Holland, Amsterdam, 1980.

[44] A. W. Rushforth, B. L. Gallagher, P. C .Main, A. C. Neumann, C.H. Marrows, I. Zoller, M. A. Howson, B. J. Hickey, and M. Henini, Physica E **6** (2000), 751.

[45] M. L. Roukes, A. Scherer, S. J. Allen Jr., H. G. Craighead, R. M. Ruthen, E. D. Beebe, and J. P. Harbison, Phys. Rev. Lett. **59** (1987), 3011.

[46] T. J. Thornton, M. L. Roukes, A. Scherer, and B. P. Van de Gaag, Phys. Rev. Lett. **63** (1989), 2128.

[47] J. Reijniers and F. M. Peeters, Phys. Rev. B **63** (2001), 165317.

[48] Q. Ye, B. I. Shklovskii, A Zrenner, F. Koch, and K. Ploog, Phys. Rev. B **41** (1990), 8477.

[49] D. N. Lawton, A. Nogaret, S. J. Bending, et al., Phys. Rev. B **64** (2001), 033312.

[50] P. Rhodes and G. Rowlands, Proc. Leeds. Phil. Soc. **6** (1954), 191.

[51] E. C. Stoner and E. P. Wohlfarth, Philos. Trans. Roy. Soc. A **240** (1948), 599.

[52] R. R. Gerhardts, Phys. Rev. B **53** (1996), 11064.

[53] MathSoft Inc. *Mathcad 8 Professional.* U.S.

[54] W. H. Press, S. A. Teukolsky, W. T. Vetterling, and B. P. Flannery. *Numerical Recipes in C - The Art of Scientific Computing.* Cambridge University Press, Cambridge, U.K., 2nd edition, 1992.

[55] D. C. Look. *Electrical Characterization of GaAs Materials and Devices.* John Wiley & Sons Ltd., New York, 1989.

[56] J. Singh. *Physics of Semiconductors and their Heterostructures.* McGraw Hill, New York, 1993.

[57] E. E. Mendez, P. J. Price, and M. Heiblum, Appl. Phys. Lett. **45** (1984), 294.

[58] B. J. F. Lin, D. C. Tsui, M. A. Paalanen, and A. C. Gossard, Appl. Phys. Lett. **45** (1984), 695.

[59] B. J. F. Lin and D. C. Tsui, Surf. Sci. **174** (1986), 397.

[60] J. H. Davies. *The Physics of Low Dimensional Semiconductors.* Cambridge University Press, Cambridge, UK, 1st edition, 1998.

[61] D. E. Lacklison, J. J. Harris, C. T. Foxton, J. Hewett, D. Hilton, and C. Roberts, Semicond. Sci. Technol. **3** (1988), 633.

[62] M. K. Wilkinson, W. C. Koehler, E. O. Wollan, and J. W. Cable, J. Appl. Phys. **32** (1961), 48S.

[63] Soshin Chikazumi. *Physics of Magnetism.* John Wiley & Sons Ltd., New York, 2nd edition, 1966.

[64] O. V. Kibis, Phys. Lett. A **237** (1998), 292.

[65] O. V. Kibis, Physica B **256-258** (1998), 449.

[66] O. V. Kibis, J. Exp. Theor. Phys. **88** (1999), 527.

[67] A. G. Pogosov, M. V. Budantsev, O. V. Kibis, A. Pouydebasque, D. K. Maude, and J. C. Portal, Phys. Rev. B **61** (2000), 15603.

[68] O. V. Kibis, Private Communications (2001).

[69] K. Hess and C. T. Sah, Phys. Rev. B **10** (1974), 3375.